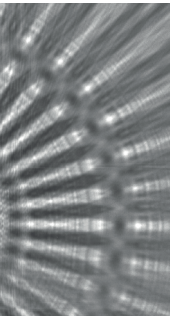


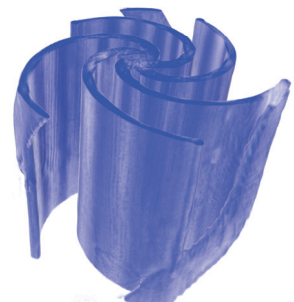
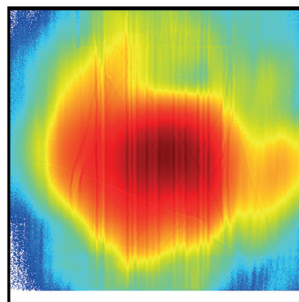
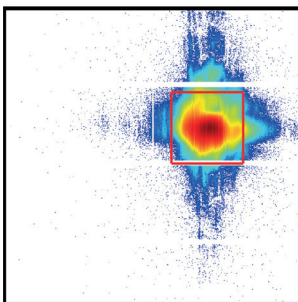
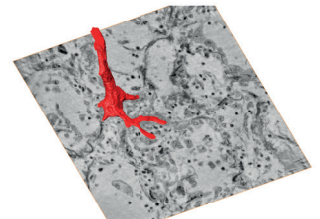
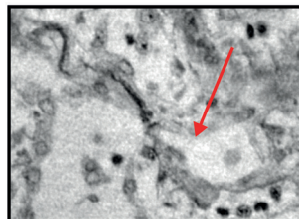
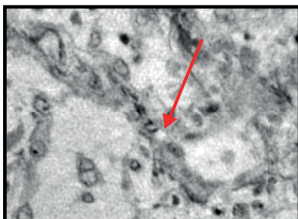
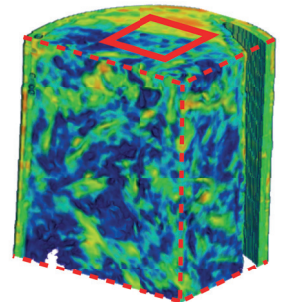
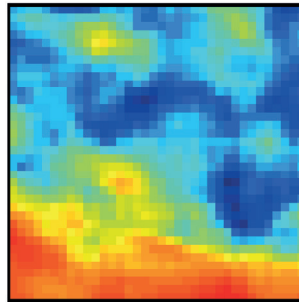
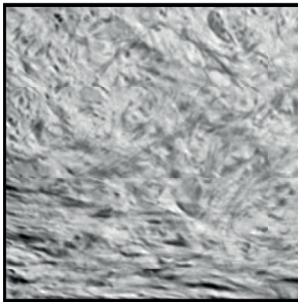


Göttingen Series in  
X-ray Physics



Jasper Frohn

## Multi-scale 3D virtual histology via phase-contrast X-ray tomography with synchrotron radiation





Jasper Frohn  
Multi-scale 3D virtual histology via phase-contrast X-ray tomography  
with synchrotron radiation

This work is licensed under a [Creative Commons Attribution-ShareAlike 4.0 International License](https://creativecommons.org/licenses/by-sa/4.0/).



Published in 2023 by Universitätsverlag Göttingen  
as volume 30 in the series “Göttingen series in X-ray physics”

---

Jasper Frohn

Multi-scale 3D virtual  
histology via phase-contrast  
X-ray tomography with  
synchrotron radiation

Göttingen series in X-ray physics  
Volume 30

Universitätsverlag Göttingen  
2023

## Bibliographic information published by the Deutsche Nationalbibliothek

The Deutsche Nationalbibliothek lists this publication in the Deutsche Nationalbibliografie; detailed bibliographic data are available in the Internet at <https://dnb.dnb.de>.

Funded by the Deutsche Forschungsgemeinschaft (DFG) Grant No. SFB 755 “Nanoscale Photonic Imaging”, the German Federal Ministry of Education and Research (BMBF) through Grant No. 05K19MG2 and Deutsche Forschungsgemeinschaft (DFG) DAPHNE4NFDI “DATA from PHoton and Neutron Experiments (DAPHNE) for a National Research Data Infrastructure (NFDI)”.

### *Contact*

Jasper Frohn

E-Mail: [jasper.frohn@phys.uni-goettingen.de](mailto:jasper.frohn@phys.uni-goettingen.de)

### Dissertation

for the award of the degree “Doctor rerum naturalium”  
of Georg-August-Universität Göttingen  
within the doctoral program in Physics  
of the Georg-August University School of Science (GAUSS)

### Thesis Advisory Committee

Prof. Dr. Tim Salditt, Institute for X-Ray Physics, Georg-August University, Göttingen

Prof. Dr. Alexander Egner, Institut für Nanophotonik, Göttingen

Prof. Dr. Frauke Alves, Institute of Diagnostic and Interventional Radiology and Clinic  
of Hematology and Medical Oncology, University Medical  
Center, Göttingen, and Translational Molecular Imaging, Max-  
Planck-Institute for Multidisciplinary Sciences, Göttingen

Date of the oral examination: 06.12.2022

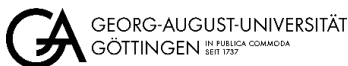
This work is protected by German Intellectual Property Right Law.

It is also available as an Open Access version through the publisher’s website and the Göttingen University Catalogue (GUK) at the Göttingen State and University Library (<https://www.sub.uni-goettingen.de>).

The license terms of the online version apply.

Typesetting and layout: Jasper Frohn

Cover picture: Jasper Frohn



© 2023 Universitätsverlag Göttingen, Göttingen

<https://univerlag.uni-goettingen.de>

ISBN: 978-3-86395-601-1

DOI: <https://doi.org/10.17875/10.17875/gup2023-2409>

ISSN: 2191-9860

eISSN: 2512-6326

## **Preface of the series editors**

The Göttingen series in x-ray physics is intended as a collection of research monographs in x-ray science, carried out at the Institute for X-ray Physics at the Georg-August-Universität in Göttingen, and in the framework of its related research networks and collaborations.

It covers topics ranging from x-ray microscopy, nano-focusing, wave propagation, image reconstruction, tomography, short x-ray pulses to applications of nanoscale x-ray imaging and biomolecular structure analysis.

In most but not all cases, the contributions are based on Ph.D. dissertations. The individual monographs should be enhanced by putting them in the context of related work, often based on a common long term research strategy, and funded by the same research networks. We hope that the series will also help to enhance the visibility of the research carried out here and help others in the field to advance similar projects.

Prof. Dr. Tim Salditt  
Prof. Dr. Sarah Köster  
Editors  
Göttingen June 2014

## **Preface to the present volume**

In biological tissues, structure matters – from organelle to organ. An intricate hierarchical cyto-architecture underlies and enables a diverse set of physiological functions. Contrarily, diseases are associated with pathological alterations of the tissue structure. Imaging and reconstructing physiological and pathological states are a matter of sample preservation, dimensionality, contrast, resolution, and field of view. Zooming in and out, trading resolution and field of view, extending the window of length scales, and creating contrast even for soft tissue components with weak contrast, is a formidable optical challenge.

In this work, three-dimensional phase-contrast X-ray imaging is augmented to a multi-scale approach by combining tomography with parallel and cone beam illumination, and a new form of super-resolution in-line holography, where the resolution is no longer limited by the demagnified pixel size. For the first time, this is shown to work also in full three dimensions. Working at the resolution frontier of holography, a new phase retrieval algorithm is proposed to extend holography to the highest level of resolution and beyond the ubiquitous assumption of a homogeneous object. Quite a tall order, and quite an evolution for a project which started primarily with synchrotron instrumentation and X-ray optics. And all this to the benefit of challenging applications, from pancreatic tumors to the histopathology of Covid-19.

Prof. Dr. Tim Salditt  
Göttingen, August 2023





# Contents

---

<b>1</b>	<b>Introduction</b>	<b>1</b>
<b>2</b>	<b>From basic X-ray interaction to 3D virtual histology</b>	<b>5</b>
2.1	X-ray interaction with matter . . . . .	5
2.2	In-line holography . . . . .	8
2.2.1	Free space propagation . . . . .	9
2.2.2	Intensity measurement and approximations . . . . .	11
2.2.3	Phase retrieval . . . . .	13
2.2.4	In-line holography resolution . . . . .	15
2.3	Basics of tomography . . . . .	15
2.4	3D virtual histology . . . . .	19
<b>3</b>	<b>Multi-scale approach (Scale I): Fast parallel beam tomography</b>	<b>21</b>
3.1	Motivation . . . . .	21
3.2	Experimental realization . . . . .	23
3.2.1	Propagation distance . . . . .	28
3.2.2	Spatial coherence . . . . .	33
3.2.3	Continuous tomography . . . . .	33
3.3	Human pancreatic tissue . . . . .	36
3.4	Lung tissue from Covid-19 patients . . . . .	42
3.4.1	Direct comparison of <i>H&amp;E</i> stained microscope and unstained X-ray phase-contrast images . . . . .	46
3.5	ID19 - Ischemic stroke in mouse brain tissue . . . . .	50
3.5.1	Sample preparation . . . . .	50
3.5.2	Parallel beam multi-scale tomography at ID19 . . . . .	51
3.5.3	Comparison of the ID19 detail setup and the GINIX parallel beam setup . . . . .	54
3.6	Discussion . . . . .	58
<b>4</b>	<b>Multi-scale approach (Scale II): Waveguide-based holotomography</b>	<b>61</b>
4.1	Motivation . . . . .	61

4.2	Holotomography setup at the GINIX . . . . .	62
4.3	Recent developments of X-ray waveguides . . . . .	64
4.3.1	Germanium waveguides . . . . .	65
4.3.2	Improved silicon waveguides . . . . .	68
4.4	Zyla X-ray detector . . . . .	69
4.4.1	Scintillators & Assembly . . . . .	71
4.4.2	Detector pixel response map . . . . .	74
4.5	3D virtual pathohistology of Covid-19 lung tissue . . . . .	79
4.6	Discussion . . . . .	84
<b>5</b>	<b>Multi-scale approach (Scale III): Super-resolution in-line holography</b>	<b>87</b>
5.1	Motivation . . . . .	87
5.2	Experimental realization . . . . .	88
5.3	Reconstruction scheme . . . . .	90
5.4	Results . . . . .	96
5.5	Discussion and Outlook . . . . .	107
<b>6</b>	<b>Conclusion and Outlook</b>	<b>109</b>
<b>A</b>	<b>Appendix</b>	<b>113</b>
A.1	Zyla scintillator exchange . . . . .	113
A.2	Derivation of the modified ePIE . . . . .	114
A.3	Silicon waveguide . . . . .	116
	<b>Bibliography</b>	<b>116</b>
	<b>List of publications</b>	<b>133</b>
	<b>Acknowledgements</b>	<b>135</b>
	<b>Curriculum Vitae</b>	<b>137</b>

# Introduction

---

# 1

The desire to cure diseases is probably as old as mankind itself. To fulfill this desire scientists attempt to understand the mechanisms of the phenomena in question. The corresponding scientific field, the study of diseases, is called **pathology**. It is an important field in medical research and medical diagnosis that addresses the cause of disease, its development, the structural changes and the corresponding manifestations. An important branch within pathology is **histology**, the study of biological tissue by the use of a light microscope, or in this context **histopathology** [Cul13]. Due to absorption, optical transmission microscopes require a sectioning of tissue, which is initially obtained by surgeries, biopsies, or autopsies into thin slices. In addition, the tissue must be stained to obtain sufficient contrast in the microscopic image. Hematoxylin and eosin staining (*H&E*) is the most widely used histological stain [BG08]. However, there are many different staining protocols, e.g. Masson-Goldner [Gol38] or immunostains, which use antibodies labeled with fluorescent dyes to visualize antigen-antibody interactions [CCJ41]. To this day, histopathological examination of biopsies is often the gold standard method for diagnosing tumor diseases. In addition to medical diagnosis, histopathology plays an important role in medical research due to its high-contrast and high-resolution two dimensional (2D) images. Despite the enormous success and importance of histology today, it has the limitation of providing only 2D images. In principle, 3D reconstructions are possible by acquiring multiple adjacent slices followed by subsequent alignment. However, the mechanical slicing leads to the occurrence of artifacts [Ger+08; Alb+21] and is very labor intensive. Furthermore, the 3D resolution is anisotropic due to the limited minimal slice thickness [Amu+13]. To this end, pathological conclusions and decisions are often based on single 2D slices. The aim of **3D virtual histology** is to overcome these limitations. **3D** sample volumes can be acquired by different imaging techniques e.g. by computed tomography (CT). One advantage of this approach is that no mechanical slicing is required, hence avoiding the invasive destruction of the sample. In addition, the reconstructed 3D volume can be **virtually** sliced in arbitrary directions. The application of computed tomography to the sample sizes used in **histology** therefore results in **3D virtual his-**

**tology.** The challenge is to achieve similar resolution and contrast as in conventional histology. However, if achieved, the accessibility to the 3D information can provide new insights to support conventional histology. For example, simply sliding through several hundred slices in different directions instead of a few in a fixed orientation can help evaluate structural changes of the sample under study. **3D virtual histology** is realised by different underlying contrast mechanisms and resolutions, e.g. by magnetic resonance imaging (MRI) with a resolution of  $52\ \mu\text{m}$  ex vivo as in [Cle+11], by photoacoustic tomography (PAT) with resolutions of  $\sim 100\ \mu\text{m}$  as in vivo [ZYW16; San+22], by light sheet fluorescence microscopy (LSFM) at sub-micrometer resolution ex vivo as in [Häg+17; HM22] or by **X-ray** tomography at sub-micrometer resolution ex vivo, which will be discussed in detail in the course of this work.

Furthermore, light microscopes offer the possibility of examining samples at different fields of view or length scales with the corresponding resolutions by changing the microscope objective used. This **multi-scale** capability is very powerful, since the tissue pieces can be investigated in their entirety, with the ability to zoom into specific areas of interest and observe them at a sub-cellular resolution. Since the scales complement each other, the access to multiple scales is important for a more complete assessment of the tissue. To this end, the realisation of such a multi-scale approach for 3D virtual histology is of great interest and subject of this work.

Due to the weak interaction with matter and the resulting high penetration depth, X-rays are predestined for tomographic acquisitions. The contrast mechanism of common X-ray tomography applications, e.g. in daily clinical routine, is based on absorption. Apart from absorption, the object-wave interaction also shifts the phases of the penetrating X-rays. This can be exploited for weakly absorbing objects, such as biological soft tissue. Both interactions are described by the complex index of refraction  $n = 1 - \delta + i\beta$  of the object, where the *decrement*  $\delta$  describes the phase shift and the *extinction coefficient*  $\beta$  the attenuation. For example, at an X-ray energy of 13.8 keV the decrement is  $\delta = 1.2 \times 10^{-6}$  and  $\beta = 1.4 \times 10^{-9}$  for soft tissue (*Tissue, Soft (ICRP)*) [Sch+11]. Thus, their ratio is  $\frac{\delta}{\beta} \approx 860$  and the phase-contrast is higher compared to the absorption-contrast. Since phases are not directly measurable, also known as the **phase problem**, different phase-sensitive imaging methods have been developed. Examples for phase-sensitive near-field imaging techniques are **grating-based (GBI)** [Dav+02; Mom+03; Pfe+06; Wei+05], **speckle-based (SBI)** [BWS12; MPS12; Zan+14; Zdo+17] and **propagation-based phase-contrast imaging (PBI)** [Sni+95; Clo+96; Pag+02; Clo+99], while ptychography [Die+10; Wil+12; Hol+14] and coherent diffractive imaging (CDI) [Mia+99; Brä+19] are imaging methods in the

---

far-field regime. Due to the high resolution of sub-50 nm in ptychography [Hol+19] and CDI [Brä+19], the resulting small field of views are unsuitable for 3D virtual histology. The achievable resolution of a few micrometer and the corresponding field of view of a few millimeter in GBI, SBI and PBI are more suitable for 3D virtual histology. The application to 3D virtual histology has been demonstrated in [Kim+20] for GBI, in [Zdo+20] for SBI and in [Fro+20a; Eck+20] for PBI. Of these three approaches PBI provides the highest spatial resolution [Zdo+20] and is therefore the subject of this work. The phase information is encoded in the measured intensity pattern, which is the square of the absolute value of the wavefield  $I = |\psi|^2$ , obtained by constructive and destructive interference of the scattered wavefield and the primary wavefield. The recovery of the introduced phase shifts is an ill-posed inverse problem, which requires elaborate reconstruction schemes. Examples for such **phase retrieval** algorithms are: the popular *Paganin* single step approach based on the transport-of-intensity equation (TIE) [Pag+02] for the edge-enhancement regime, the single step approach based on Contrast-Transfer-Function (CTF) for the holographic regime [Clo+99; Loh+20a] or iterative reconstruction schemes such as the Gerchberg-Saxton (GS), the Error-reduction (ER), the Hybrid-Input-Output (HIO) algorithm [Fie82], the relaxed averaged alternating reflections (RAAR) algorithm [Luk04] or a Tikhonov regularization-based approach [Huh+22].

The formation of an interference pattern by free space propagation is only possible with partially coherent X-rays. The partial spatial coherence of microfocus X-ray source is sufficient to enter the edge-enhancement regime (single fringe at the edges) in laboratories [Wil+96; TOH07; Bar+13]. Additional temporal coherence is required to obtain phase-contrast in the holographic regime (multiple interfering fringes) [Clo+99]. Such spatial and temporal coherence conditions are provided by synchrotron radiation. 3D virtual histology via X-ray phase-contrast is an established technique in the synchrotron community and realised at several beamlines e.g. ID19 (ESRF) [Wei+10; Cho+22b], TOMCAT (SLS) [Sta+10; Bor+21], ANATOMIX (SOLEIL) [Wei+17; Rod+21] and BM05 (ESRF) [Wal+21]. Although each setup differs in X-ray energy, monochromaticity (bending magnet/wiggler/undulator), covered object size or supported propagation distance, a rough differentiation between microtomography and nanotomography is reasonable. Microtomographic setups exploit a parallel beam geometry and the resolution is given by the detector pixel size. In that configuration, the highest resolutions are mostly obtained by microscope X-ray detectors with a sensor pixel size of 6.5  $\mu\text{m}$  and a 10x microscope objective resulting in an effective pixel size of 650 nm. On the other hand, nanotomographic setups rely on a cone beam geometry

e.g. Holotomography at the GINIX (DESY) [Töp+18; Eck+20; Rei+21; Eck+21b], ID16 (ESRF) [Kua+20; Bar+22] or ptychography at the cSAXS (PSI) [Die+10; Hol+19]. The effective pixel size is based on geometrical magnification. Pixel sizes of sub-100 nm are routinely achieved at these setups. In this work the *GINIX* endstation is extended to combine micro- and nanotomography in one setup by switching from a parallel beam to cone beam configuration.

The outline of this work is as follows. **Chapter 2** provides the theoretical background essential for this work. The results section is divided into the three realized scales of the multi-scale approach, starting with the largest length scale and ending with the smallest scale. Each result chapter contains an own motivation and discussion. **Chapter 3** describes the realisation of the microtomography setup based on a parallel beam geometry. **Chapter 4** discusses recent upgrades of the waveguide-based cone beam setup. **Chapter 5** demonstrates the potential to reconstruct 3D volumes at super-resolution compared to the standard approach by using a novel acquisition and reconstruction approach. **Chapter 6** concludes this work and discusses future directions.

# From basic X-ray interaction to 3D virtual histology

---

# 2

This chapter outlines the key concepts of the underlying physics related to this work. Starting point is the interaction of X-rays with matter, followed by X-ray propagation, detection and phase retrieval of in-line holography. The transition from 2D images to 3D reconstruction volumes is explained by the basics of tomography. Current exemplary approaches of 3D virtual histology are presented at the end. The following textbook literature contains in-depth descriptions of the concepts [AM11; Buz11; SAA17; Pag06].

## 2.1 X-ray interaction with matter

In principle, when X-ray photons interact with matter, it can be attributed to two main processes, namely absorption and scattering. Both phenomena will be first explained by considering photons as particles. Then, the complex index of refraction is introduced, which describes the interaction by mean of a wave representation. The wavelength of X-rays are in the range of 0.01-10 nm and the interaction mostly relates to the electrons of the interacting atoms.

**Absorption** If the photon energy of an X-ray photon is higher than the binding energy of a bound atomic electron, the photon can be absorbed by the atom. The energy transfer ejects the bound electron from the atom, which is thereby ionized. This process is called *Photoelectric absorption*. The electron vacancy is filled by electrons from higher orbitals resulting in the emission of a photon with a characteristic energy (the difference between the two energy levels) or the emission of an Auger electron. In a wave picture, the absorption of photons results in a decrease of the X-ray intensity and is described by the Beer-Lambert law:

$$I(z) = I_0 \cdot e^{-\mu z}. \quad (2.1)$$

Here,  $I_0$  is the incident intensity,  $I(z)$  the beam intensity at the distance  $z$  and  $\mu$  the linear attenuation coefficient, which depends on the atomic number  $Z$  of the medium and the X-ray photon energy  $E_{ph}$  as follows [AM11]:

$$\mu(E_{ph}, Z) \propto \frac{Z^4}{E_{ph}^3}.$$

Besides this relation, *absorption edges* occur at specific energies when the emission of additional electrons become possible. At these energies, the attenuation coefficient increases discontinuously (edge).

**Scattering** The scattering of an X-ray photon on the atomic electrons is differentiated in elastic (coherent) or inelastic (incoherent) scattering. Elastic scattering describes the scattering process with unchanged photon energy. It is referred to as *Thomson scattering* if the photon frequency is above the resonance frequency of the scattering particle and *Rayleigh scattering* if the photon frequencies is below the resonance frequency. At low photon energies, this is the predominant effect. At higher photon energies, inelastic scattering is predominant, where the photon transfers energy to the scattering electron. This process is known as *Compton scattering*. Thomson scattering is the physical basis of refraction [SAA17] and can be expressed by the index of refraction  $n$ :

$$n = 1 - \delta. \quad (2.2)$$

Here,  $\delta$  is the refractive decrement and is related to the number density of electrons  $\rho$  as follows [AM11]:

$$\delta = \frac{2\pi\rho r_0}{k^2},$$

where  $k$  is the wave vector and  $r_0$  is the Thomson scattering length.

**Complex index of refraction** Refraction and absorption of a wavefield in matter can be expressed by the complex index of refraction  $n$  as illustrated in Fig. 2.1. So far, the index of refraction in Eq. (2.2) considers only the effect of scattering by the refractive decrement  $\delta$ . To also consider attenuation of the wavefield the real-valued



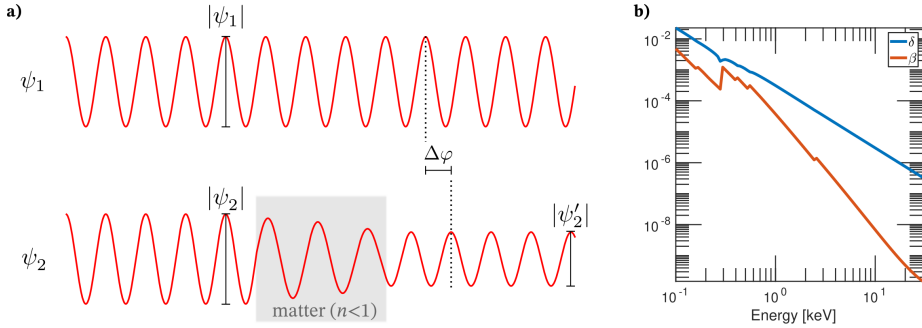


**Fig. 2.1:** Illustration of the X-ray matter interaction by means of the complex index of refraction. (a) Top: Monochromatic wave  $\psi_1$  in vacuum. Bottom: Monochromatic wave  $\psi_2$  interacting with matter. The interaction introduces a phase shift  $\Delta\varphi$  and an amplitude decrease  $|\psi'_2| < |\psi_2|$ . (b) Energy dependence of the refractive decrement  $\delta$  and the extinction coefficient  $\beta$  for the example of soft tissue, represented by the empirical chemical formula of a protein  $H_{50}C_{30}N_9O_{10}S_1$  and a density of  $1.35 \text{ g cm}^{-3}$  from [How+09]. While the overall interaction decreases with increasing X-ray energy, except for absorption edges, the  $\delta/\beta$ -ratio increases. Values obtained from [CXR].

extinction coefficient  $\beta$  is added as an imaginary term to  $n$ :

$$n = 1 - \delta + i\beta. \quad (2.3)$$

Inserting Eq. (2.3) into the wavefield of a plane wave  $\psi$  in matter leads to the following expression:

$$\psi(z) = e^{inkz} = e^{ikz} \cdot e^{-i\delta kz} \cdot e^{-\beta kz}.$$

Here,  $k$  is the wavenumber and  $z$  the propagation distance. The argument of the complex wavefield  $\arg(\psi)$  is the phase of the wave. Thus, the relative phase shift  $\Delta\varphi$  introduced by the interaction is defined as

$$\Delta\varphi = -\delta kz,$$

while the amplitude is given by

$$|\psi| = e^{-\beta kz}.$$

Since the intensity is the absolute squared root of the wavefield ( $|\psi|^2 = I$ ),  $\beta$  relates to

the linear attenuation coefficient  $\mu$  from (2.1) by  $\beta = \frac{\mu}{2k}$ . Figure 2.1b shows the energy dependence of  $\beta$  and  $\delta$  for an example protein as a representative for soft tissue.

**Projection approximation** If parallel propagating X-rays are weakly scattered within the interacting object, their propagation direction is assumed to be unchanged. Thus, the change in amplitude and phase can be projected onto a single plane, which is set to the end of the object. With the integrated decrement  $\bar{\delta} = \int_0^z \delta dz$  and the integrated extinction  $\bar{\beta} = \int_0^z \beta dz$  the exit wavefield behind the object  $\psi(z)$  is expressed by the *object transmission function*  $O(z)$  multiplied by the illumination wavefield  $P(z)$ . This approximation is called *projection approximation* [Pag06].

$$\psi(z) = P(z) \cdot O(z) \quad \text{with} \quad O(z) := e^{-k\bar{\beta} \cdot z} \cdot e^{-ik\bar{\delta}z} = e^{-\mu - i\varphi} \quad (2.4)$$

## 2.2 In-line holography

In 1948, Dennis Gabor proposed a novel lenseless imaging setup, which was later called *Holography* [Gab48]. The exit wavefield  $\psi = P \cdot O$  obtained by Eq. (2.4) propagates to the detection plane without any optical components in the free space. The detected image or signal, which is referred to as the **hologram**, is interpreted as the sum of a reference wavefield  $\psi_0$  and a scattered wavefield  $\psi_S$ .

$$I = |\psi_0 + \psi_S|^2$$

Since both wavefields share the same optical axis, the hologram is called an *in-line* hologram. The object reconstruction requires only the scattered wavefield, which can be separated from the reference wavefield, if it is known. However, often the reference wavefield is unknown and the reconstruction of the object is not trivial. To this end, many different approaches exist to reconstruct the object transmission function.

This section describes the free space wave propagation, followed by the signal detection, the phase problem and ends with the phase retrieval of the object.

### 2.2.1 Free space propagation

A description for the wavefield propagation in free space can be derived by solving the paraxial Helmholtz equation, which assumes a wavefield  $\Psi(x, y, z) = e^{ikz} \cdot \psi(x, y, z)$  with a slowly varying envelope  $\psi(x, y, z)$ :

$$\left[ 2ik \frac{\partial}{\partial z} + \nabla_{x,y}^2 \right] \psi(x, y, z) = 0.$$

**Fresnel propagation** The solution of this partial differential equation is given by the *Fresnel diffraction integral* [Gre82; Goo05], which is:

$$\begin{aligned} & \psi(x, y, z > 0) \\ &= -\frac{ik \exp(ikz)}{2\pi z} \int \int_{-\infty}^{\infty} \psi(x_0, y_0, z = 0) \exp \left[ \frac{ik}{2z} \left[ (x - x_0)^2 + (y - y_0)^2 \right] \right] dx_0 dy_0. \end{aligned}$$

It describes the wavefield propagation of paraxial waves from the plane  $(x_0, y_0, z = 0)$  to the plane  $(x, y, z > 0)$ . This propagation equation can be written as a convolution

$$\begin{aligned} \psi(x, y, z > 0) &= \psi_{z=0}(x, y) * \mathcal{H}_z(x, y) \\ &= \int \int_{-\infty}^{\infty} \psi_{z=0}(x_0, y_0) \mathcal{H}_z(x - x_0, y - y_0) dx_0 dy_0 \end{aligned}$$

with the convolution kernel:

$$\mathcal{H}_z(x, y) = -\frac{ike^{ikz}}{2\pi z} \cdot e^{\left[ \frac{ik}{2z}(x^2 + y^2) \right]}.$$

Thus, the wavefield propagation from  $z = 0$  to  $z > 0$  is given by:

$$\psi(x, y, z) = \mathcal{F}^{-1} \left[ \hat{\mathcal{H}}_z \cdot \mathcal{F}(\psi(x, y, z = 0)) \right],$$

with the reciprocal kernel  $\hat{\mathcal{H}}_z$ :

$$\hat{\mathcal{H}}_z = e^{\left[\frac{-iz}{2k}(k_x^2 + k_y^2)\right]}.$$

To this end, the Fresnel propagator  $\mathcal{F}_r(\cdot)$  is denoted as:

$$\psi(x, y, z) = \mathcal{F}^{-1} \left[ e^{\left[\frac{-iz}{2k}(k_x^2 + k_y^2)\right]} \cdot \mathcal{F}(\psi(x, y, 0)) \right] =: \mathcal{F}_r[\psi(x, y, 0)]. \quad (2.5)$$

**Fresnel number** A rearrangement of the Fresnel diffraction integral supports the introduction of the dimensionless *Fresnel number*  $F$ :

$$\begin{aligned} & \psi(x, y, z > 0) \\ &= -\frac{ik \exp(ikz)}{2\pi z} \int \int_{-\infty}^{\infty} \psi(x_0, y_0, z = 0) \exp \left[ \frac{ik}{2z} \left[ (x - x_0)^2 + (y - y_0)^2 \right] \right] dx_0 dy_0 \\ &= -\frac{ik \exp(ikz)}{2\pi z} \exp \left[ \frac{ik}{2z} (x^2 + y^2) \right] \\ & \quad \cdot \int \int_{-\infty}^{\infty} \psi(x_0, y_0, z = 0) \exp \left[ \frac{-ik}{z} (xx_0 + yy_0) \right] \underbrace{\exp \left[ \frac{ik}{2z} (x_0^2 + y_0^2) \right]}_{\text{chirp}} dx_0 dy_0. \end{aligned}$$

This notation consists of a single Fourier transform of the wavefield  $\psi(x_0, y_0, 0)$  and the chirp function  $\exp \left[ \frac{ik}{2z} (x_0^2 + y_0^2) \right]$ . The argument of the chirp function scales with the Fresnel number:

$$F := \frac{a^2}{\lambda z},$$

where  $a$  is chosen to represent a typical structure size and is therefore assumed to be the pixel size of the detector. The Fresnel number describes the influence of the chirp function on the propagation. For  $F \approx 1$  the propagation is called the *near-field* or *Fresnel* regime, since the chirp function affects the propagation.

**Fraunhofer propagation** For  $F \ll 1$ , the chirp function becomes unity and is therefore negligible. This propagation regime is referred to as the *far-field* or *Fraunhofer*

regime. To this end, the far-field propagation is described by a single Fourier transform with the corresponding spatial frequencies  $x = x_0/\lambda z$  [Goo05].

$$\begin{aligned} \psi_z(x, y) &= \underbrace{-\frac{ik \exp(ikz)}{2\pi z} \exp\left[\frac{ik}{2z}(x^2 + y^2)\right]}_{=\text{complex prefactor}} \mathcal{F}[\psi_{z=0}(x_0, y_0)] \\ &\propto \mathcal{F}[\psi_{z=0}(x_0, y_0)] \end{aligned} \quad (2.6)$$

### 2.2.2 Intensity measurement and approximations

**Detection and phase problem** X-ray detectors measure the beam intensity  $I$  in the detection plane  $z_{det}$ . The phase information of the propagated wavefield  $\psi(z_{det})$  is lost in the detection process, since the measured intensity is the squared modulus of the propagated wavefield:

$$\begin{aligned} I &= |\psi(z_{det})|^2 = |\mathcal{F}_r[\psi(z_{obj})]|^2 \\ &= |\mathcal{F}_r[P(z_{obj}) \cdot O(z_{obj})]|^2 \\ &= |\mathcal{F}_r[P(z_{obj}) \cdot e^{-i\varphi - \mu}]|^2. \end{aligned}$$

Here,  $\psi(z_{obj}) = P(z_{obj}) \cdot O(z_{obj})$  is the object exit wavefield and  $\mathcal{F}_r$  the Fresnel propagator. The recovery of the objects phase  $\varphi$  is an ill-posed inverse problem, which is solved by phase retrieval algorithms as discussed later. Prior to the phase reconstruction, two common simplifications are discussed.

**Flat-field correction** In order to reconstruct the object transmission function  $O$  from the exit wavefield of the object  $\psi = P \cdot O$ , it needs to be separated from the illumination wavefield  $P$ , which is typically unknown. However, the propagated illumination function  $|\mathcal{F}_r[P(z_{obj})]|^2$  can be measured by moving the object out of the X-ray beam. To this end, a common simplification in in-line X-ray holography is the *Flat-field correction* or *Empty-beam division*. It is the division of the recorded hologram by the intensity pattern of the empty beam. Thus, the assumption is that the corrected hologram approximates the propagated object transmission function:

$$\frac{|\mathcal{F}_r [P(z_{obj}) \cdot e^{-i\varphi-\mu}]|^2}{|\mathcal{F}_r [P(z_{obj})]|^2} \approx |\mathcal{F}_r [e^{-i\varphi-\mu}]|^2.$$

This assumption is quite accurate for smooth illumination wavefields, while it fails for structured illumination wavefields  $P$  [Hag+14; Hom+15]. Ideally, the complex-valued illumination wavefield  $P$  and the wavefield  $P \cdot O$  are reconstructed simultaneously, since a division of both in the object plane results in the object transmission function  $O$ .

**Fresnel scaling theorem** Often, the illumination function is a point source with divergent radiation. The Fresnel scaling theorem [Pag06] states that a point source illumination  $\psi(z_{01})$  at a large distance  $z_{01}$  can be described by an equivalent plane wave illumination with effective variables. The application of the paraxial approximation to a spherical wave results in:

$$\psi(z_{01}) = e^{ikr} = e^{ik\sqrt{x^2+y^2+z_{01}^2}} \approx e^{ikz_{01}} \cdot e^{\frac{ik}{2z_{01}}(x^2+y^2)}$$

The propagation from  $z_{01}$  to  $z_{02}$  with  $z_{12} = z_{02} - z_{01}$  is obtained by inserting the illumination wavefield  $\psi(z_{01})$  into the Fresnel diffraction integral:

$$\begin{aligned} & \psi(z_{02} > z_{01}) \\ &= -\frac{ik \exp(ikz_{12})}{2\pi z_{12}} \exp\left[\frac{ik}{2z_{12}}(x^2+y^2)\right] \cdot \int \int_{-\infty}^{\infty} e^{ikz_{01}} \\ & \cdot \exp\left[\underbrace{\frac{-ik}{z}(xx_0 + yy_0)}_{=-\frac{ik}{z_{eff}}(x_{eff}x_0 + y_{eff}y_0)}\right] \exp\left[\underbrace{\frac{ik}{2}(x_0^2 + y_0^2)\left(\frac{1}{z_{01}} + \frac{1}{z_{12}}\right)}_{=\frac{ik}{2z_{eff}}(x_0^2 + y_0^2)}\right] dx_0 dy_0. \end{aligned}$$

In this form the propagation of the spherical wave is given by an equivalent plane wave propagation with the scaled effective variables  $\frac{x}{M} = x_{eff}$ ,  $\frac{y}{M} = y_{eff}$  and  $\frac{z_{12}}{M} = z_{eff}$ .  $M$  is the geometrical magnification obtained by the distances  $z_{01}$  and  $z_{02}$ :

$$M = \frac{z_{02}}{z_{01}}.$$

### 2.2.3 Phase retrieval

Different approaches to reconstruct the objects phase from the measured intensities exist, e.g. see [Loh+20a]. However, a prominent approach for in-line X-ray holography and most relevant for this thesis is based on the *contrast transfer function (CTF)*.

**CTF-based approach** The assumptions of a weakly interacting object (weak absorption  $\mu \ll 1$  and small phase-gradients  $\Delta\varphi \ll 1$ ) [Tur+04] allow for the linearization of  $I = |\mathcal{F}_r [e^{-i\varphi - \mu}]|^2$ , which leads to the contrast transfer function (CTF) as derived in [Mar19]. The CTF describes the contributions of the objects phase shift  $\varphi$  and absorption  $\mu$  to the measured intensity contrast in the reciprocal space, denoted by the “ $\sim$ ” symbol.

$$\frac{\tilde{I}(k_x, k_y, z)}{I_0} = \delta_D(k_x, k_y) + 2\tilde{\varphi} \sin \chi - \tilde{\mu} \cos \chi.$$

The intensity in reciprocal space  $\tilde{I}$  divided by the empty-beam intensity  $I_0$  is given by the delta function  $\delta_D(k_x, k_y)$ , a sine weighted phase term ( $2\tilde{\varphi} \sin \chi$ ) and a cosine weighted absorption term ( $\tilde{\mu} \cos \chi$ ) with the reduced spatial frequencies  $\chi = \frac{\lambda z k_{\perp}}{4\pi}$ .

The minimization of the error function  $S_C$

$$S_C = \frac{1}{N} \sum_{m=1}^N \int |\tilde{I}_{exp,m}(k_{\perp}) - \tilde{I}_{theo,m}(k_{\perp})|^2 dk_{\perp}$$

of the expected intensity  $\tilde{I}_{theo}$  and the measured intensity  $\tilde{I}_{exp}$  is obtained by setting the derivative with respect to  $\tilde{\varphi}$  to zero  $\frac{\partial S_C}{\partial \tilde{\varphi}} = 0$ . Taking measurements at multiple distances accounts for the zero crossings of the sine filter [Zab+05]. The CTF reconstruction formula for the objects phase  $\varphi$  is obtained by assuming a homogeneous object ( $\frac{\beta}{\delta} = \text{const.}$ ):

$$\varphi = \mathcal{F}_{\perp}^{-1} \left[ \frac{\sum_{m=1}^N \left( \sin \chi + \frac{\beta}{\delta} \cos \chi \right) \cdot \mathcal{F}_{\perp}(I_{exp}(x, y) - 1)}{\sum_{m=1}^N 2 \cdot \left( \sin \chi + \frac{\beta}{\delta} \cos \chi \right)^2 + \alpha(k_{\perp})} \right].$$

This CTF-based phase retrieval is a single step algorithm with a frequency-dependent regularization parameter  $\alpha(k_{\perp})$ , which effects high and low frequencies separately [Töp18].

**Iterative phase retrieval** Another approach to reconstruct the phase of the object transmission function  $O$  is given by iterative reconstruction schemes based on the method of alternating projections. The wavefield of the object transmission function  $O$  is propagated between the detection and the reconstruction plane, while applying constraints to the wavefield in each plane. The constraint in the detection plane is given by the measured amplitude of the wavefield  $\sqrt{I} = |\psi|$ . Thus, the amplitude of the propagated wavefield is replaced by the measured amplitude in the detection plane, which is known as the magnitude projector  $\mathcal{P}_1$ . The constraint in the reconstruction plane  $\mathcal{P}_2$  requires prior knowledge of the object and depends on the reconstruction approach. One iteration reads as follows:

$$\psi_{n+1} = \mathcal{P}_2 \left[ \mathcal{F}_r^{-1} \left[ \mathcal{P}_1 \left[ \mathcal{F}_r \left[ \psi_n \right] \right] \right] \right].$$

Prominent examples of such alternating projection reconstruction methods are the Gerchberg-Saxton (GS)[Ger72], the Error-reduction (ER)[Fie82], the Hybrid-Input-Output (HIO) algorithm [Fie82] or the relaxed averaged alternating reflection (RAAR) algorithm [Luk04]. In the GS approach, intensities are measured in two different planes. In that case, the prior knowledge in the reconstruction plane is the measured intensity. Thus, the constraint in the reconstruction plane becomes another magnitude constraint. The constraint in the reconstruction plane of the ER is a support constraint. Here, the prior knowledge is the limited size of the object. Areas of the wavefield that do not interact with the object are set to zero. In the HIO approach, an adapted support constraint is exploited in the reconstruction plane. Areas next to the object are set to values, which are obtained by a linear combination of the input and the output wavefield. Issues of concern for iterative phase retrieval algorithms are the initialization, convergence, numerical efficiency, and stagnation [SAA17]. Alternating



projection algorithms can be applied to different wavefields with different constraints. For example, the investigated wavefield can be the exit wavefield of the object  $\psi = P \cdot O$ , the wavefield of the illumination  $P$  or the empty-beam corrected wavefield  $\mathcal{F}_r(O)$ . Different propagation operators can be applied, e.g. Fresnel Eq. (2.5) or Fraunhofer Eq. (2.6). In addition, the used constraints can be adapted depending on the prior knowledge of the measurement.

### 2.2.4 In-line holography resolution

By considering an effective parallel beam geometry, the resolution of in-line holography is limited by the numerical aperture of the setup as well as by the effective pixel size  $p_{eff} = \frac{p}{M}$ . The resolution limit  $d_{res}$  given by diffraction can be determined by the wavelength  $\lambda$ , the distance between sample and detector  $z$  and the size of the hologram  $D$  [Lat19]:

$$d_{res} = \frac{\lambda z}{D}.$$

The resolution in a typical propagation-based X-ray phase-contrast experiment for virtual histology is limited by the effective pixel size, as a large field of view is preferred to high resolution. Exemplary acquisition parameters are  $z = 4975$  mm,  $D = 2560 \cdot 6.5 \mu\text{m} = 16.6$  mm and  $\lambda = 8.9841 \times 10^{-11}$  m, which results in an effective pixel size of  $p_{eff} = 159.3$  nm. With these parameters, the resolution limit given by diffraction is  $res_{125mm} = 26.9$  nm. In order to match the effective pixel size and the resolution limited by diffraction, the magnification need to be increased by placing the object closer to the source. At a source-to-sample distance of  $z_{01} = 21.5$  mm effective pixel size and resolution limited by diffraction are  $res = p_{eff} = 27.4$  nm.

## 2.3 Basics of tomography

Computed tomography is a non-invasive technique that allows the reconstruction of the three dimensional structure of an object by acquiring projections at different angles. The reconstruction is performed digitally by filtering and subsequent back projecting the acquired projections. This chapter outlines the basic aspects of tomography, further details can be found in [Buz11; SAA17].

**Radon transform** The fundamental concept of computed tomography is the *radon transform* [Rad17]. It is the mathematical description of the image acquisition process in the experiment. Consider a 2D function  $f(x, y)$  (the object), which is illuminated under an angle  $\alpha$  by X-rays. The absorption and phase shifts are integrated in the direction  $\alpha$ , which results in a 1D profile  $p_\alpha(s)$  of the object, known as the *projection* of the object:

$$p_\alpha(s) = \mathcal{R}_\alpha f(s) := \int_{\mathbb{R}^2} f(x, y) \delta(x \cos \alpha + y \sin \alpha - s) dx dy.$$

The acquisition of many projections can be plotted against the angle  $\alpha$ , which results in a sinogram  $P(\alpha, s)$ . The object  $f(x, y)$  can be reconstructed from this sinogram by the *inverse radon transform*  $\mathcal{R}^{-1}$ :

$$f(x, y) = \mathcal{R}^{-1}(P(\alpha, s)).$$

The realisation of the inverse radon transform is outlined in the following.

**Fourier slice theorem** The one-dimensional Fourier transform of the projection  $p_\alpha$  results in a line through the 2D Fourier transformed function  $f(k_x, k_y)$  at the angle  $\alpha$ . This relation is called the *Fourier slice theorem* [Nat01]:

$$\tilde{p}_\alpha(k_s) = \mathcal{F}_s(\mathcal{R}_\alpha f)(k_s) = \tilde{f}(k_s \cos \alpha, k_s \sin \alpha).$$

By filling the 2D Fourier space with the recorded projections of all angles, the function  $f(x, y)$  can be reconstructed by an inverse Fourier transform  $\mathcal{F}^{-1}$ . However, this filling of the Fourier space projects the  $\tilde{p}_\alpha(k_s)$  onto a rectangular grid, instead of a polar grid. Due to the required interpolation between the discrete grid points, the subsequent inverse Fourier transform can result in severe reconstruction artifacts [KS01]. To this end, another implementation of the inverse radon transform is more accurate.

**Filtered backprojection** A simple partial back projection of the radon transforms at the according angle (2.7) results in a blurred reconstruction of the object, since the sampling density of the low spatial frequencies is higher compared to the density of the high spatial frequencies.

$$f(x, y) \approx \mathcal{R}^{-1}p(x, y) = \int_0^\pi p_\alpha(x \cos \alpha + y \sin \alpha) d\alpha \quad (2.7)$$

The consideration of the Fourier transformed object function  $\tilde{f}(k_x, k_y)$  in polar coordinates  $(k_x, k_y) = (k_s \cos \alpha, k_s \sin \alpha)$  and the application of the Fourier slice theorem yield that a back projection of filtered projections results in a more accurate reconstruction of the object  $f(x, y)$ :

$$\begin{aligned} f(x, y) &= \frac{1}{\sqrt{2\pi}} \int_0^\pi \int_{-\infty}^\infty \tilde{f}(k_s \cos \alpha, k_s \sin \alpha) \cdot |k_s| \cdot e^{i(xk_s \cos \alpha + yk_s \sin \alpha)} dk_s d\alpha \\ &= \frac{1}{\sqrt{2\pi}} \int_0^\pi \int_{-\infty}^\infty \tilde{p}_\alpha(k_s) \cdot \tilde{\mathcal{H}}(k_s) \cdot e^{i(xk_s \cos \alpha + yk_s \sin \alpha)} dk_s d\alpha. \end{aligned}$$

A multiplication of the reciprocal projections  $\tilde{p}_\alpha(k_s)$  with the filter kernel  $\tilde{\mathcal{H}} = |k_s|$ , which amplifies high spatial frequencies and is known as the *Ram-Lak* filter, results in the filtered projections  $p_\alpha^F(s)$ .

$$p_\alpha^F(s) = \mathcal{F}^{-1} \left[ \tilde{\mathcal{H}}(k_s) \mathcal{F}(p_\alpha(s)) \right]$$

The back projection of the filtered projections over all angles  $\alpha$  results in a sharp reconstruction of the object  $f(x, y)$

$$f(x, y) = \int_0^\pi p^F(x \cos \theta + z \sin \theta) d\theta$$

and is referred to as *filtered back projection*.

**Artifacts** In real world experiments, tomography is accompanied by artifacts for manifold reasons, e.g. a misaligned rotational axis, a flawed pixel response of the detector, motion of the object or an inaccurate beam geometry. Two tomographic artifacts of special interest for this work are outlined in the following. A detailed descriptions of tomographic artifacts is provided in the literature, e.g. [Buz11; SAA17; Töp18].

**Sampling** Tomographic artifacts occur if the angular sampling is insufficient. A minimum number of  $N$  angles is required to avoid sampling artifacts for an object size of  $N_{px}$  pixels within an angular range of  $\alpha \in [0, 180]^\circ$  [Buz11]:

$$N = N_{px} \frac{\pi}{2}.$$

In addition, if the angular increment  $\Delta\alpha$  of the measurement and the reconstruction differ from each other, severe tomographic artifacts are introduced. This mismatch can occur in continuous tomographic scans, where the absolute position of the rotational axis is unknown. Fig. 2.2 illustrates the introduced artifacts if e.g. the angular increment is assumed to be  $0.305^\circ$  instead of  $0.3^\circ$ . The artifact strength increases from the center towards the borders.

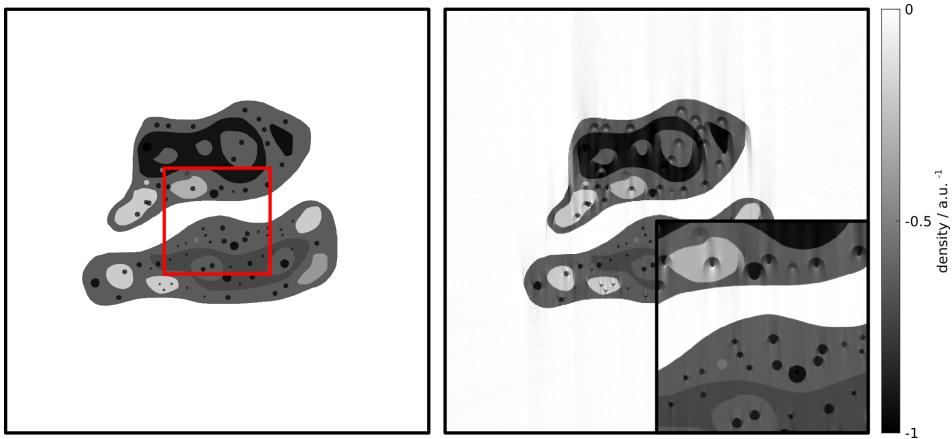


**Fig. 2.2:** Tomographic artifacts introduced by a wrong angular increment  $\Delta\alpha$  in the reconstruction. The left image shows the used phantom. The reconstruction in the right is obtained by an angular increment of  $0.305^\circ$  instead of  $0.3^\circ$  within  $\alpha \in [0, 180]^\circ$ . The inset highlights severe reconstruction artifacts.

**Local tomography** In high resolution tomographic scans, it is often the case that the sample size is larger than the detectors field of view. This results in the acquisition of *truncated projections* and is referred to as region-of-interest (ROI), interior or local tomography. The reconstruction of ROI-tomographic scans can result in artifacts, due to structures outside the field of view. If features with high image contrast are partially or entirely outside the field of view, shape artifacts occur [MA96]. However, this is not

the case for propagation-based phase-contrast ROI-tomography of soft tissue, since the objects are weakly interacting. More importantly, the reconstructed mean gray values of the reconstruction differ from the correct gray values. Artifacts appear in the form of a global elevation towards the edges, which is known as peripheral glow [Ohn+00]. An approach to overcome these artifacts is to extend the sinogram by replicating the edge values [Kyr+11] of the sinogram. This corrects for the peripheral glow, however, the reconstructed gray values depend on the extent of the sinogram padding. To this end, ROI-tomography reconstructions provide only relative gray value changes. An approach to correct for incorrect gray values is presented in [RFS20] based on iterative back-projection and re-projection and the assumption of an approximately cylindrical shaped sample with general homogeneity.

## 2.4 3D virtual histology

The application of propagation-based X-ray phase-contrast tomography on low absorbing samples such as biological tissue provides 3D reconstructions with sufficient image contrast to visualize single cells. To this end, it is very suitable for 3D virtual histology and is performed at laboratory setups as well as at synchrotron beamlines as presented in the following examples.

State-of-the-art laboratory setups have provided excellent results. [Våg+18] showed the application of 3D virtual histology to intact coronary artery autopsy samples at cellular resolution. In [Alb+18] the application of propagation-based phase-contrast to a standard benchtop microCT was demonstrated on the example of mouse lung tissue. The application to image human hippocampal tissue affected by Alzheimer's disease [Töp+20], cardiac tissue from patients who succumbed to Covid-19 [Rei+21] and tissue of human and murine cerebral cortex [Eck+21c] was also demonstrated at laboratory setups.

State-of-the-art synchrotron setups are able to study the morphology and composition changes of murine brains due to the preparation steps of conventional histology [Rod+21; Rod+22]. Myelinated axons in rodent and human brain tissue are investigated in [Cho+22a; Cho+22b]. The 3D imaging of human cerebellum and neocortex specimens is demonstrated in [Khi+18]. Pulmonary disease studies in animal models are performed in [Bor+21]. In [Cas+11] propagation-based X-ray phase-contrast tomography is exploited for mammography with synchrotron radiation facilitates. Recently, intact human organs (brain, lung, heart, kidney and spleen) were imaged

in-vitro from the organ to the cellular scale in three dimensions by hierarchical phase-contrast tomography (HiP-CT) [Wal+21]. 3D virtual histology obtained by an X-ray waveguide-based cone beam geometry is demonstrated on human cerebellum biopsies [Töp+18; Eck+21b], on Covid-19 affected human lung tissue [Eck+20] and on Covid-19 affected human cardiac tissue [Rei+21].

# Multi-scale approach (Scale I): Fast parallel beam tomography

---

# 3

## 3.1 Motivation

In histology, the study of tissue, optical microscopes are utilized to investigate tissue sections of a few micrometer thickness. Starting with the lowest magnification of the microscope, the specimen is first inspected in its entirety. It reveals the general shape and morphology of the tissue. This overview image is crucial, since severe pathological changes are already visible on that scale. Areas of special interest can then be investigated in more detail at higher resolution. The magnification can be increased by changing the objectives of the microscope, usually up to 40x or 100x. This provides excellent images in 2D and is the gold standard method in pathology departments.

The disadvantage of this conventional histology is the physical sectioning of the sample. Firstly, the position and orientation of the slicing predetermine the interpretation of the whole specimen. Secondly, the sectioning is invasive, which hampers further investigations with other methods. Finally, the 3D information about the sample structure is either unavailable or the 3D resolution is limited in one direction by the slice thickness.

The possibility to investigate tissues on an overview scale and certain regions in higher resolution is referred to as **multi-scale approach** and was implemented at the *GINIX* endstation in this work. To this end, a setup for tomographic scans on a larger scale was implemented in a **parallel beam** geometry with a beam size of  $\sim 1.6 \text{ mm} \times 1.4 \text{ mm}$ , additional to the existing high resolution waveguide-based holotomography setup (Ch. 4).

The parallel beam setup provides the 3D information of millimeter sized samples with isotropic resolution, which is considered as **virtual 3D histology**. This enables the characterization and quantification of the tissue morphology in 3D. Importantly, this is not possible in the waveguide-based holotomography setup alone due to the small

field of view and it would be very labour intensive without an isotropic 3D resolution in conventional histology.

Propagation-based X-ray phase-contrast **microtomography setups** in parallel beam geometry are available at other synchrotron beamlines, e.g. ID19 (ESRF) [Wei+10; Cho+22b], TOMCAT (SLS) [Sta+10; Bor+21], SYRMEP (ELETTRA) [Dul+21] and BM05 (ESRF) [Wal+21]. Contrary to the *GINIX*, each beamline is designed especially for parallel beam microtomography, further optimized and equipped for certain applications, e.g. fast tomography at the TOMCAT. The multi-scale acquisition scheme, sometimes referred to as **hierarchical imaging**, is realized by different detectors within one setup or by decreasing the effective pixel size via optical magnification of the scintillator image. Highest resolution in these setups is achieved by 10x magnification at 6.5  $\mu\text{m}$  pixel size. The unique characteristic of the *GINIX* endstation is to increase the resolution via geometrical magnification by switching from parallel beam to cone beam setup (25x-100x magnification) and the usage of a Si(111) monochromator with  $\frac{\Delta\lambda}{\lambda} = 1 \times 10^{-4}$  [Kal12].

The possibilities to characterize and quantify the tissue samples in 3D are enormous. To this end, an important step is to define meaningful metrics constrained by the scientific questions on the investigated tissue. The 3D analysis and metric calculation can be either applied on the reconstructed electron densities (direct) or on segmentations of the reconstructed volumes (indirect). The segmentation itself can be very challenging. It ranges from manual segmentation by experts over simple threshold-based segmentation, to edge detection and blob finding algorithms, to deep learning networks trained on manual segmentations [CV01; RFB15; MNA16; Ber+19a].

In the following chapter, three cases for the application and potential of 3D virtual histology obtained by the PB setup are presented. First, the potential to support daily clinical routines is shown on the example of punch biopsies of tumorous human pancreatic tissue biopsies embedded in paraffin. Volumetric information as well as a large series of neighboring histological slices can support e.g. the classification of tumor stages and thereby the decision on treatment strategy. Second, analysing the 3D tissue morphology of post mortem tissues may provide additional information to understand the fatality mechanisms at cellular level. This can be of particular interest for novel diseases as demonstrated for the novel Covid-19 disease. Finally, 3D virtual histology is very promising for preclinical studies on large sample quantities due to the high sample throughput. This could improve the statistics of studies and therefore their significance. Furthermore, it facilitates studies on temporal evolution of tissue or



differently treated tissue. A preclinical study on ischemic stroke in mouse models is presented here.

## 3.2 Experimental realization

*This section is based on the publication "3D virtual histology of human pancreatic tissue by multiscale phase-contrast X-ray tomography" [Fro+20a] and quotes extracts from it. It covers the realization of the parallel beam setup at the synchrotron endstation GINIX.*

The **GINIX** endstation (Göttingen Instrument for Nano Imaging with coherent X-rays) at the P10 coherence beamline at the PETRA III storage ring at DESY (Hamburg) can be operated in the medium-hard X-ray regime of 5-20 keV. Since 2020 the U29 undulator was replaced by a 5 m long U32 undulator offering tunable X-ray energies without an energy gap between the 1st and the 3rd undulator harmonic. The undulator creates an X-ray source spot of  $36\ \mu\text{m} \times 6\ \mu\text{m}$  size ( $h \times v, 1\sigma$ ) with a divergence of  $28\ \mu\text{rad} \times 4\ \mu\text{rad}$  ( $h \times v, 1\sigma$ ) in low- $\beta$  setting. As reported in [Sal+15], the GINIX endstation offers different X-ray experimental setups: Scanning nanobeam diffraction, ptychography and waveguide-based holotomography. This pool of setups is extended by a **fast parallel beam tomography setup (PB)** for propagation-based phase-contrast tomography in a parallel beam geometry. For this configuration, all X-ray optics are moved out of the beam and the quasi-parallel beam is used. The setup is illustrated in Fig. 3.1 and the setup parameters are listed in Tab. 3.1.

The beam is monochromatized by either a Si(111) channel-cut (CC) or a Si(111) double-crystal monochromator (DCM) to improve the temporal coherence. The CC provides a much higher angular stability, while the DCM can operate in a larger energy range and offers an energy independent beam position offset, which is beneficial for energy varying scans. During this work the CC was used.

The beam size was maximized by opening all beam size defining slits. The abbreviations refer to the respective names in the *SPEC* control software of the GINIX or the *SPOCK* control software of the P10:

1. gslt1 ( $2\ \text{mm} \times 2\ \text{mm}$ , P10)
2. uslt1 ( $4\ \text{mm} \times 3\ \text{mm}$ , P10)
3. uslt2 ( $4\ \text{mm} \times 2\ \text{mm}$ , P10)
4. g2 ( $2\ \text{mm} \times 2\ \text{mm}$ , GINIX)

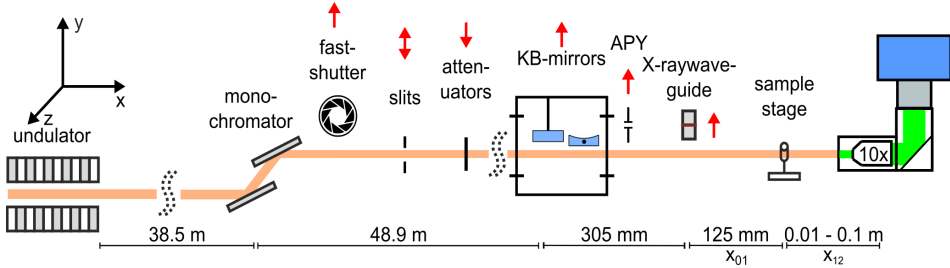


**Fig. 3.1:** Experimental realization of the parallel beam tomography setup at the GINIX endstation. The X-ray beam is monochromatized by either a Si(111) channel-cut or a Si(111) double-crystal monochromator. Fastshutter, KB-mirrors, Aperture (APY) and X-ray waveguide are moved out of the beam path. Beam size defining slits are opened. Attenuators are moved into the beam path. The sample to detector distance is 10-100 mm. An X-ray microscope system converts the X-rays into optical light by a  $50\ \mu\text{m}$  thick LuAG:Ce scintillator. The scintillator image is magnified by an 10x optical objective and acquired by the sCMOS camera pco.edge, resulting in an effective pixel size of  $0.65\ \mu\text{m}$ . Figure adapted from [Fro+20a].

##### 5. skb ( $2\ \text{mm} \times 2\ \text{mm}$ , GINIX)

The Kirkpatrick–Baez mirrors (KB) are installed in a vacuum chamber and are translated by moving the entire vacuum chamber. Entry and exit window are  $75\ \mu\text{m}$  thick single crystal diamond apertures of  $4.5\ \text{mm}$  diameter (Applied Diamond, Wilmington, USA). In order to let the KB-reflected X-ray beam (reflection angle  $8\ \text{mrad}$ ) pass through, entry and exit windows are displaced laterally with respect to the beam direction. As a consequence, the horizontally reflecting mirror as well as the exit window cut into the beam path of the parallel beam at first. By rotating the optical table of the GINIX (*otzrot* motor) the beam path through the KB chamber can be adjusted.

**Table 3.1:** Experimental parameters of the parallel beam setup.

	Parallel geometry
FOV	$1.6\ \text{mm} \times 1.4\ \text{mm}$
Pixel size	$650\ \text{nm}$
$x_{01}$	-
$x_{12}$	$10\ \text{mm} - 100\ \text{mm}$
Regime	direct contrast
Rotation	continuous
Exposure	$0.035\ \text{s}$
Total exposure	$75\ \text{s}$
Volumetric flowrate	$4.07 \times 10^7\ \mu\text{m}^3\ \text{s}^{-1}$

The high photon flux of  $5 \times 10^6$  photon/s/ $\mu\text{m}^2$  at 8 keV and  $2 \times 10^6$  photon/s/ $\mu\text{m}^2$  at 13.8 keV enables the possibility of fast tomographic scans. The total acquisition time was reduced by changing the acquisition scheme from step and shoot to a continuous scheme (Sec.3.2.3 for details). The optical sCMOS camera *pco.edge 5.5* (PCO, Kelheim, Germany) provides the necessary camera readout speed with a maximum frame rate of 100 fps and a pixel size of  $6.5 \mu\text{m}$ . It was mounted on a X-ray microscope system (Optique Peter, Lentilly, France), which converts the X-rays into optical light ( $\lambda = 535 \text{ nm}$ ) by an  $50 \mu\text{m}$  thick LuAG:Ce scintillator. The image is magnified by one of the three microscope objectives mounted in a objective turret (2x, 10x and 20x). The 10x objective results in an effective pixel size of  $0.65 \mu\text{m}$  and a field of view of  $1.6 \text{ mm} \times 1.4 \text{ mm}$  that covers the entire X-ray beam. The working distance between scintillator and objective is controlled by a step motor and needs to be adjusted prior to the experiment. The 10x objective in combination with the  $50 \mu\text{m}$  LuAG:Ce scintillator (both exchangeable) lead to saturated images without any absorber at 35 ms exposure time. To prevent scintillator and sample damage due to the beam intensity the beam is attenuated. The beamline provides two different absorber systems. The absorber system of the GINIX setup consists of  $100 \mu\text{m}$  aluminium ( $E < 10 \text{ keV}$ ) and  $50 \mu\text{m}$  molybdenum ( $E > 10 \text{ keV}$ ) foils, which are strongly structured and therefore unsuitable for full-field X-ray imaging. Instead, for the PB setup the second absorber system is used, since the  $25 \mu\text{m}$  single crystal silicon ( $E < 10 \text{ keV}$ ) and  $25 \mu\text{m}$  silver ( $E > 10 \text{ keV}$ ) foils show less features. The total attenuation is determined by the amount of foils, e.g.  $4 \times 25 \mu\text{m}$  silicon foils were used for scans at 8 keV. At an acquisition time of 35 ms, the fastshutter (Cedrat technologies) movement is too slow. It was moved out of the beam and the beam is controlled by the safety shutter (*SPEC: osh/csh*) only. It stays open during the tomographic scan. The two beam position monitors foils *mon1g* & *mon2g* need to be moved out of the beam path as well (*SPEC: umv mon1g/mon2g 15*), since they create a structured beam profile. The propagation distance between sample and detector  $x_{12}$  ranges from  $x_{12,min} = 10 \text{ mm}$  to  $x_{12,max} = 500 \text{ mm}$ , limited by the GINIX design. The effect of  $x_{12}$  on the image quality will be discussed in detail in Sec.3.2.1. Good reconstructions were obtained at propagation distances of  $x_{12} < 100 \text{ mm}$ . The Fresnel numbers range from  $F \approx 0.5$  for 13.8 keV at 10 mm propagation distance to  $F \approx 0.025$  for 8 keV at 100 mm propagation distance. At these Fresnel numbers the image formation transitions from the direct contrast regime towards the holographic regime. Exemplary images of the X-ray illumination in the PB setup are shown in Fig. 3.2 for 8 keV (a)/(c) and 13.8 keV (b)/(d), both acquired at *run94* (April 2020) with the channel-cut monochromator. At both energies, the illumination is homogeneous

overall in their logarithmic representation. Note that for 13.8 keV the KB window as well as the KB-mirror cut into the beam path, as marked by the arrows in Fig. 3.2 b). The linear representation reveals the beam profile and its inhomogeneities. The diffraction pattern of the features suggests their origin in the beam path. Weakly diffracted features are close to the detector as for example the structures on the KB window in the inset of Fig. 3.2 c) while highly diffracted features are further upstream such as the one depicted in the inset of Fig. 3.2 d). Tomographic scans are acquired with the following scan parameters: 1500 projections over 180° at 20 Hz frame rate (35 ms exposure + 15 ms readout time). This results in a total acquisition time of 75 s at a volumetric flow rate of:

$$\frac{V}{t} = \frac{\pi \cdot (1280 \cdot 0.65 \mu\text{m})^2 \cdot (2160 \cdot 0.65 \mu\text{m})}{75 \text{ second}} = 4.07 \times 10^7 \mu\text{m}^3 \text{ s}^{-1}.$$

**Switching from parallel beam to waveguide setup** The detailed switch from the PB setup to the WG setup is as follows:

1. move KB in (e.g. umvr kby -1.5 / kbz -1)
2. move WG in (e.g. umvr pody -3000)
3. move APY in (e.g. umvr apy -12)
4. move pilatus in
5. remove protective lead foil in front of flight tube
6. move GINIX absorber in (e.g. att 15)
7. move pco.edge out (e.g. umvr mdety 200)
8. move oav out (e.g. umvr oavz 40)
9. move sample tower in (e.g. umv stx 125)
10. move p10 abs out (SPOCK: p10\_abs 0)
11. move p10 fastshutter in (SPOCK: p10\_fastshutter in)
12. enable slow shutter (SPOCK: p10\_cssh)
13. move beam monitor in (e.g. umv mon1g/mon2g 0)
14. move hayrot (e.g. umvr hayrot -224  $\hat{=}$  -8 mrad).

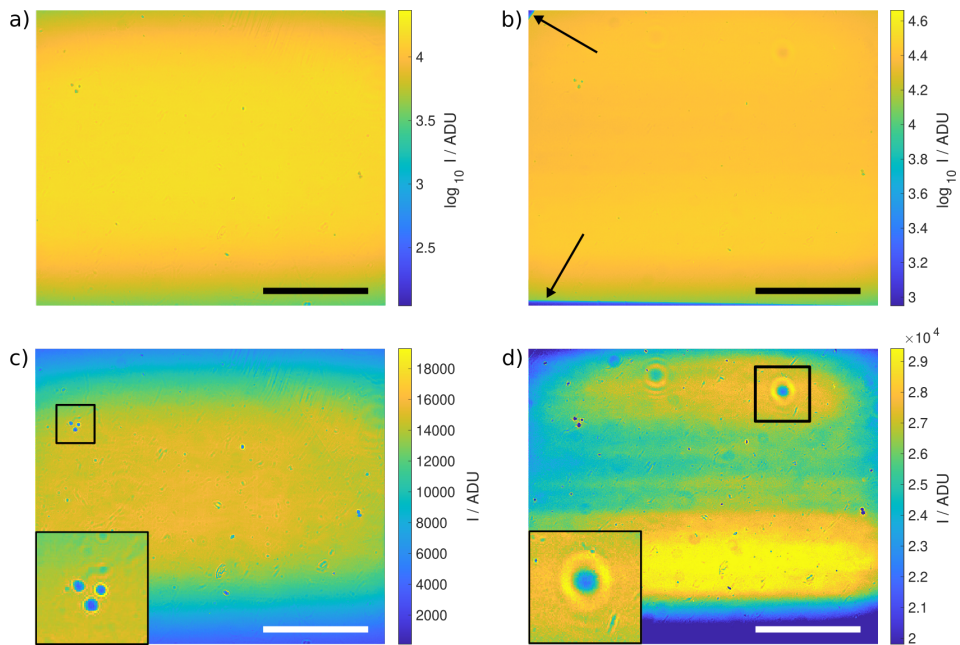


**Fig. 3.2:** X-ray flat field images of the parallel beam setup for two different X-ray energies. a) Logarithmic flat field at 8 keV. b) Logarithmic flat field at 13.8 keV. Black arrows mark the KB-window (top left) and the vertical KB-mirror (bottom) cutting into the beam path. c) Linear flat field at 8 keV. The inset shows three weakly diffracted features sticking at the diamond window of the KB tank. d) Linear flat field at 13.8 keV. The inset shows a highly diffracted feature sticking at one of the attenuation foils positioned further upstream in the X-ray beam. Scale bars: 500  $\mu\text{m}$ .

### 3.2.1 Propagation distance

To investigate the effect of the propagation distance on image formation, phase reconstruction and image quality, tomograms at four different propagation distances  $x_{12} \in \{10 \text{ mm}, 30 \text{ mm}, 40 \text{ mm}, 100 \text{ mm}\}$  between object and detector are acquired at  $E = 8 \text{ keV}$ . The sample is a 1 mm punch biopsy of unstained paraffin embedded human pancreatic tissue. Figure 3.3 depicts the projections of the four distances at the same rotation angle. With increasing propagation distance the phase contrast becomes more visible in form of intensified interference fringes, e.g. fine structures within the sample become more pronounced.

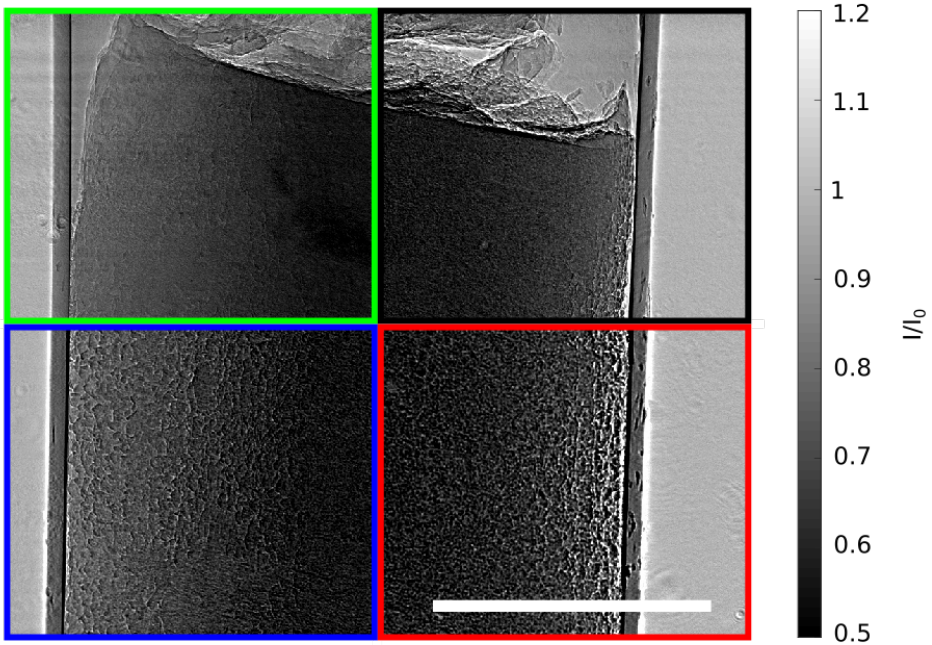


**Fig. 3.3:** Empty-beam corrected projections of an unstained human pancreatic tissue sample at four different propagation distances acquired in the parallel beam setup. Green:  $x_{12}=10 \text{ mm}$  ( $F_{10} = 0.2726$ ). Black:  $x_{12}=30 \text{ mm}$  ( $F_{30} = 0.0909$ ). Blue:  $x_{12}=50 \text{ mm}$  ( $F_{50} = 0.0545$ ). Red:  $x_{12}=100 \text{ mm}$  ( $F_{100} = 0.0273$ ). Phase-contrast in form of constructive interference increases with decreasing Fresnel number and finer structures become more visible. Scale bar  $500 \mu\text{m}$ . Adapted from [Fro+20a].

The observed increase in phase contrast with increasing propagation distance is also visible in the power spectral density (PSD) of the four projections. Here, the change in

the image formation corresponds to the number of oscillations in the PSDs, which is in good agreement with the theory of the contrast transfer function (Ch. 2.2.3). With increasing propagation distance, the oscillation period decreases and the number of minima increases, as shown in Fig. 3.4. The propagation distance  $x_{12}=10$  mm shows zero minima,  $x_{12}=30$  mm one minimum,  $x_{12}=50$  mm two minima and  $x_{12}=100$  mm five minima. The increasing number of minima in the PSD indicates the transition from the *direct contrast* regime at  $x_{12}=10$  mm towards the holographic regime.

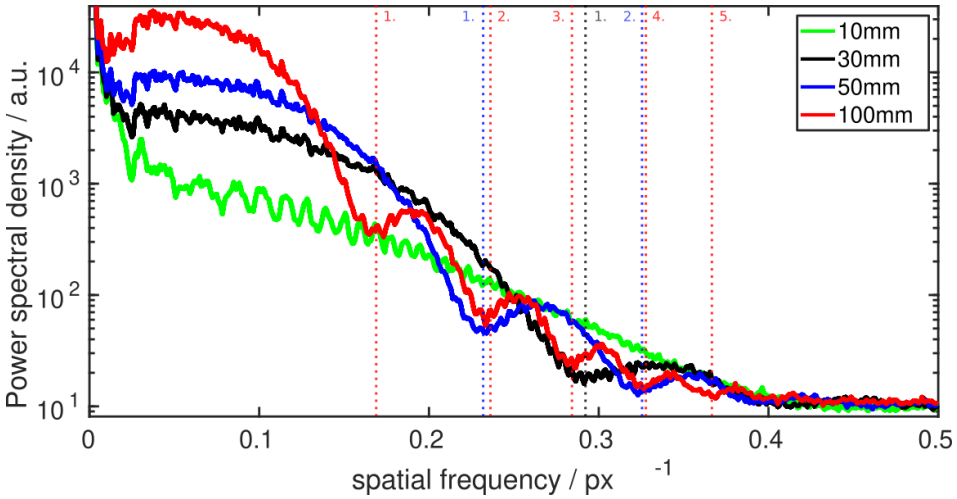


**Fig. 3.4:** Power spectral density of the four projections in Fig.3.3. Variation of the propagation distance indicates the transition from the *direct contrast* regime at  $x_{12}=10$  mm towards the holographic regime, as more minima are emerging. 0 minima for  $x_{12}=10$  mm, 1 minimum for  $x_{12}=30$  mm, 2 minima for  $x_{12}=50$  mm and 5 minima for  $x_{12}=100$  mm. Low spatial frequencies increase with increasing propagation distance while high frequencies remain similar.

For each distance 1500 projections are acquired over an angular range of  $\Theta = 0 - 180^\circ$ . First, the phase shift of each projection of the four distances is reconstructed via the CTF approach. The reconstruction parameters are  $lim1 = 0$ ,  $lim2 = 0.1$  and  $\frac{\delta}{\beta} = 30$ . An exemplary empty-beam corrected projection at 100 mm propagation distance and the corresponding phase reconstruction is shown in Fig.3.6 a). The edge enhancement at the surrounding kapton tube as well as the interference fringes at the interfaces within the sample are corrected. After the phase reconstruction, the tomographic reconstruction is performed via filtered back projection. An exemplary xy-slice of the tomographic reconstruction at the propagation distance of 100 mm is shown in Fig.3.6 b). The characteristic glandular structure of the pancreatic tissue can be recognised.

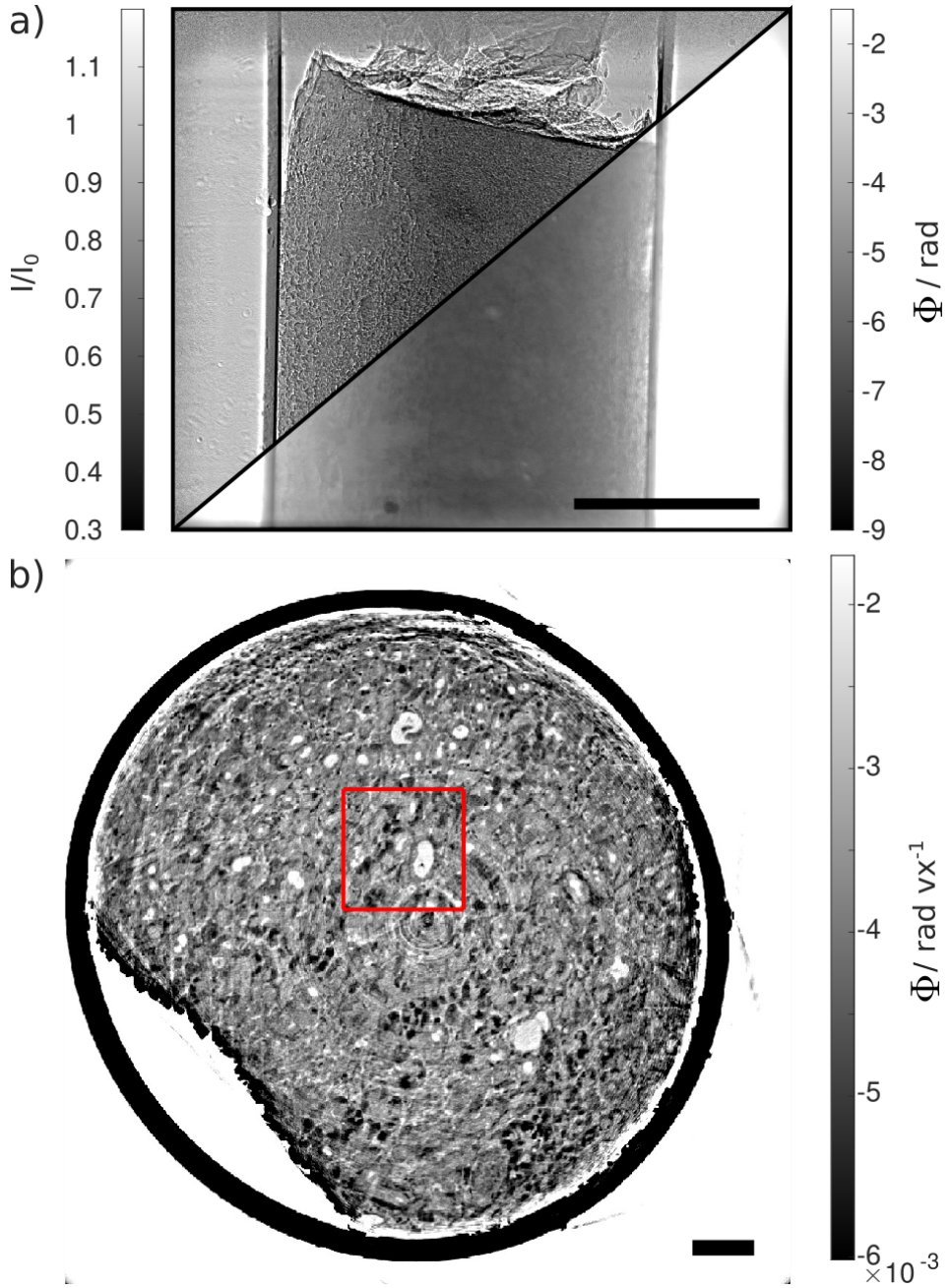
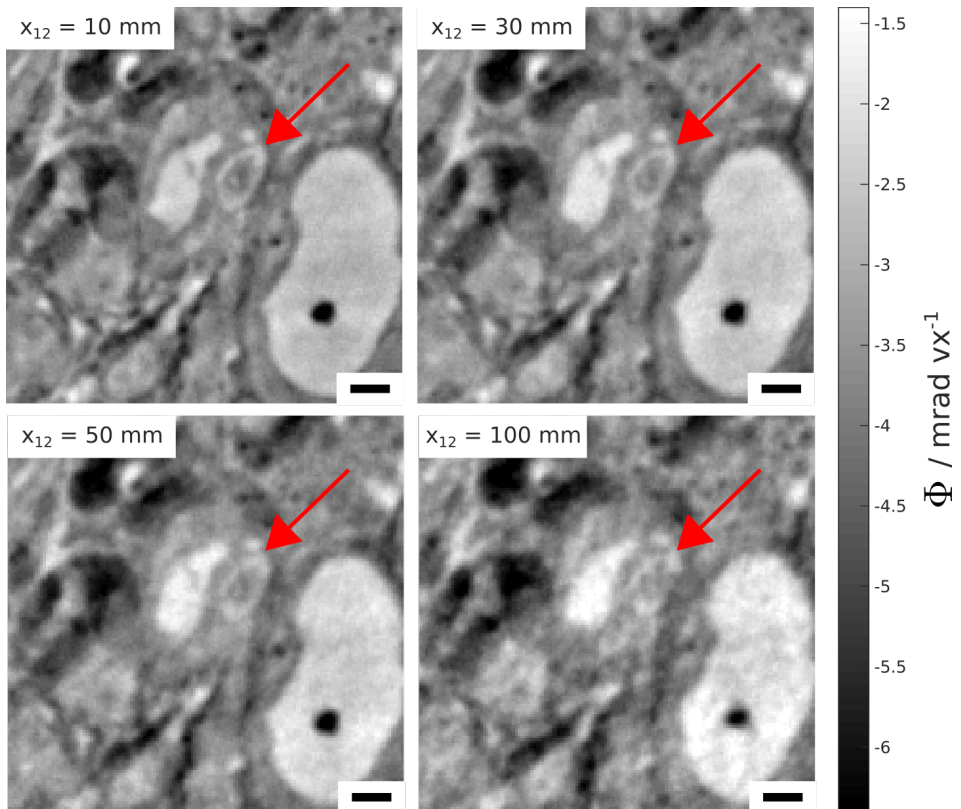


Fig. 3.5: (caption next page)



**Fig. 3.5 (previous page):** Reconstruction of the objects phase and tomographic reconstruction of a 1 mm punch biopsy of unstained tumorous human pancreatic tissue. (a) Top: Exemplary empty-beam corrected projection at  $x_{12}=100$  mm. Bottom: Reconstructed phase of the object via CTF-approach with the reconstruction parameters  $lim1 = 0$ ,  $lim2 = 0.1$  and  $\frac{\delta}{\beta} = 30$ . (b) Exemplary xy-slice of the tomographic reconstruction. The red rectangle marks the magnified area shown in Fig. 3.6. Scale bar: a)  $500 \mu\text{m}$  and b)  $100 \mu\text{m}$ .

A magnified view of the marked area is shown in Fig. 3.6 for the four distances. Unexpectedly, the image quality decreases in this measurement with increasing propagation distance. The reconstruction becomes noisy and less sharp with increasing propagation distance. An exemplary feature is marked by the red arrow and highlights this effect. To this end, the origin must lie in the experimental setup. The spatial coherence of the setup as an explanation of the effect is excluded, as discussed in the next chapter (3.2.2). One possible explanation could be the fact, that the phase of the illumination function deviates from the assumed plane wave illumination. Small phase variations of the X-ray illumination, which are possibly introduced by vibrations of the monochromator, become more visible with increasing propagation distance. To this end, these phase variations, which are reconstructed at larger propagation distances, result in object artifacts within the reconstructed slice. As a follow-up experiment, the phase of the illumination wavefield should be measured to prove or disprove this conjecture.



**Fig. 3.6:** Effect of increasing propagation distance on the tomographic reconstruction in the parallel beam setup of the *GINIX*. The red marked area of Fig. 3.5 is shown for the four distances. With increasing propagation distance the reconstruction becomes less sharp and the noise level increases, as highlighted by the feature marked with the red arrow. Scale bar  $10 \mu\text{m}$ .

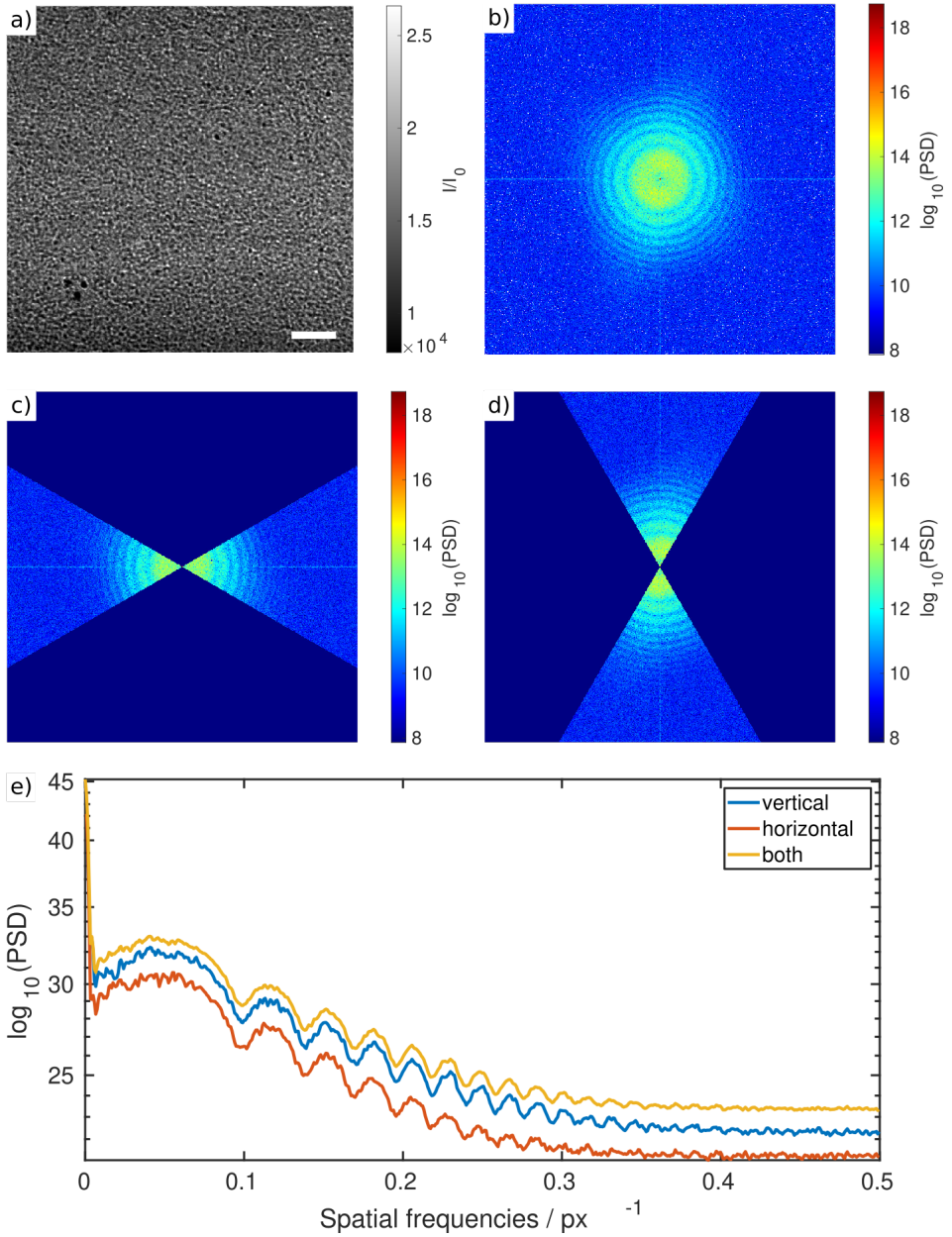
### 3.2.2 Spatial coherence

With increasing propagation distance, additional and finer interference fringes occur from the objects interfaces. This effect is reflected in form of additional oscillations within the power spectral density of the empty-beam corrected projection, as illustrated in Fig. 3.4. In the case of insufficient spatial coherence of the X-ray beam, these fine fringes and the corresponding oscillations at higher spatial frequencies would be suppressed. Figure 3.4 does not indicate if the spatial coherence already suppresses the formation of interference fringes at the propagation distance of 100 mm. To check if the number of oscillations within a PSD at a larger propagation distance increases, a tomogram of a 3 mm punch biopsy of unstained paraffin embedded human pancreatic tissue was acquired at the maximum propagation distance of 500 mm. An exemplary empty-beam corrected projection and its PSD are shown in Fig. 3.7 a) and b), respectively. In the case of a limiting degree of spatial coherence, an asymmetry between the vertical and the horizontal directions should be present in the PSD, due to the asymmetrical spot size of the X-ray beam ( $36 \mu\text{m} \times 6 \mu\text{m}$ ). To this end, the angular average of  $\pm 30^\circ$  in horizontal and vertical directions is determined, as illustrated in c) and d). The angular averaged PSDs differ in the amount of oscillations, as depicted in e). The horizontal direction (red) shows 9 oscillations while the PSD in the vertical direction shows 12 (blue) oscillations. The angular average of the entire PSD (yellow) shows 11 oscillations. Note, that the graphs are shifted vertically for visibility purposes. This leads to the conclusion that the spatial coherence in the horizontal direction limits the formation of interference fringes at 500 mm propagation distance. Furthermore, since at least 9 oscillations are observable in the direction of lower spatial coherence, the image quality of reconstruction at 100 mm propagation distance is not limited by the coherence.

### 3.2.3 Continuous tomography

The **step and shoot** scheme is the conventional method of tomographic acquisition at the GINIX. After the rotation of the tomographic axis by the angle increment  $\Delta\theta$ , the motor stops and an image is acquired. This is repeated for each of the  $N$  images. The actual acquisition time per image is given by the exposure time and the overhead time, which includes the following additional times:

1. Rotation step ( $\sim 0.2$  s)
2. Motor position readout ( $\sim 0.1$  s)

**Fig. 3.7:** (caption next page)

**Fig. 3.7 (previous page):** The asymmetry of the spatial coherence of the parallel beam at the *GINIX*. a) An exemplary empty-beam corrected projection of a 3 mm punch biopsy of unstained paraffin embedded human pancreatic tissue was acquired at the maximum propagation distance of 500 mm at 13.8 keV. b) The power spectral density of a) shows the sinusoidal behavior of the CTF's phase contribution. c) and d) show the regions for the calculation of the vertical and horizontal part of the PSD, respectively. e) Vertical (blue), horizontal (red) and total (yellow) averaged PSDs show a different number of oscillations, which reflects the asymmetric spatial coherence of the X-ray beam in horizontal and vertical direction, due to the asymmetric beam size. Graphs are shifted vertically for visibility purposes. Scale bar: 100  $\mu\text{m}$ .

### 3. Image save and feedback:

- a) local SSD: ( $\sim 0.1$  s)
- b) network: ( $\sim 0.3$ - $0.5$  s)

In order to reduce the overhead time, a **continuous** acquisition scheme was implemented. The additional time from the motor movement in form of starts and stops is circumvented by this continuous rotation. Meanwhile, motor positions are not read out for each angular position software-wise (SPEC) and the absolute motor positions are missing. For tomography relative angle positions are sufficient, which are calculated from the rotation velocity. The overhead time caused by saving the images on a local Solid-State-Drive (SSD) is negligible. The time consuming part here is the feedback to the command software SPEC for each image. Omitting the feedback by changing the camera control from a software trigger (SPEC) to an external trigger generated by a field programmable gate array (FPGA) further reduces the overhead. The exposure time per image is dictated by the trigger pulse length. In this scheme, the image acquisition and the rotation of the tomographic axis are independent parallel processes, as illustrated in Fig. 3.8.

The control software SPEC starts the axis rotation a few seconds before the first trigger pulse to ensure a constant rotation velocity after the initial acceleration. The rotation velocity in terms of SPEC units is calculated as follows:

$$1 \text{ Hz} = 9000 \text{ steps} = 9000 \text{ steps} \cdot 200 \text{ int. unit steps}^{-1} = 1\,800\,000 \text{ int. unit}$$

The rotational stage uses an incremental rotary encoder, where one encoder step corresponds to the rotation of  $0.04^\circ$ , which results in 9000 steps per revolution. A typical SPEC command for an tomographic scan used during this work reads as:

`tomo_pco 3000 35 15`. This starts a tomographic scan with 3000 projections over  $360^\circ$  (angle increment  $\Delta\theta = 0.12^\circ$ ) with 35 ms exposure time and 15 ms readout time. Hence, the total acquisition time is 150 s with a rotation velocity of 12 000 int. unit at 20 Hz frame rate.

The overall overhead time in the continuous acquisition scheme is limited by acceleration and deceleration of the rotation axis and the readout time per image.

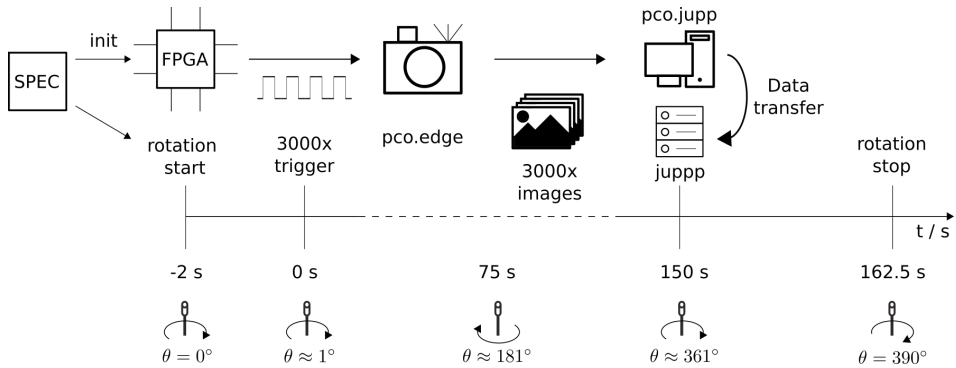


**Fig. 3.8:** Acquisition scheme of the continuous rotation in parallel beam configuration. Exemplary scan parameters: 3000 projections, angular range  $360^\circ$ , exposure time 35 ms, readout time 15 ms, frame rate 20 Hz. The command software SPEC sets up the trigger parameter for the camera and the delay for the FPGA and starts the rotation axis e.g. 2 s before the first trigger pulse to ensure a constant rotation velocity. Images are saved on the local SSD of the detector computer `pco.jupp`. Parallel to the image acquisition, already acquired images are transferred into the network folder by `juppp` (JUSt a Picture Pump Proxy). Rotation ends with an angular buffer at  $390^\circ$ .

### 3.3 Human pancreatic tissue

*This section is based on the publication "3D virtual histology of human pancreatic tissue by multiscale phase-contrast X-ray tomography" [Fro+20a] and quotes extracts from it. It covers the results on human pancreatic tissue obtained by the parallel beam setup at the synchrotron endstation GINIX.*

Pancreatic cancer is the fourth leading cause of cancer death and has the lowest 5-year relative survival rate of all cancer types, for example (9%) in the US [SMJ19]. The most common pancreatic tumor, pancreatic ductal adenocarcinoma (PDAC), accounts for about 90% of the cases and is characterized by an invasive mucin producing neo-

plasm of epithelial origin that causes an intense stromal desmoplastic reaction [Hru10]. Morphologic criteria such as irregular arrangement of tubular glands, embedded in desmoplastic stroma and signs of inflammation are characteristic features identified by conventional histology [HE19]. Understanding the mechanism of this disease in more detail is of high interest.

By adding a third dimension to the conventional histology more information are accessible and novel 3D quantification parameters can be introduced. This was demonstrated on paraffin embedded human tumor biopsies, obtained from surgery, at the PB setup of the GINIX endstation. Two characteristics of the 3D tissue analysis are highlighted.

**Islet of Langerhans** The *Islet of Langerhans* is a three-dimensional cluster of cells in the endocrine part of the pancreas. They consist of different hormone producing cells, e.g. the insulin producing *beta cells*, and release these hormones into the bodys blood flow. A deficiency in either the beta cell mass, which is the absolute number of beta cells in the pancreatic Islets of Langerhans, or the beta cell function, or both, can lead to insufficient levels of insulin, resulting in hyperglycemia and diabetes [Che+17]. The Islets of Langerhans differ from the overall glandular morphology of pancreatic tissue, the exocrine part of the pancreas, and are therefore rather easy to recognise. With the PB setup it is possible to investigate those Islets in their entirety in 3D, as shown in Fig.3.9. The exemplary Islet of Langerhans has a diameter of  $d_{islet} \approx 100 \mu\text{m}$  and the size of the inside cells is  $d_{cell} = 5\text{-}15 \mu\text{m}$ .

The segmentation was performed using the software `ilastik` [Ber+19b]. Cells located inside the Islet, shown in the reconstructed slice in Fig. 3.9(a), were segmented by interactively marking a few cells, followed by an automatic completion of the entire volume based on machine learning algorithms. Figure 3.9(b) shows the same xy-slice of the segmented volume. Segmentation comprises three tissue classes: 1 = high gray value stroma, 2 = low gray value stroma, 3 = cells. The segmentation step was completed by a masking step, to exclude false positive cells outside the Islet. Figure 3.9(c) shows a 3D rendering of all segmented cells located inside the Islet.

The segmented volume was then further analyzed with Matlab. Cells were registered using the Matlab function `bwconncomp()`, which identifies connected components in a binary image/volume. With an input parameter "Connectivity" of 6, which takes the 6 nearest voxel into account, 1309 single cells were counted inside the Islet of Langerhans without any corrections. Visual inspection shows that some segmentation components include more than one cell, due to a connection in the segmentation. To

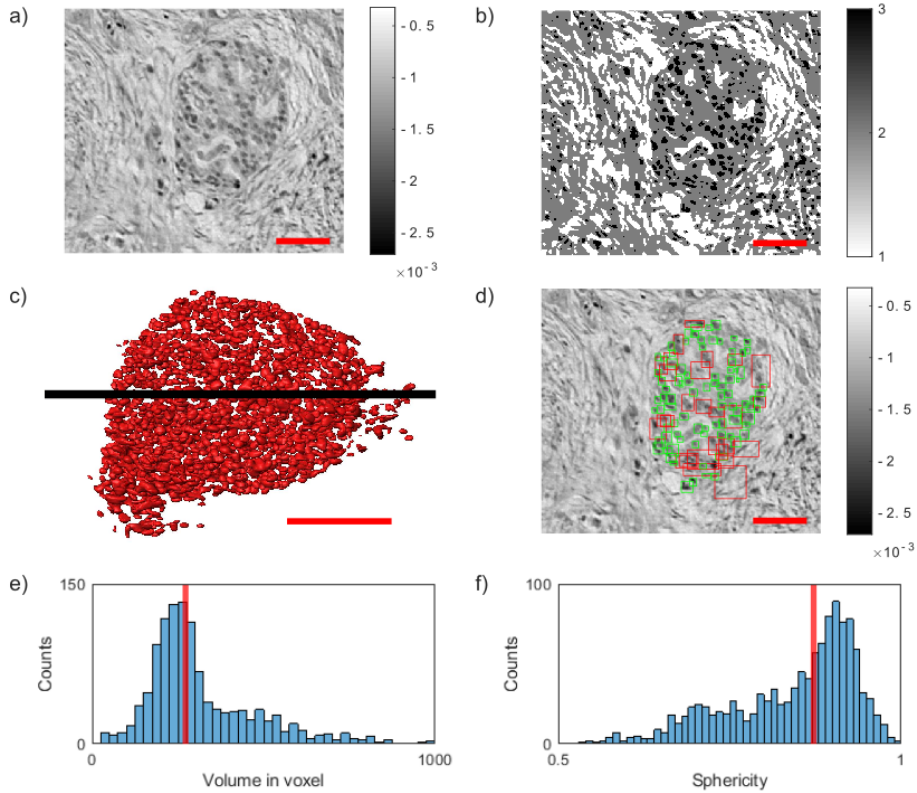


**Fig. 3.9:** a) Reconstructed slice in the xy plane of the PTA stained punch biopsy obtained by the parallel beam illumination. b) Pixel segmentation into 3 classes via *ilastik*. c) 3D rendering of the segmented cells located within the Islet of Langerhans by their manual selection. d) Boundary boxes of the segmented cells. Each squares mark one component. If the width of one component is larger than 20 px in one dimension, it is declared as false (red squares). Squares of components with the correct size are marked green. e) Cell volume distribution of the selected cells (green marked in d)). Note that the median volume size of a single cell is 271 vx. f) Distribution of the cell sphericity  $\Psi$  of the selected cells (green marked in d)). Note that the median cell sphericity is 0.87. Scale bars in a, b, c and d: 50  $\mu\text{m}$ . Adapted from [Fro+20a].



filter the connected cells out for the subsequent histograms, we introduced a volume threshold. Based on an estimated maximum cell size of 20 px (=13  $\mu\text{m}$ ), all cells with a larger size in one of the x-,y-,z-directions were subjected to a veto, as illustrated in Fig. 3.9(d). The squares represent the boundary boxes of each segmented component in 3D. Green squares contain connected binary components below 20 px width and red squares comprise larger connected components within the volume. In this way, 139 objects were found to be too large. In order to count the connected cells inside the larger objects (consisting of seemingly connected cells), we divided the corresponding volume of all segmented objects above threshold (224865 voxel) by the median volume of a single cell (271 voxel), obtained from the distribution of properly segmented cells (below threshold), as shown in Fig. 3.9(e). This led in this example to a total number of 2000 cells located within the Islet of Langerhans, which is in good agreement with the literature [WK18].

Volume, surface area and boundary boxes of each component were determined by using the Matlab function `regionprops3()`. As a further morphological measure, the sphericity of each cell was computed and calculated by the following definition [Wad32]:

$$\Psi = \frac{\pi^{1/3}(6 \cdot V_{cell})^{2/3}}{A_{cell}}$$

with the cell volume  $V_{cell}$  and the cell surface area  $A_{cell}$ . The sphericity distribution is shown in Fig. 3.9(f).

**Anisotropy parameter** Tumorous pancreatic tissue is characterized by an abundance of collagen fibers known as typical desmoplastic reaction (intratumoral fibrosis). Since fibers have a direction and do not cross each other, they create an anisotropy within the glandular structure of pancreatic tissue. To quantify the degree of fiber orientation e.g. corresponding to the degree to which the tissue is affected, the anisotropy parameter  $\Omega$  was introduced, defined as a scalar field. This anisotropy parameter was evaluated on two samples. **Sample A** was an unstained 1 mm punch biopsy taken from putative healthy tissue and **Sample B** was a PTA stained 1 mm punch biopsy, consisting mainly of tumor tissue. The description of the 3D analysis quotes [Fro+20a]: "  $\Omega$  describes the local degree of orientation for a chosen subvolume  $\Lambda_k$  centered around the voxel in question. Its value is based on the three eigenvalues  $\lambda_i$  of the structure tensor  $ST$  as in [Rei+19]. By shifting the subvolumes voxel-wise, every voxel of the tomographic volume can be allocated with an  $\Omega$ -value. The structure tensor can be defined as the sum (or average) over the subvolume  $\Lambda_k$  of the multiplication of the

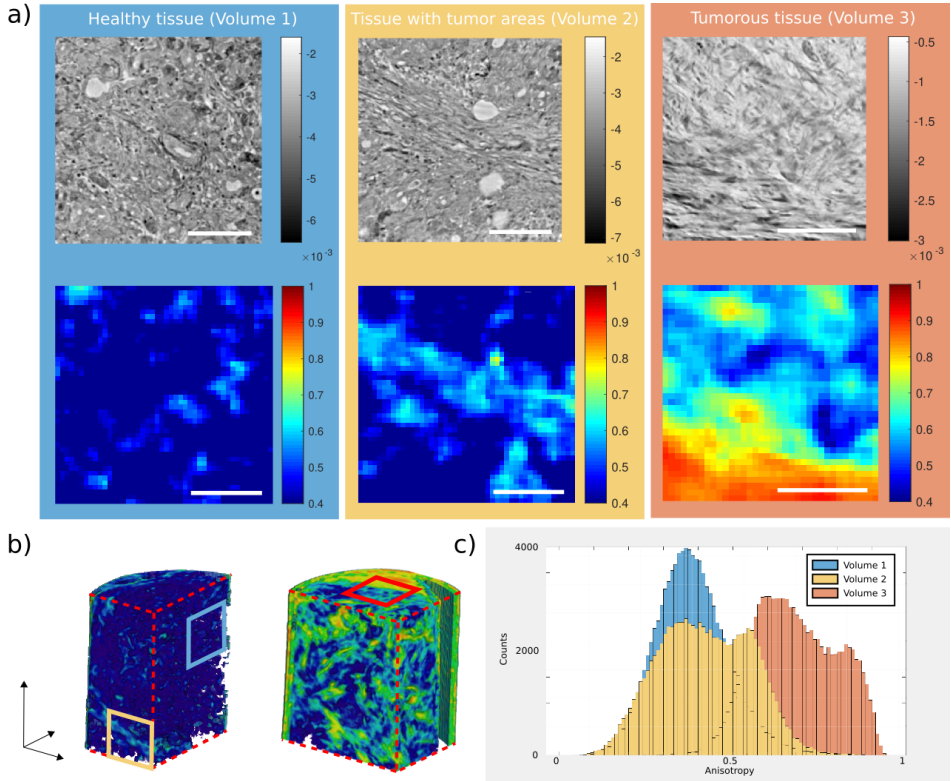


**Fig. 3.10:** Results of the anisotropy parameter  $\Omega$  for three example volumes of pancreatic tumor tissue. a) Virtual slices (top) obtained from the parallel beam configuration and corresponding anisotropy maps (bottom) for **Volume I**, containing mostly healthy, glandular tissue (blue), **Volume II**, containing partially tumorous tissue (yellow), and **Volume III**, containing mostly tumorous tissue with intratumoral fibrosis (red). Note that the blue and yellow marked slices were chosen from the 3D reconstruction of **Sample A**, while the red marked slice was chosen from the 3D reconstruction of **Sample B**. b) 3D visualization of the anisotropy parameter  $\Omega$  of **Sample A**. Blue and yellow frames mark the positions of the corresponding slices in a). c) Histograms of the three anisotropy volumes.  $\Omega$ -values of the histograms increase with the presence of collagen fibers inside the volume. Scale bars:  $100\ \mu\text{m}$ . Adapted from [Fro+20a].

intensity gradient components of each voxel

$$ST_{ij} = \sum_{x,y,z \in \Lambda_k} \partial_i I(x, y, z) \cdot \partial_j I(x, y, z)$$

from which the Eigenvalues  $\lambda_i$  are calculated by

$$ST \cdot b_i = \lambda_i \cdot b_i .$$

The anisotropy parameter  $\Omega$  can then be defined as

$$\Omega = \sqrt{\frac{\left[\frac{1}{\lambda_1} - \frac{1}{\lambda_2}\right]^2 + \left[\frac{1}{\lambda_2} - \frac{1}{\lambda_3}\right]^2 + \left[\frac{1}{\lambda_3} - \frac{1}{\lambda_1}\right]^2}{2 \cdot \left[\left(\frac{1}{\lambda_1}\right)^2 + \left(\frac{1}{\lambda_2}\right)^2 + \left(\frac{1}{\lambda_3}\right)^2\right]}}$$

$\Omega$  evaluates to 0 for an isotropic structure ( $\lambda_1 \approx \lambda_2 \approx \lambda_3$ ), while for a highly anisotropic structure ( $\lambda_1 \approx \lambda_2 \gg \lambda_3$ )  $\Omega$  converges to 1. For the following results  $\Lambda_k$  was chosen with subvolume size of 40 px<sup>3</sup>. Subvolume  $\Lambda_{k+1}$  was shifted by 10 px with respect to  $\Lambda_k$ , leading to a binning of the volume by a factor of 10.

The concept of the  $\Omega$  measure was demonstrated on three volumes with different collagen abundance:

- (I) volume containing mostly healthy tissue, consisting of glandular tissue (blue)
- (II) volume containing in part intratumoral fibrosis tissue (yellow)
- (III) volume containing large areas of intratumoral fibrosis tissue (red)

Due to the morphology of both samples, volume **I** & **II** were selected from the parallel beam reconstruction of **Sample A**, while volume **III** was selected from the parallel beam reconstruction of **Sample B**. Figure 3.10(a) shows the virtual slice from the parallel beam reconstruction (top), and the corresponding anisotropy map (bottom). The position within the biopsy for volume **I** & **II** is shown in Fig. 3.10(b), indicated by the colored frames. Visual inspection of the virtual slice and the corresponding anisotropy map demonstrate how the fibrous structures of the tumor are represented by an increased anisotropy parameter  $\Omega$ .

The three volumes were compared by their  $\Omega$ -histograms in Fig. 3.10(c). The histogram of the healthy tissue volume **I** is Gaussian distributed with a mean value of  $\bar{\Omega}_{healthy} = 0.38$  and a standard deviation of  $\sigma_{healthy} = 0.104$ . Volume **II** still contains healthy tissue, but the presence of collagen fibers increases as shown in the virtual slice, and

the distribution of the histogram is broadened and shifted towards higher  $\Omega$ -values ( $\bar{\Omega}_{partial} = 0.43$  &  $\sigma_{partial} = 0.132$ ). In the histogram of volume **III**, which contained mostly tumorous tissue, the  $\Omega$ -values of the histogram are further shifted to higher ( $\bar{\Omega}_{full} = 0.68$  &  $\sigma_{full} = 0.118$ ). These three examples indicate that the tissue volumes can be classified based on their  $\Omega$  histograms into different stages of affected tissue. The  $\Omega$ -values increased with the increased presence of fiber, as expected, and the average value  $\bar{\Omega}$  of a biopsy might therefore serve as a suitable biomarker to classify the tumor. To this end, future work should extend this analysis to a representative number of cases, and a validation based on correlative imaging technique.

### 3.4 Lung tissue from Covid-19 patients

*This section is based on the publication "3D virtual histology of human pancreatic tissue by multiscale phase-contrast X-ray tomography" with a shared first authorship of M.Eckermann, J.Frohn and M.Reichardt [Eck+20] and quotes extracts from it. It covers the results obtained by the parallel beam setup.*

To stop the Covid-19 pandemic, which emerged in March 2020 in Germany, a more detailed understanding of the disease is crucial. Phase-contrast tomography at the GINIX provides access to the 3D architecture on a cellular level. To this end, six postmortem lung samples from Covid-19 patients [Men+20] with the size of a few millimeters were scanned at the GINIX parallel beam setup. With that, propagation-based X-ray phase-contrast studies were performed on Covid-19 affected lung tissue for the first time [Eck+20]. In order to analyse the morphology of the samples in their entirety, the acquisition and reconstruction scheme was extended by a stitching approach. As respiratory failure was the reason for the majority of Covid-19 fatalities, the function of the lung to exchange oxygen was investigated by analysing the tissue to air distance in 3D.

**Stitching tomograms** The 3D reconstruction volume can be artificially extended by stitching several tomograms acquired at neighboring positions. Hence, it is possible to scan the lung samples in their entirety of a few millimeter size. The stitching acquisition scheme is illustrated in Fig. 3.11. The horizontal detector size of 1.6 mm leads to a reconstruction area of a circular slice with a radius of 0.8 mm. In order to stitch the tomograms without artifacts a sufficient overlap of e.g.  $\approx 20\%$  is recommended. This can be achieved by a displacement in x- and y- direction by 1 mm. A 3 times 3 scheme

yields a total reconstruction area of  $2.4 \text{ mm} \times 2.4 \text{ mm}$ , sketched in Fig. 3.11 b. The tomograms are stitched using the workflow presented in [Mie+19].

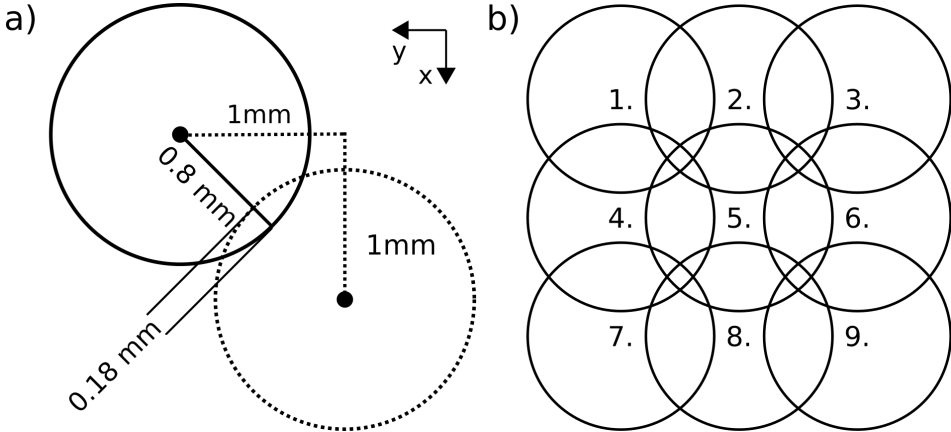


**Fig. 3.11:** Stitching acquisition scheme. a) Illustration of the dimensions of two reconstructed slices, shifted by 1 mm in x- and y- direction. The minimum overlapping distance is 0.18 mm. b) Stitching of 9 (3x3) tomograms results in a reconstruction area of  $2.4 \text{ mm} \times 2.4 \text{ mm}$ .

A comparison of a reconstructed slice obtained by the stitched X-ray tomograms and an *H&E* stained histological slice is shown in Fig. 3.12. The slices are not identical, but in close spatial proximity, since the histological slice was sectioned prior to the tomographic scan. In both images, the morphology of the tissue sample is clearly differentiable from the background and various tissue layers are distinguishable. A detailed discussion of the *H&E* staining and the resulting image contrast compared to the image contrast of the reconstructed X-ray slice is presented Sec. 3.4.1. Ring artifacts in the X-ray reconstruction are visible at the top of the image. These result from a flawed empty beam correction caused by scattering dirt on the entry/exit window of the KB box. Based on this acquisition scheme the tissue to air distances were analysed in 3D.

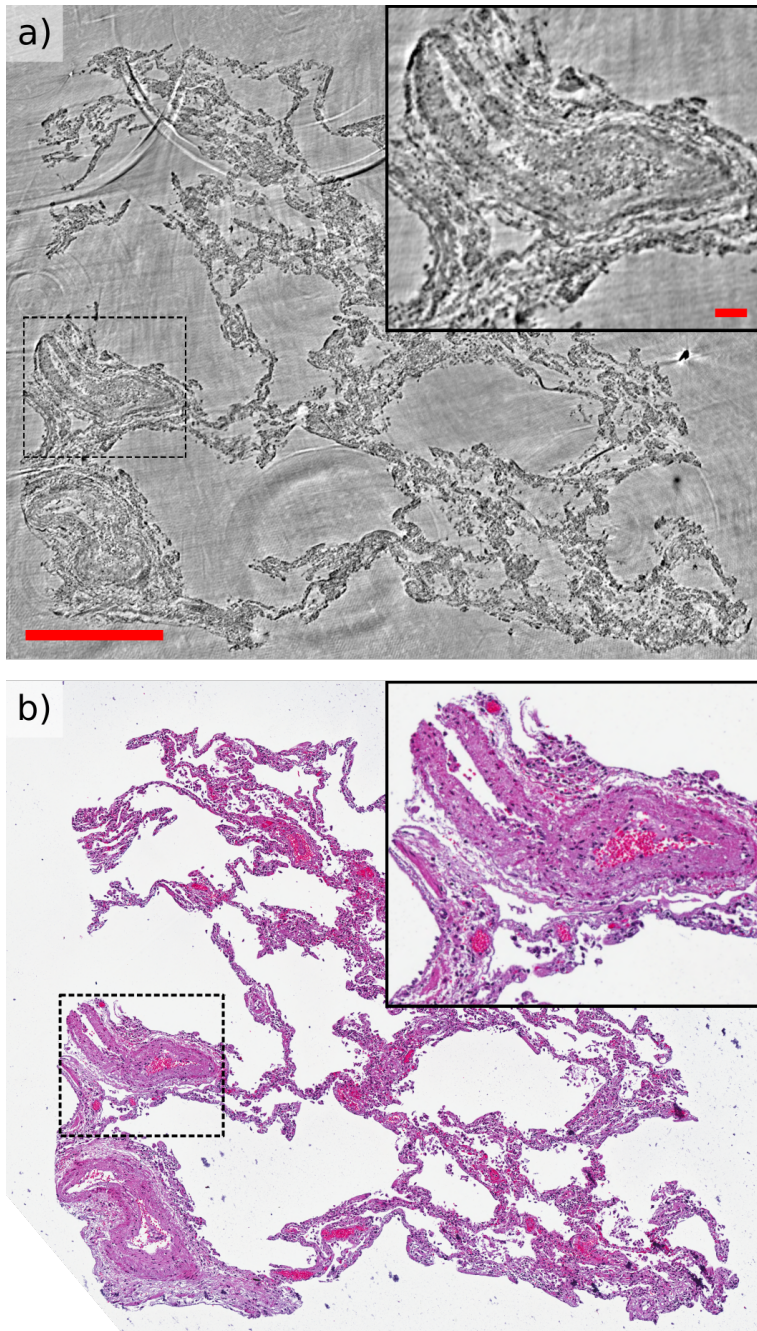


**Fig. 3.12:** (caption next page)

**Fig. 3.12 (previous page):** Comparison of a stitched unstained virtual histology slice and an *H&E* stained histology slice of covid-19 affected human lung tissue. They are in close spatial proximity, since the histological slice was sectioned prior to the tomographic scan. a) Reconstructed slice obtained by stitching 9 (3x3) individual tomograms. The ring artifacts at the top indicate two such individual reconstructions. The origin of the ring artifacts is a flawed empty beam correction due to scattering from dirt on the windows of the KB box. b) The corresponding *H&E* stained histological slice. Scale bars are 500  $\mu\text{m}$  and 50  $\mu\text{m}$  in the inset.

**Tissue-air distance** Severe progression of the 2019 coronavirus disease (Covid-19) is frequently accompanied by the clinical acute respiratory distress syndrome (ARDS) and respiratory failure, an organ manifestation responsible for the majority of Covid-19 fatalities. Lung injury associated with ARDS can be readily detected by radiographic chest imaging and clinical computed tomography (CT), which has assisted the diagnosis and management of Covid-19 patients [LNK20; Shi+20; Chu+20]. Here, so-called peripheral lung ground-glass opacities are the main radiological hallmark of ARDS, and can be linked to the histological observation of diffuse alveolar damage (DAD) with edema, hemorrhage, and intraalveolar fibrin deposition [Ack+20]. This disturbs the gas exchange by reducing the surface area between the alveolar septa and the inhaled air. With access to the 3D volume of specimens, 3D parameters characterizing the architecture with respect to the tissue air surface are determined. The workflow of the 3D analysis is illustrated in Fig. 3.13 exemplarily for one sample.

The 3D reconstructions were first binned (2x2x2) and the tissue was segmented from the surrounding paraffin using the segmentation software Ilastik [Ber+19a; Ber+19b], which was then further refined in MATLAB. In order to exclude single macrophages or detached tissue, only voxels connected to the tissue block were considered for the distance map. Further, the areas of the paraffin, which represent air compartments, were linked to the outside of the tissue block. Individual selfcontained areas of paraffin (not connected to air) were excluded from the mask. Based on this segmentation, the distance  $d_{O_2}$  to the nearest voxel containing oxygen was calculated for each tissue voxel. The tissue volume  $V$  is given by the sum of all voxels containing tissue. The surface area  $SA$  is defined by all tissue voxels with a distance of 1 px to the air. Additionally, the mean distance  $\bar{d}_{O_2}$  from all tissue voxels to the closest air compartment and its standard deviation was calculated. For the shown sample the **specific surface area**  $S_V$  is

$$S_V = SA/V = 0.1928.$$

Together with the edge length of a voxel  $d_{vx} = 1.3 \mu\text{m}$  a **characteristic length**  $L_C$  was calculated:

$$L_C = V/SA \cdot d_{vx} = 6.7 \mu\text{m}.$$

The distance  $d_{O_2}$  for each tissue voxel is illustrated for an exemplary slice in Fig. 3.13 c), the 3D histogram is shown in e) and the corresponding 3D volume in g). The mean tissue to air distance is  $\bar{d}_{O_2} = (3.6 \pm 2.1) \mu\text{m}$ . Poor oxygen exchange is related to lower specific surface area, larger characteristic length  $L_C$  or larger tissue to air distance  $\bar{d}_{O_2}$ .

### 3.4.1 Direct comparison of *H&E* stained microscope and unstained X-ray phase-contrast images

The differences of conventional histology (*H&E* staining) and virtual histology (X-ray phase-contrast unstained) images are discussed on the exact same slices of an exemplary object, as illustrated in Fig. 3.14. Since conventional histology requires an invasive sectioning of the object, beforehand an X-ray tomogram of unstained Covid-19 affected human lung tissue embedded in paraffin was acquired. Afterwards, an object slice was separated, stained with the the standard two component stain **Hematoxylin** and **Eosin** for histological examination of human tissue and imaged by an optical microscope.

Both stains exploit complementary contrast mechanisms. The hematoxylin stains acidic (basophilic) structures such as the nucleus, the rough endoplasmic reticulum and ribosomes in purplish blue. Eosin acts as a counter stain and stains basic (acidophilic) structures such as most of the cellular organelles and the extracellular matrix in red or pinkish [Cha14]. Thus, the image obtained by *H&E* stained histology represents the basophil/acidophil affinity of the tissue in the image contrast. As opposed to this, the gray values of the X-ray image encode the electron density of the tissue. To this end, conventional and virtual histology represent different tissue properties.

The same acidophil affinity of two tissue structures does not imply the same electron



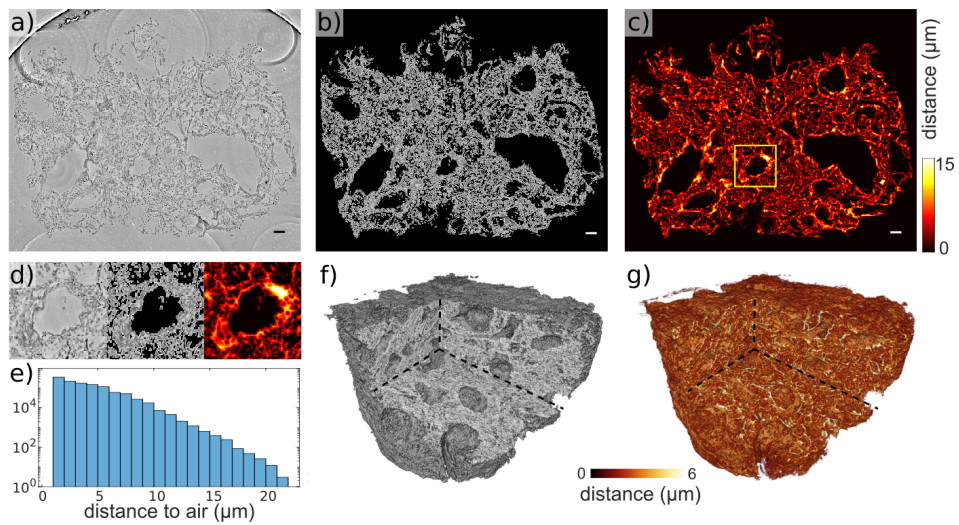


**Fig. 3.13:** 3D analysis of unstained paraffin embedded Covid-19 affected human lung tissue. a) Virtual histology slice obtained by stitching 9 (3x3) individual tomograms. b) Tissue voxels were separated from air-containing voxels by first segmentation of the tissue followed by masking out the air. c) Distance between the tissue voxels and the closest air-containing voxels  $d_{O_2}$  is encoded by the color in the tissue mask. d) Magnified area of a vessel as marked in (c), with the respective colormaps similar to (a) - (c). e) Histogram of the tissue to air distance  $d_{O_2}$  distribution. f) 3D rendering of the masked tissue volume. g) 3D rendering of the tissue to air distance volume. Scale bars: 100  $\mu\text{m}$

density of the structures, as illustrated on the example of comparing erythrocytes (Fig. 3.14 c)) with a thrombus (Fig. 3.14 d)). In the *H&E* image, the pinkish cells in the red rectangle are erythrocytes while the homogeneous pinkish ellipse in the blue rectangle is a thrombus. The image contrast in the form of the pink colored intensity is the same. However, the electron density of both structures differs as visible in the X-ray image and furthermore, the thrombus reveals even substructures as shown in Fig. 3.14 d).

An advantage of the *H&E* staining is the combination of two counteracting stains. Tissue structures without contrast in the hematoxylin stain are obtaining high contrast in the eosin stain. In addition, both stains are separated in different colors (pink/blue), acting as two separated signal channels. The X-ray image of the unstained tissue contains only one signal channel for the electron density.

Since different tissue properties are visualized by *H&E* histology and virtual histology, a combination of both image modalities leads to an improved representation of the tissue. In addition, to generate an X-ray image contrast based on the same tissue properties as in conventional *H&E* stained histology, X-ray sensitive *H&E* stains are required as well as the opportunity to differentiate signal channels. Recently, first modified variants of hematoxylin and eosin are developed that are sensitive to X-rays while maintaining the staining function for conventional histology. In [Mül+18] a hematein lead complex was developed to increase to the electron density of basophilic structures. After the acquisition of the X-ray image the tissue was counterstained for the conventional histology image. Similarly, the electron density of the eosin molecule was increased by the addition of four bromine atoms [Bus+18]. So far, both X-ray modified stains have been used on their own. A combination of both stains could lead to an *H&E* stained X-ray image, if separate signal channels are available. Such X-ray signal channels are realised by considering the X-ray energy, leading to the idea of **spectral tomography**. This could be achieved either by energy sensitive detectors [Loh+20b] or by modifications of the X-ray illumination spectrum, e.g. with the method of K-edge-substraction [Kul+19].

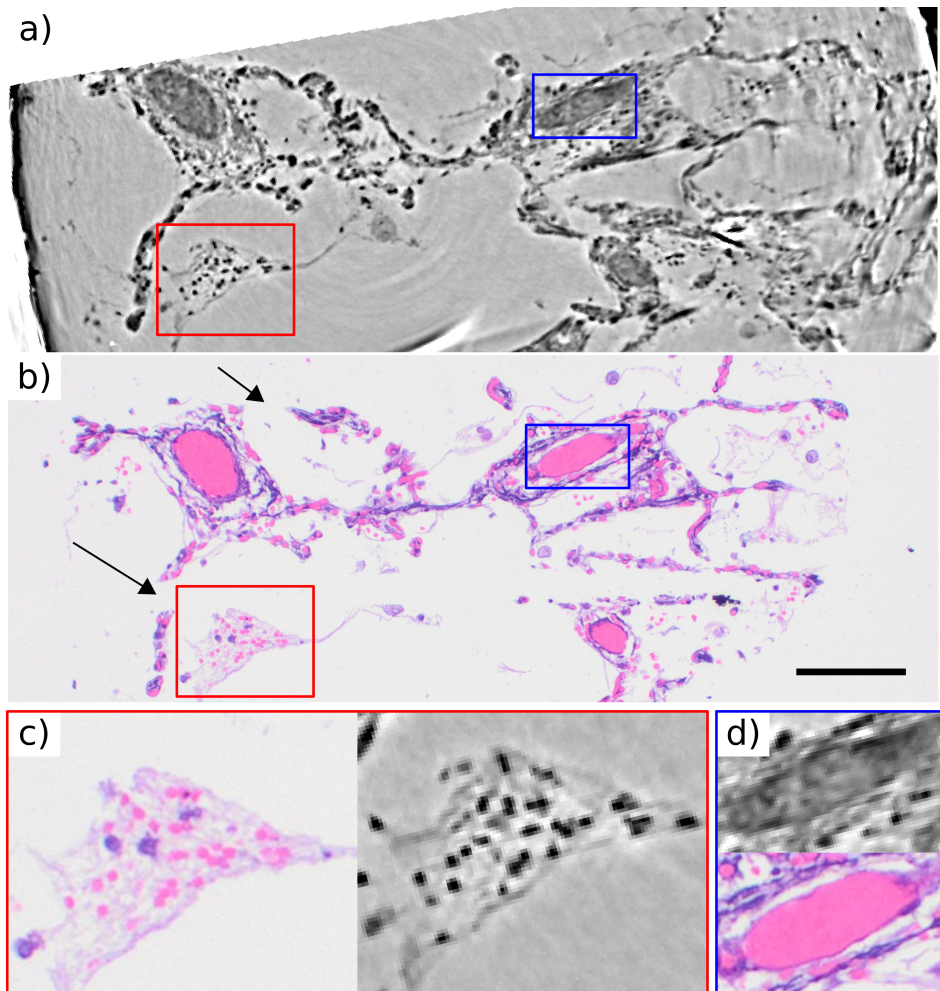


**Fig. 3.14:** Direct comparison of 3D virtual histology and conventional *H&E* stained histology. An X-ray tomogram of unstained Covid-19 affected human lung tissue embedded in paraffin was acquired. Afterwards, a slice of the sample was sectioned and stained with **H**ematoxylin and **E**osin. a) Virtual histology slice obtained by X-ray phase-contrast tomography encodes the electron density of the sample. Erythrocytes are marked by the red rectangle, while a thrombus is marked by the blue rectangle. b) The corresponding slice obtained by conventional *H&E* stained histology. Compared to the X-ray slice, ruptures and distortions are visible due to the additional preparation steps, as marked by the two arrows. c) The comparison of the erythrocytes shows an intense pinkish color contrast in the *H&E* image and strong contrast in the X-ray image. d) The comparison of a thrombus shows a similar intense pinkish color contrast in the *H&E* image as the erythrocytes. However, the X-ray image contrast is lower. Furthermore, the thrombus reveals substructures within the X-ray image. Scale bar: 50  $\mu\text{m}$ .

## 3.5 ID19 - Ischemic stroke in mouse brain tissue

Ischemia is a decrease in blood supply of tissue, causing a shortage of oxygen. Cerebral ischemia is associated with a lack of oxygen within brain tissue, leading to irreversible cell injury. Visualization and quantification of the structural alterations in 3D caused by cerebral ischemia, on multiple length scales from single cell up to the entire brain region provides further insights into stroke mechanisms. This 3D information can be obtained by phase-contrast tomography. In the inhouse study "Multiscale x-ray phase-contrast tomography in a mouse model of transient focal cerebral ischemia" [Töp+19] 1 mm punch biopsies of the left and right hemisphere of one mouse brain with an induced cerebral ischemia in the left hemisphere were investigated via phase-contrast tomography. Single cells without further differentiation were observed as well as the migration of new cells into the affected brain region. A first suggestion is that the additional cells result from the inflammatory response. Based on this work, a follow-up experiment on cerebral ischemia in mouse models with higher contrast and resolution was planned and performed in the framework of this thesis.. It was conducted at the propagation-based X-ray phase-contrast microtomography setup at the beamline ID19 at the ESRF. In addition to the study of structural alterations and possible inflammatory response, the neuroprotective effect of lithium on ischemic stroke was investigated. For statistic purposes, 8 brains were measured (4 lithium treated + 4 untreated ischemic brains) in total. This section concentrates on the multi-scale approach and image quality of the ID19 compared to the parallel beam setup of the *GINIX*.

### 3.5.1 Sample preparation

Cerebral ischemia was induced in the left brain hemisphere of C57BL6 mice (common inbred strain of laboratory mice) by 45 min exposure of intraluminal middle cerebral artery occlusion (MCAO) followed by 24 h of reperfusion [Doe+14]. The experiments were performed according to the regulations imposed by local authorities (LAVES, Lower Saxony, Germany) following the ARRIVE guidelines. The animals were intraperitoneally treated with phosphate buffered saline (PBS; control group) or lithium chloride (Sigma-Aldrich, Germany) dissolved in PBS. PBS or lithium were given at the beginning of the reperfusion, and at 6 h after the MCAO. The lithium dosage for the first injection was  $1 \text{ mmol kg}^{-1}$  and for the second  $2 \text{ mmol kg}^{-1}$ . The unstained mouse brains were embedded in paraffin. To reduce excess paraffin 8 mm biopsy punches are

taken, which cover most parts of the brain as can be seen later.

### 3.5.2 Parallel beam multi-scale tomography at ID19

The ID19 beamline at the ESRF [Wei+10], which was recently upgraded to a fourth generation synchrotron [Pac19], offers propagation-based X-ray phase-contrast microtomography without any focusing optics. X-rays with an energy of 26.1 keV are generated by an U13 undulator with  $\frac{\Delta\lambda}{\lambda} \approx 0.01$ . A multi-scale approach is realized in this experiment by using two different detectors as sketched in Fig. 3.15 a). In the **overview configuration** a pco.edge 5.5 is placed at 1900 mm propagation distance. The Fresnel number is  $F = 0.0293$ . It is coupled with a 250  $\mu\text{m}$  thick LuAG:Ce (Cerium-doped Lutetium Aluminium Garnet) scintillator and a 4x microscope objective resulting in an effective pixel size of 1.625  $\mu\text{m}$ . The flat field image acquired with an exposure time of 50 ms shows an intensity decay towards the image borders as depicted in Fig. 3.15 b). In the **detail configuration** a pco.edge 4.2 is placed at 300-610 mm propagation distance. The Fresnel number is  $F = 0.0146$ . It is coupled with a 10  $\mu\text{m}$  thick GGG:Eu ( $Gd_3Ga_5O_{12} : Eu$ ) scintillator and a 10x microscope objective resulting in an effective pixel size of 0.65  $\mu\text{m}$ . The flat field image acquired with an exposure time of 100 ms is quite homogeneous. However, it contains a lot of scattering particles as depicted in Fig. 3.15 c). Despite the scatterers, the empty-beam correction works well.

**Overview configuration** First, the entire brains are scanned in the overview configuration at 1.625  $\mu\text{m}$  pixel size. To this end, 5 tomograms are acquired in total as illustrated in Fig. 3.16 top left. Four of the tomograms are taken at neighboring overlapping positions arranged in a grid. This is completed by one additional tomogram in the center of the grid. Stitching these data sets leads to a reconstruction volume covering the entire brain. Each tomogram consists of 4000 projections acquired with an exposure time of 100 ms over 360°. The phase reconstruction was performed via the CTF phase retrieval for each empty-beam corrected projection. The reconstruction parameters are  $\text{lim1} = 8.8\text{e-}6$ ,  $\text{lim2} = 0.288$  and  $\frac{\beta}{\delta} = 1/1977$  ('Tissue, Soft (ICRP)' value from [Sch+11]). Tomographic reconstruction is performed via filtered backprojection, followed by manual stitching. An exemplary slice of the reconstructed brain is shown in Fig. 3.16. Due to the high image contrast, the different brain layers are distinguishable, e.g. the cerebellum is recognisable at the bottom of the slice. Comparisons of entire brain layers between the left and right hemisphere are accessible with a voxel

size of  $1.625 \mu\text{m}$ . For instance, the electron density progression and its difference between the hemispheres can be determined on the whole organ.

**Detail configuration** In order to resolve single cells, tomograms are taken in the detail configuration at  $0.65 \mu\text{m}$  pixel size. Here, 8 neighboring overlapping tomograms are acquired in a  $2 \times 2 \times 2$  3D grid as depicted in Fig. 3.16 bottom left. The scan area is the center of the brain, marked by the red squares in the reconstruction of the overview scan. Each tomogram consists of 3000 projections acquired with an exposure time of 50 ms over  $360^\circ$ . The phase reconstruction was performed via the CTF phase retrieval for each empty-beam corrected projection. The reconstruction parameters are  $\text{lim1} = 1.9200\text{e-}07$ ,  $\text{lim2} = 0.4$  and  $\frac{\beta}{\delta} = 1/3008$  ('Paraffin Wax' value from [Sch+11]). An exemplary slice of the reconstructed volume is depicted in Fig. 3.17 a).

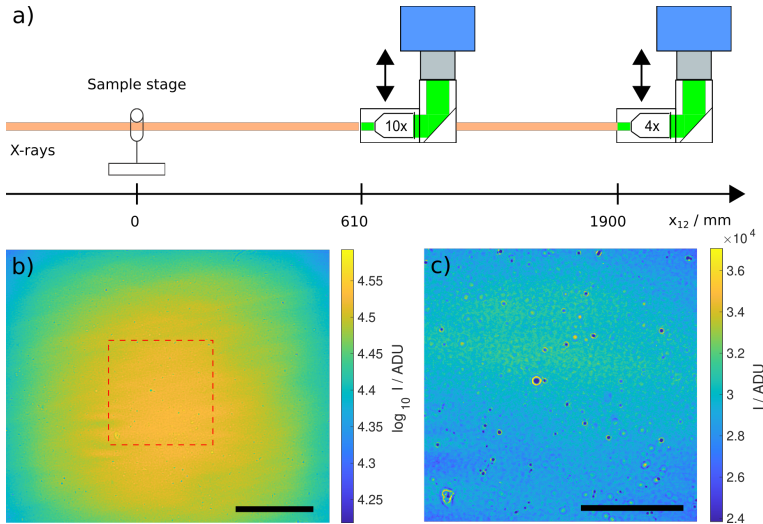


**Fig. 3.15:** Experimental setup at the ID19 beamline (ESRF). a) A multi-scale acquisition scheme is realized by utilising two detectors with different pixel sizes. The overview scan is performed with  $1.625 \mu\text{m}$  pixel size (FOV:  $4.2 \text{ mm} \times 3.5 \text{ mm}$ ) at 1900 mm propagation distance, while the detail scan is performed with  $0.65 \mu\text{m}$  pixel size (FOV:  $1.3 \text{ mm} \times 1.3 \text{ mm}$ ) at 300-610 mm propagation distance. b) The flat field image of the overview configuration shows the beam profile with an intensity decay towards the edges. The red square indicates the field of view of the second detector. c) The flat field image of the detail configuration reveals a lot of scattering particle within the beam profile. Scale bars: b) 1 mm and c) 0.5 mm.

A comparison of the same reconstructed slice demonstrates the improvement in resolution by switching from the overview configuration to the detail configuration, as

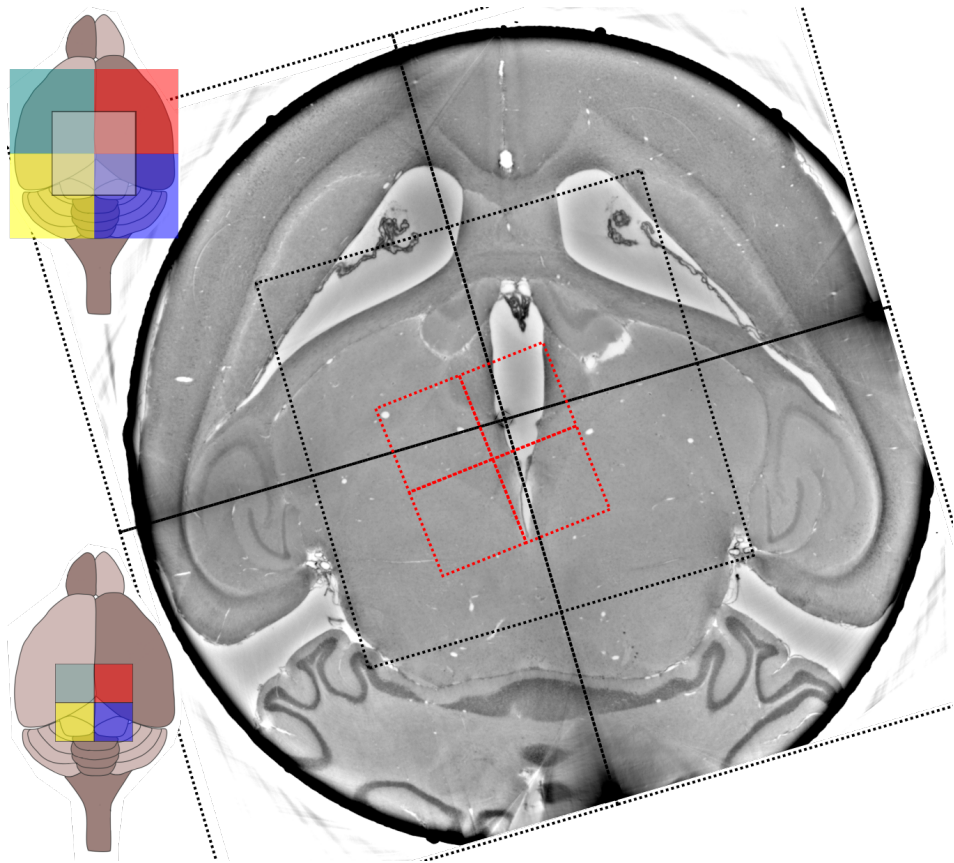


**Fig. 3.16:** Overview of the reconstruction volumes of the ID19 experiments. 5 tomograms are acquired to scan a 8 mm punch biopsy of unstained paraffin embedded mouse brain, indicated by the black dotted squares in the reconstructed slice and as illustrated in the sketch on the top left. The detail tomograms consist of 2x2 tomograms in the central region of the brain, marked by the red squares. The corresponding sketch is at the bottom left.

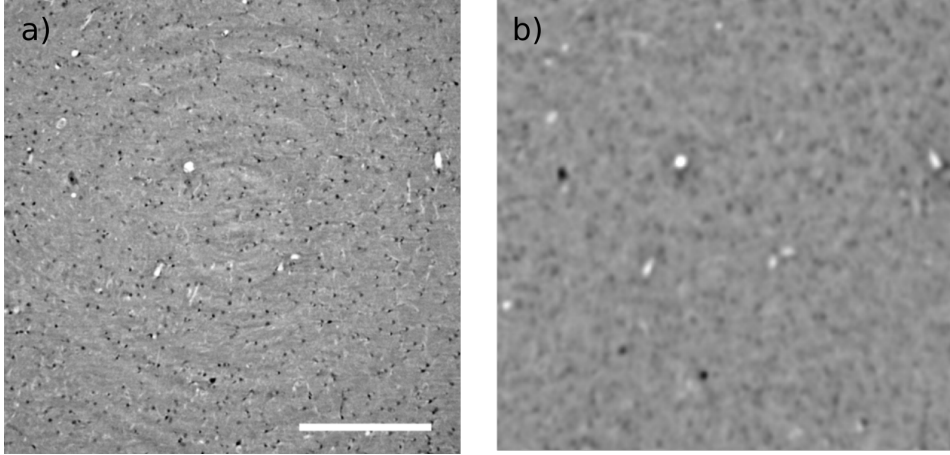


**Fig. 3.17:** Comparison of reconstructed slices obtained by the overview and the detail configurations at ID19 of unstained paraffin embedded mouse brain tissue. Left: Exemplary slice of the detail scan demonstrates, that the resolution is sufficient to resolve single cells. Right: Same slice of the overview configuration with a resolution insufficient to resolve all cells. Scale bar: a) 250  $\mu\text{m}$ .

illustrated in Fig. 3.17. While the resolution of the overview configuration is on the edge of resolving the cells, the detail configuration clearly resolves them. To this end, the multi-scale acquisition scheme enables the 3D analysis of the cells within a subvolume, e.g. their distribution in 3D, while knowing the exact position of the subvolume within the brain.

### 3.5.3 Comparison of the ID19 detail setup and the GINIX parallel beam setup

The pixel size of the **detail configuration** of the ID19 setup is the same as for the **PB setup** at the GINIX. For a comparison, tomograms of a 1 mm punch biopsy of the unstained paraffin mouse brain tissue were acquired at both setups. The contrast formation of both measurements differs in the propagation distance  $x_{12}$ , the X-ray energy  $E$  and the monochromaticity  $\Delta E$ . Nevertheless, the Fresnel numbers are comparable. All experimental parameters are listed in Tab. 3.2. The phase retrieval for both reconstructions is performed via the CTF-approach. An exemplary slice of the tomographic reconstruction obtained by the parallel beam setup of the *GINIX* is shown in Fig. 3.18, while the same slice obtained by the detail configuration of the



**Table 3.2:** Experimental parameters of the overview configuration at ID19, the detail configuration at ID19 and the parallel beam configuration at GINIX.

	overview ID19	detail ID19	PB GINIX
Pixel size $p$	1.625 nm	650 nm	650 nm
Propagation distance $x_{12}$	1900 mm	610 mm	220 mm
Energy $E$	26.1 keV	26.1 keV	13.8 keV
Fresnel number $F$	0.0293	0.0146	0.0214
Monochromator	-	-	channel-cut
Angle increment	0.09°	0.1200°	0.1200°
CTF phase retrieval			
lim1	8.81e-06	1.92e-07	2.24e-06
lim2	0.29	0.4	0.2
$\frac{\delta}{\beta}$	1977	3008	1942

ID19 is shown in Fig. 3.19. This qualitative comparison of these two reconstructions illustrates that the image quality is similar. Both reconstructions resolve single cells within the different cell layer of the mouse brain, as magnified in the inset of the marked areas. However, slight differences in the contrast of the low spatial frequencies are visible. They result as a combination of different CTF regularisation parameters lim1, different setting of the color map range and the different contrast transfer, during the image formation, and subsequent reconstruction.

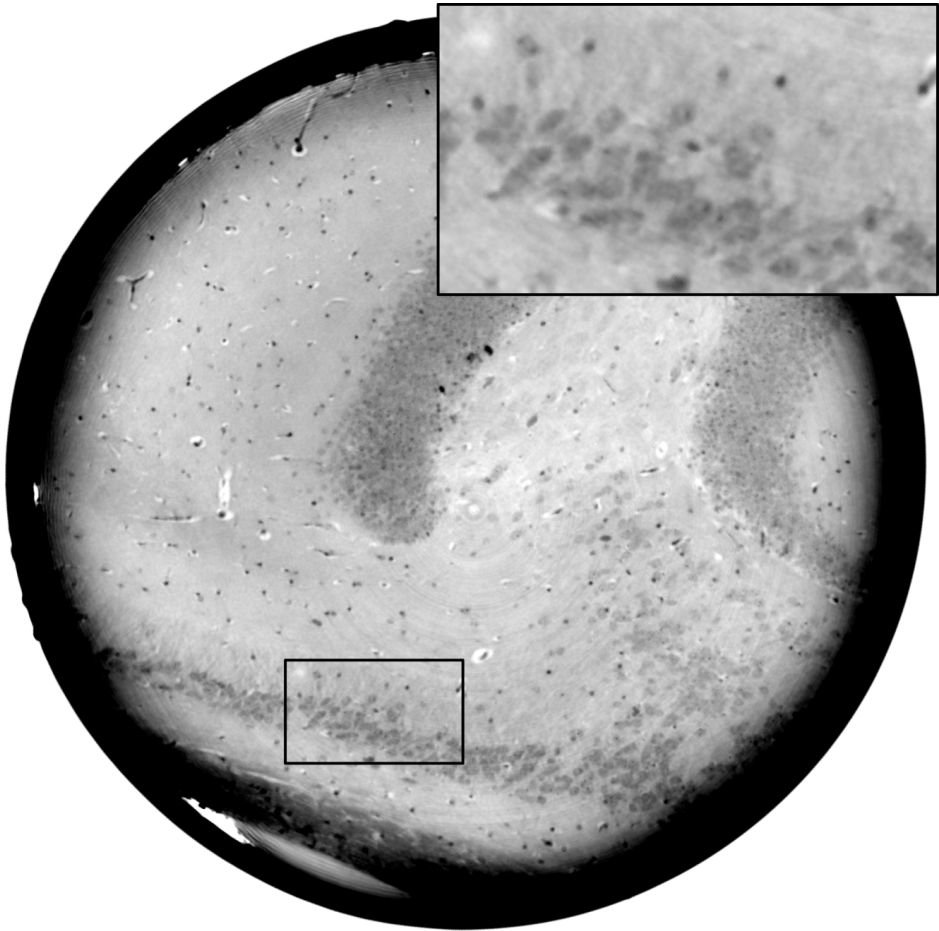


**Fig. 3.18:** Reconstructed xy-slice of a 1 mm punch biopsy of unstained paraffin embedded mouse brain tissue obtained by the parallel beam setup at the GINIX. The Fresnel number is  $F = 0.0214$  with a propagation distance of  $x_{12} = 220$  mm and an X-ray energy of 13.8 keV. CTF reconstruction parameters are  $lim1 = 2.24e - 06$ ,  $lim2 = 0.2$  and  $\frac{\delta}{\beta} = 1942$ . The inset shows magnification of the marked area. Cells within the brain layer are clearly resolved.

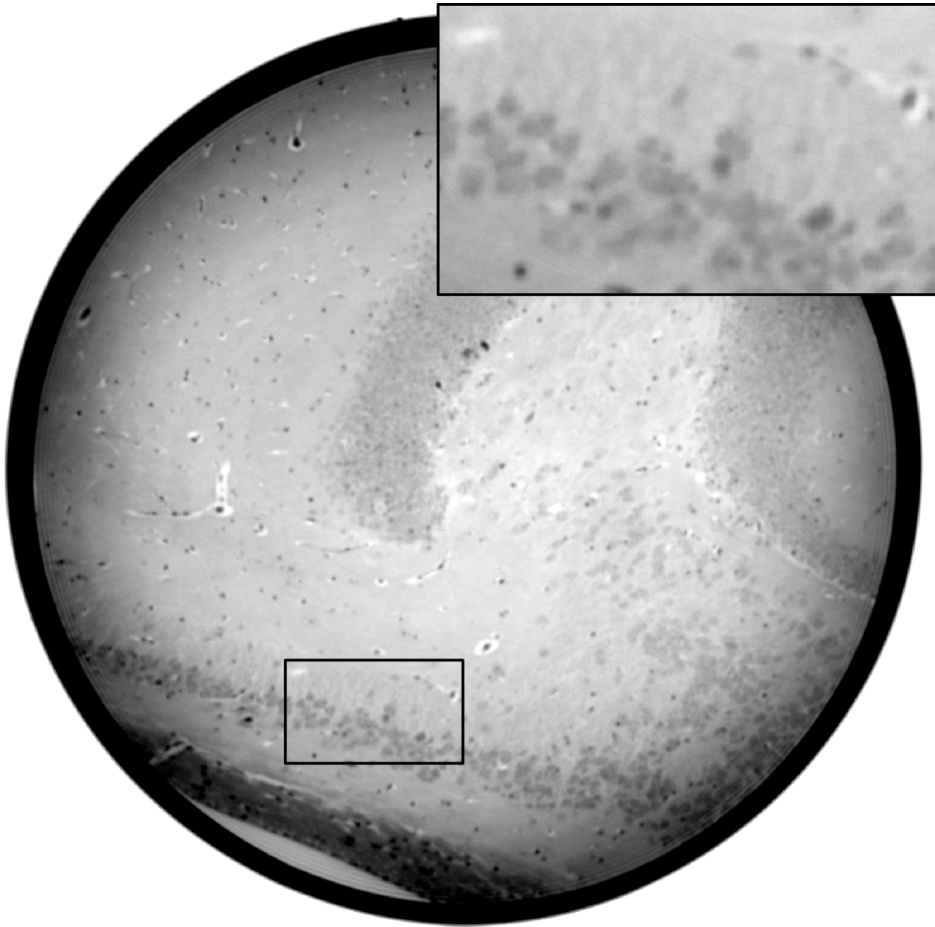


**Fig. 3.19:** Reconstructed xy-slice of a 1 mm punch biopsy of unstained paraffin embedded mouse brain tissue obtained by the detail configuration at the ID19. The Fresnel number is  $F = 0.0146$  with a propagation distance of  $x_{12} = 610$  mm and an X-ray energy of 26.1 keV. CTF reconstruction parameters are  $lim1 = 1.92e - 07$ ,  $lim2 = 0.4$  and  $\frac{\delta}{\beta} = 3008$ . The inset shows magnification of the marked area. Cells within the brain layer are clearly resolved.

## 3.6 Discussion

The **parallel beam setup** is a major complement to the high resolution **waveguide-based holotomography setup** at the *GINIX* endstation. It is now possible, to scan the samples on a  $\sim 4$  times larger scale compared to the high resolution scans. This has the advantage of obtaining an overview of the sample structure as well as inspecting the sample quality, e.g. in terms of the sample preparation, prior to the high resolution scan. Based on the overview reconstruction, areas of specific interest can be identified and navigated to. The detection of these areas based on the holographic projection of the high resolution setup alone is very difficult. Importantly, the parallel beam setup alone is a powerful configuration to image biomedical tissue at the scale of a few mm at cellular resolution. For most of the biomedical tissue applications, the provided single cell resolution with an effective pixel size of  $0.65 \mu\text{m}$  is sufficient to characterize the tissues. Compared to the high resolution scans the characterization and 3D quantification of larger volumes is statistically even more meaningful. Studies on the 3D structures of large sample quantities are conceivable, since the acquisition time of one tomogram is less than 5 min in total. For samples that are larger than the detector's field of view of  $1.6 \text{ mm} \times 1.4 \text{ mm}$ , the reconstruction volume can be artificially enlarged by stitching adjacent tomograms. Punch biopsy samples with sizes up to 3 mm in diameter were scanned without showing strong shape artifacts of *local tomography*. Nevertheless, the volumetric flow rate is still limited by the X-ray beam size, which cannot be further increased due to the beamline design.

So far, the PB setup was successfully implemented and contributed to some publications, e.g. [Rei+20; Eck+21a; Rei+21; Kep+21; Eck+21c], besides the presented first author publications [Fro+20a; Eck+20]. Furthermore, the a qualitative comparison of the PB setup and the microtomography setup at the ID19 revealed similar image details.

However, the reconstruction quality of the object can be further improved by investigating the phase of the illumination function in the reconstruction plane. Furthermore, gray value and shape artifacts resulting from local tomography should be investigated in more detail. This is important for reconstructing quantitative electron densities. The application of correction schemes for local tomography artifacts such as [RFS20] should be considered and optimized. Thus, the reconstruction volume can be further extended by stitching more tomograms without artifacts. Moreover, the combination of scintillation material, scintillator thickness, absorption foils and illumination time can be further optimized. With a thinner scintillator, which is less sensitive, the amount of absorption foils can be reduced, leading to less scatterers in the X-ray beam. A huge

---

opportunity to improve the image quality of the reconstructions is provided the investigation of energy variations within experiments. Instead of changing the propagation distance, a change of the X-ray energy leads to different Fresnel numbers and therefore contrast formations, as demonstrated in [Rob+20]. Furthermore, the improvement of the image contrast by X-ray specific stains can be investigated. E.g. a combination of multiple structure specific stainings within one sample has the potential for spectral X-ray tomography by changing the monochromatic X-ray energy.



# Multi-scale approach (Scale II): Waveguide-based holotomography

---

# 4

## 4.1 Motivation

The **waveguide-based holotomography setup (WG setup)** of the *GINIX* endstation is a high resolution propagation-based phase-contrast X-ray tomography setup with an divergent illumination created by an X-ray waveguide. It was established, refined and optimized over the last 10 years [Kal12; Kre15; Sal+15; Töp18], consecutively. A good compromise between field of view (FOV) and resolution for this setup is found to be at a 40x geometrical magnification ( $x_{01} = 125 \text{ mm}$ ,  $x_{02} = 5000 \text{ mm}$ ).

In this default configuration the FOV is  $400 \mu\text{m} \times 350 \mu\text{m}$  with an effective pixel size of 160 nm, which is particularly suitable to study biological tissues with sub-cellular resolution as in [Töp+18; Eck+20; Rei+21; Eck+21b].

In the demand for higher resolution the geometrical magnification can be increased by decreasing the source to sample distance  $x_{01}$  resulting in smaller effective pixel sizes. For example, in [Ves+21] tomograms were acquired with a voxel size of 64 nm, however, even smaller pixel sizes are realisable. The unique application of an X-ray waveguide to create a secondary X-ray focus offers the advantages of a small focal spot size (sub-100 nm), an increase in spatial coherence and a lowpass filtering of the illumination profile at the cost of reduced beam intensity. A comparable propagation-based phase-contrast X-ray tomography setup excluding the waveguide illumination at similar resolutions is available e.g. at the nano-imaging beamline ID16A at the ESRF [Kua+20].

This chapter presents the current state of the *WG setup* at the *GINIX* and highlights the software and hardware upgrades implemented during this thesis. The performance of two improved X-ray waveguide designs is discussed in terms of beam stability and intensity. Furthermore, the properties of the new fiber-optic scintillation-based sCMOS detector for the *WG setup* are described in detail. Software-wise, the application of a pixel sensitivity map for the new detector is demonstrated.

## 4.2 Holotomography setup at the GINIX

The *WG setup* of the *GINIX* endstation combines the lenseless imaging technique of propagation-based X-ray phase-contrast in the holographic regime with a tomographic acquisition scheme. This enables the 3D reconstruction of the phase shifts, introduced by the object. The outstanding feature in this setup is an X-ray waveguide. It acts as a secondary X-ray source with a focal spot size down to sub-50 nm [Krü+10; Krü+12] and increases the spatial coherence of the X-ray beam required for propagation-based phase-contrast. Behind the waveguide, the X-ray beam propagates in a diverging geometry. The resulting cone beam introduces a geometrical magnification  $M = \frac{x_{01} + x_{12}}{x_{01}}$  of the object at the detector plane, which is determined by the distance between waveguide exit and object  $x_{01}$  and the distance between object and detector  $x_{12}$ . Typical magnifications of 40x up to 100x lead to high 3D resolutions with effective pixel sizes of 50-200 nm [Ves+21]. Since a detailed technical description is presented in [Sal+15], only the main components for the image acquisition are introduced.

**Undulator** The X-rays are generated by an undulator insertion device. In 2020, the 5 m long U29 undulator (29 mm magnetic period) was replaced by a 5 m long U32 undulator. This offers tunable X-ray energies without an energy gap between the 1st and the 3rd undulator harmonic in the medium-hard X-ray regime of 5-20 keV.

**Monochromator** The X-ray beam is monochromated by either a Si(111) channel-cut (CC) or a Si(111) double-crystal monochromator (DCM) to improve the temporal coherence. The CC provides a much higher angular stability, while the DCM can operate in a larger energy range offering an energy independent beam position offset and a slightly higher flux.

Importantly, the pitch angle of the DCM is controlled and automatically regulated to ensure a stable beam position. It is a counter measure to motor drifts as well as to vibrations of the crystals introduced by the liquid nitrogen cooling. This automatic regulation sometimes over corrects. As a consequence, the resulting changes of the X-ray beam position cause a failure of the X-ray coupling into the waveguide. To this end, it is recommended to turn off automatic pitch control for the WG setup. In that way, a more steady waveguide illumination with a slow drift is ensured compared to the abrupt loss of the entire X-ray intensity due to a failed waveguide coupling.



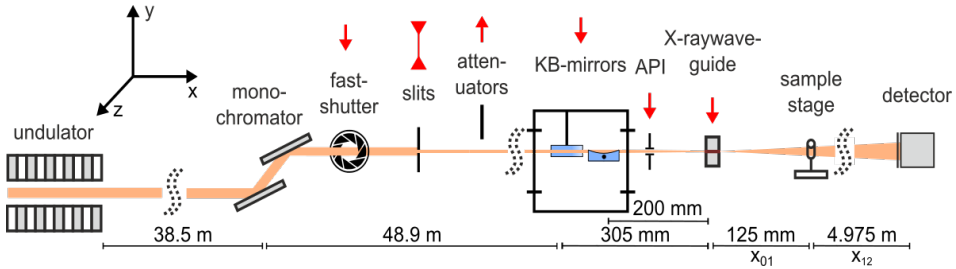


**Fig. 4.1:** Sketch of the waveguide-based holotomography setup at the *GINIX* endstation. The X-rays are generated with an energy of 5-20 keV by an 5 m long U32 undulator. The temporal coherence is improved by either a Si(111) channel-cut (CC) or a Si(111) double-crystal monochromator (DCM). Behind the fastshutter, several slit systems and the attenuator foils box are placed. The X-ray beam is focused by a pair of KB-mirrors down to focal spot size of about 300 nm x 300 nm. An X-ray waveguide is placed at the focal plane of the KB-mirrors to further reduce the focal spot size. The object is mounted onto the sample stage with an adjustable distance to the waveguide. A typical distance is 125 mm. The position of the detector is fixed at a distance of 5100 mm to the focal plane of the KB-mirrors. This figure is adopted from [Fro+20a].

**KB mirrors** A pair of elliptical shaped mirrors, the Kirkpatrick-Baez (KB) mirrors, focuses the beam down to about 300 nm x 300 nm. The first mirror focuses in vertical direction with focal length  $f_v = 302$  mm and an incidence angle of  $\Theta_v = 3.954$  mrad. The second mirror focuses in horizontal direction with focal length  $f_h = 200$  mm and an incidence angle of  $\Theta_h = 4.05$  mrad [Kal12; Sal+15]. Apart from the double-reflected beam, two single reflected beams as well as a non reflected part of the incident X-ray beam are present. A 1 mm aperture of tungsten (APY) blocks these non- and single-reflected beams.

**X-ray waveguides** An X-ray waveguide is placed in the focal plane of the KB-mirrors to further reduce the focal spot size. The spot size depends on the diameter of the guiding layer. A reduction of the diameter size results in a smaller focal spot size and a higher beam divergence at the cost of a reduced photon flux. For example, a diameter of 100 nm leads to a fully illuminated scintillation detector, e.g. the Zyla (see Ch. 4.4) at 5 m distance with exposure times of a few seconds. The waveguide also serves as a lowpass filter for the high frequent features of the beam caused by imperfections of the mirror surfaces. The resulting smooth illumination is beneficial for the empty beam correction. Furthermore, the spatial coherence of the beam is increased [OS11]. The waveguide is precisely aligned by the *SmarPod* hexapod system (SmarAct, Germany),

which offers 6 degrees of freedom (3x translations + 3x rotations). The waveguides used in this thesis and their recent developments are presented in detail in Ch. 4.3.

**Sample stage** The sample stage consists of the three translational positioners (2x HPS-170 (x,y) and 1x UPL-160 (z), Micos, Germany) for the alignment of the tomographic rotation axis (UPR-160 AIR, Micos, Germany) mounted on top of them. For the alignment of the pitch and roll angle of the tomographic axis two custom build cradles are positioned below the motor. In order to adjust the position of the object itself, three additional translational stages (2x SLS-1760 (x,y) and SHL-1D20N-10 (z), SmarAct, Germany) are mounted on top of the rotational stage.

### 4.3 Recent developments of X-ray waveguides

X-ray optics are either based on refraction such as compound refractive lenses and zone plates or on reflection e.g. Kirkpatrick–Baez mirrors and X-ray waveguides. Since the index of refraction of vacuum (or air) is always larger than the index of refraction of a solid state material  $n_{air} > n_{mat}$  for X-rays, total reflection appears at the transition from air to matter. This effect can be exploited to fabricate X-ray waveguides. An empty channel (air filled) with a diameter of 10-100 nm within a solid state material acts as the guiding layer for the X-rays, while the surrounding material acts as the cladding material of the waveguide. Besides enabling the total reflection, the cladding layer has the function of absorbing the X-rays that are not guided by the empty channel. The waveguide length to fully absorb the incoming X-rays depends on the cladding material and the X-ray energy. Such an X-ray waveguide is manufactured by electron beam lithography, reactive ion etching and wafer bonding, as described in detail in [Hof+16; Töp18]. Different shapes of the guiding channel are realisable e.g. straight, tapered or curved, however in this work only straight channels are considered.

In the past, such straight empty channel X-ray waveguides based on a silicon cladding were successfully used with an X-ray energy of 8 keV [Sal+15; Hof17; Töp+18]. Since then, the improvement of the waveguides can be split in two directions. The change of the cladding material from silicon to germanium offers the opportunity to utilize higher X-ray energies with moderate aspect ratios between channel diameter and waveguide length. The first successful applications of these germanium waveguides in tomographic experiments at the *GINIX* are reported in [Fro+20a]. Furthermore, the manufacturing accuracy of the channels within a silicon cladding was improved

by outsourcing the e-beam lithography and reactive ion etching steps to the external company *Eulitha*. The performance of both waveguide types is presented and discussed.

### 4.3.1 Germanium waveguides

With an atomic number of  $Z = 32$  the electron density of germanium is higher than the electron density of silicon with  $Z = 14$ , resulting in a higher absorption coefficient. To this end, the required aspect ratio can be reduced. Additionally, the absorption edge of germanium is at 11.1 keV, which increases the X-ray absorption in the cladding material.

The diverging X-ray beam obtained by a germanium X-ray waveguide with  $200\ \mu\text{m}$  optical depth and a channel diameter of 100 nm at 5 m distance is presented in Fig. 4.2. The waveguide is placed into the X-ray focus of the KB-mirrors leading to a front coupling of the X-rays into the waveguide. The high photon flux resulted in the saturation of the Zyla detector ( $15\ \mu\text{m}$  Gadox scintillator) at an exposure time of 350 ms. The corresponding image is illustrated in Fig. 4.2 a). Typical exposure times for the same detector are 1-2 s for similar silicon waveguides at 8 keV X-ray energy. At these short exposure times the implementation of a continuous rotation for tomographic scans becomes reasonable and a reduction in scan time by a factor of 3-5 is realistic. In order to investigate the temporal stability of the beam intensity, the empty images obtained by two subsequent four distance tomographic scans are exploited. The measurement is completed by waveguide alignment scans and pure empty beam acquisitions afterwards. For a better understanding of the results shown in Fig. 4.2c), the acquisition steps for a tomogram at a single distance are described below:

- i) The waveguide is scanned in vertical and horizontal direction and moved to the position with maximum intensity (indicated as *WG alignment* and the white area)
- ii) 50 images of the X-ray beam are acquired (indicated as *Empty image* and the green area)
- iii) A tomogram with 1500 projections is acquired (indicated as *Tomographic scan* and the bronze area)
- iv) 50 images of the X-ray beam are acquired (indicated as *Empty image* and the green area)

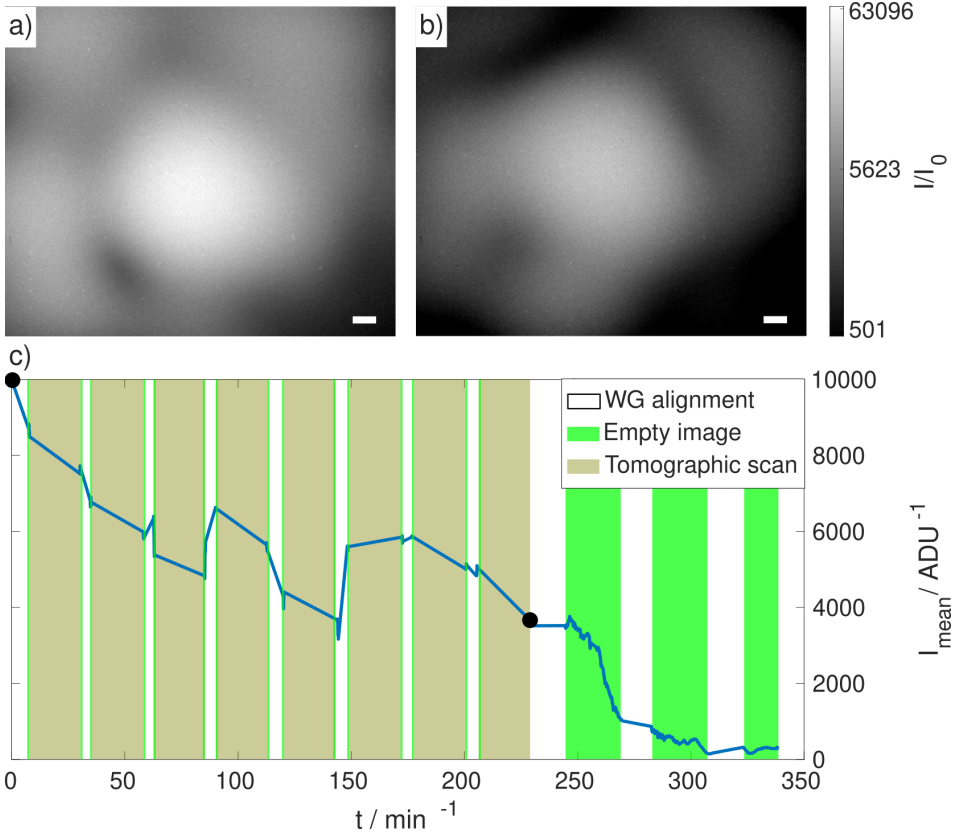


**Fig. 4.2:** Instability of a germanium X-ray waveguide with  $200 \mu\text{m}$  optical depth and a channel diameter of  $100 \text{ nm}$  at  $13.8 \text{ keV}$ , which is above the absorption edge of germanium ( $E_{\text{edge}} = 11.1 \text{ keV}$ ). a) The first intensity image of the X-ray beam ( $t = 0 \text{ min}$ ) is saturated at an exposure time of  $350 \text{ ms}$ . It was acquired with the Zyla detector ( $15 \mu\text{m}$  Gadox scintillator) at  $5 \text{ m}$  distance. b) After  $230 \text{ min}$  of exposure, the intensity decreases by a factor of  $3$ . c) The temporal behaviour of the mean beam intensity is obtained by the empty beam acquisition (green) during two subsequent tomographic scans at  $4$  distances each (bronze). Waveguide alignment scans are performed in between (white). The measurement is completed by waveguide alignment scans (white) and empty beam acquisitions (green). Scale bars are  $1 \text{ mm}$  in the detector plane.

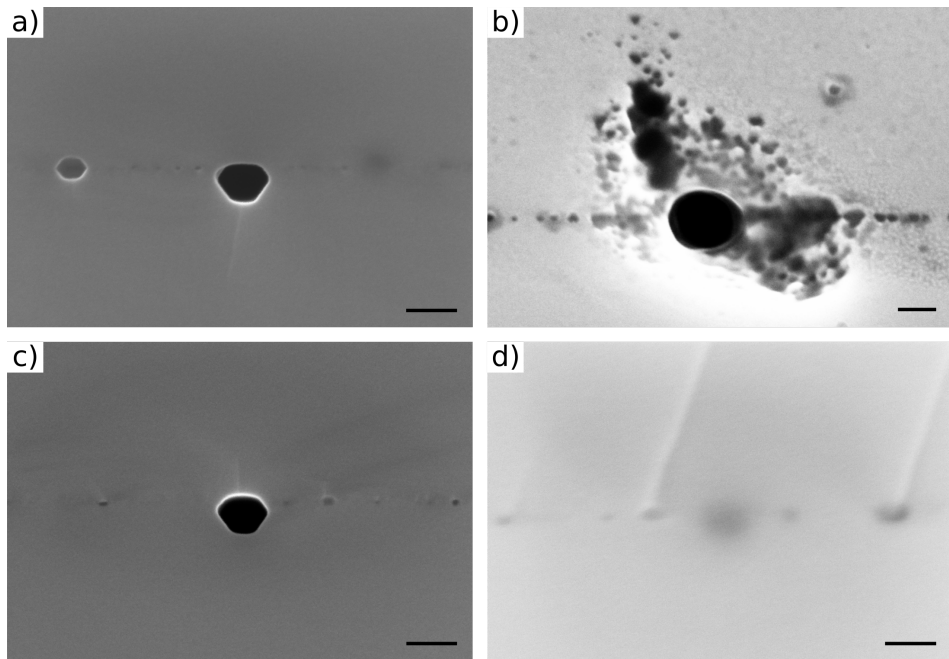


**Fig. 4.3:** Scanning electron microscope images of the waveguide channel obtained prior and post to the X-ray exposure. a) The channel entrance has a diameter of 100 nm before the X-ray exposure. b) The channel entrance shows a severe shape change after the X-ray exposure. The diameter enlarges to 400 nm. c) The channel exit has a diameter of 100 nm before the X-ray exposure. d) The channel exit is closed after the X-ray exposure. Scale bars: a) 100 nm, b) 200 nm, c) 100 nm and d) 100 nm.

After 230 min of usage the intensity decreases by a factor of  $\sim 3$ , as illustrated in the corresponding empty beam image in Fig. 4.2 b). The intensity decay is a combination of two effects. On the one hand, motor drifts of the waveguide positioning stage result in an intensity decrease due to a poor coupling into the waveguide. These can be corrected by repositioning the waveguide as described in step i). As visible in the graph, the repositioning does not necessarily improve the intensity and fails from time to time. On the other hand the overall intensity decay is a deformation of the germanium waveguide itself. Scanning electron microscope images of the channels entrance and exit are obtained before and after the X-ray exposure and are presented in Fig. 4.3. A severe shape change of the channel is visible. The channel entrance is enlarged by a factor of 4 to 400 nm and deformations are distributed around the channel entrance in the form of small holes. The channel exit shows the opposite behavior, since it seems sealed by the relocated germanium. Due to the extended channel entrance it seems like the channel shape transforms into a tapered shape.

For the future, a remedy for the channel transformation is of significant interest. It would enable faster acquisition times of the tomographic scans as well as measurements at higher photon energies with reasonable aspect ratios. Shorter scanning times also have the benefit of less motor drifts during the scan, resulting in improved empty beam corrections and therefore reconstructions.

### 4.3.2 Improved silicon waveguides

The modification of the new silicon waveguide generation is the improved manufacturing accuracy of the the empty channels within the wafer. This fabrication step is performed by *Eulitha* (Villigen, Switzerland), a company that is specialised on manufacturing nanostructures via electron beam lithography. The subsequent wafer bonding step is still performed in-house. In order to investigate the waveguiding properties in terms of resulting beam profile and intensity stability of such a waveguide, empty images of a 1 mm long silicon waveguide with an channel diameter of 100 nm at an energy of 8 keV are considered. The results are presented in Fig. 4.4.

The empty image acquired at the start of the measurement shows the nearly ideal illumination of a Gaussian intensity profile with only a few contributing modes. At an exposure time of 1 s the maximum intensity is  $\sim 90\%$  of the detectors dynamic range (59 823 ADU/65 536 ADU), as shown in Fig. 4.4 a). After 21 h of usage during several tomographic scans, the change of the empty beam image is fractional, as depicted in Fig. 4.4 b). The detailed intensity behaviour over time is illustrated in Fig. 4.4

c). To this end, the mean intensity of the empty images, which is acquired in the aforementioned tomographic scan routine, is plotted for several tomographic scans. The red areas mark the time where no image acquisition takes place, e.g. due to sample exchange and alignment. Apart from one outlier, the beam intensity is very stable over the period of  $t \approx 1$  d. The intensity is increased by the waveguide alignment at the start of each tomographic scan, while it decreases over the period of a tomographic scan due to minor waveguide drifts.

## 4.4 Zyla X-ray detector

The new Zyla HF 5.5 (Andor, USA) X-ray detector is a scintillation-based X-ray detector with a sCMOS sensor. The pixel size is  $6.5 \mu\text{m}$  with a field of view (FOV) of  $2560 \text{ px} \times 2160 \text{ px}$ . In contrast to the available sCMOS detectors at the *GINIX*, the *Pirra* ( $15 \mu\text{m}$  Gadox scintillator, max. frame rate of 18 fps, Photonic Science) detector and *Iris* ( $20 \mu\text{m}$  LuAG scintillator, max. frame rate of 30 fps, Hamamatsu Photonics) detector, it offers exchangeable scintillator materials and a higher frame rate. A simple scintillator exchange is enabled by the detector assembly. A 1:1 fibre-optic-plate (FOP) is bonded on top of the sensor without the scintillator. The scintillation material itself is bonded to an additional FOP, which is then mounted onto the sensor FOP. In that way, a straightforward exchange of the scintillation material is achieved. A detailed description is presented in Ch. 4.4.1.

The detector can be operated in two different shutter modes, the *global shutter* mode (GS) and the *rolling shutter* mode (RS). In the GS mode each pixel is illuminated at the same time. The exposure time and the subsequent readout time limit the maximum frame rate to 50 fps at 16-bit. Higher frame rates are possible using the RS mode. There, contrarily to the GS mode, the sensor is horizontally split in half and the pixel rows are read out from the centre outwards. For each half, the adjacent rows are exposed at slightly different times. The minimum time delay between the rows is the readout time of a single row, which is  $\approx 10 \mu\text{s}$ . The parallelization of pixel exposure and pixel readout results in a maximum frame rate of 100 fps at 16-bit in the *rolling shutter* mode [And17]. Note that for fast moving objects the acquired image shows object distortions due to the different exposure starting points of each row. Furthermore, the frame rate can be increased by reducing the FOV.

The detector provides three different gain modes. The *12-bit (high well capacity)* mode is the low gain mode optimal for the acquisition of images with a high dynamic range.

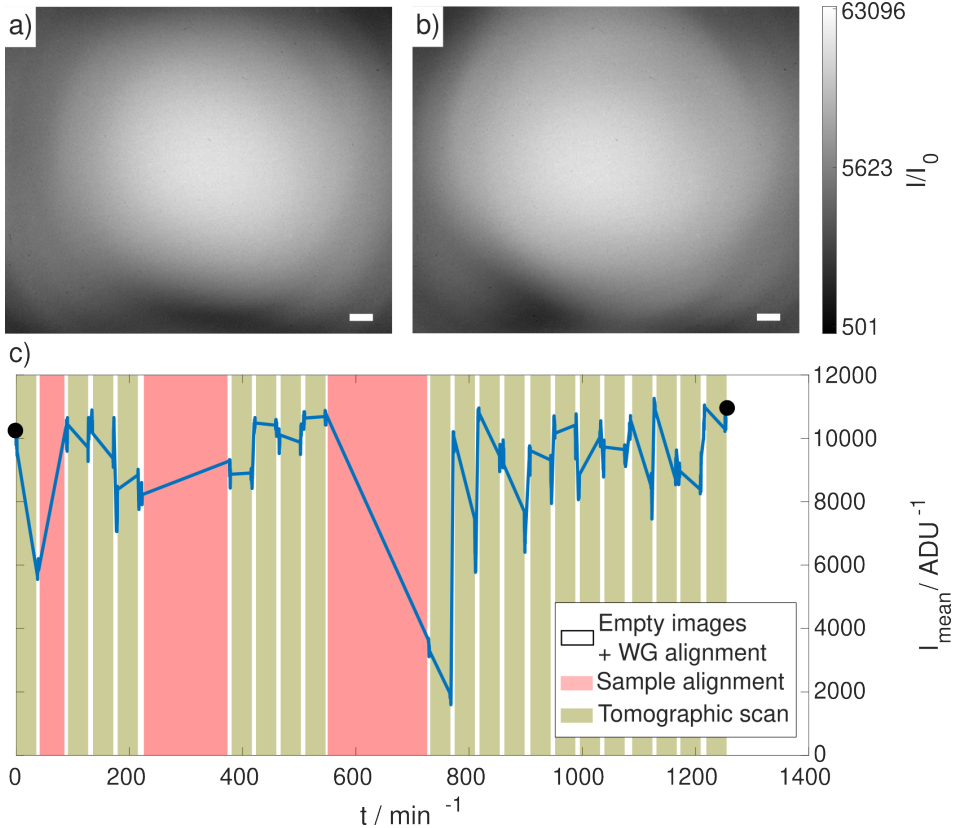


**Fig. 4.4:** Intensity stability of a silicon X-ray waveguide with 1 m optical depth and a channel diameter of 100 nm at 8 keV, for further information see A.3 . a) The first intensity image of the X-ray beam ( $t = 0$  min) is acquired at an exposure time of 1 ms. It was acquired with the Zyla detector (15  $\mu\text{m}$  Gadox scintillator) at 5 m distance. b) After 21 h of exposure, the beam profile and intensity is nearly unchanged. c) The temporal behaviour of the mean beam intensity is obtained by the empty beam acquisition during several tomographic scans, including the following steps: i) the waveguide alignment (white area), ii) the empty beam acquisition, iii) the tomographic acquisition (bronze area) and iv) empty beam acquisition. Apart from the outlier at  $t \approx 650$  min, the beam intensity is stable. Scale bars are 1 mm in the detector plane.



The *12-bit (low noise)* mode is the high gain mode offering a low noise level, which is optimal for the acquisition of weak signals. The *16-bit (low noise and high well capacity)* mode combines the advantages of both modes. "The signal can be sampled simultaneously by both high gain and low gain amplifiers. Therefore, the lowest noise of the sensor can be harnessed alongside the maximum well depth, affording the widest possible dynamic range." [And17].

The commissioning of the camera resulted in an online application note based on propagation-based X-ray phase-contrast [Fro+20b].

#### 4.4.1 Scintillators & Assembly

Three different scintillator materials are available for the Zyla detector: i) LuAG:Ce, ii) YAG:Ce and iii) Gadox. The scintillation properties are presented in Tab. 4.1 based on literature values from [Van02; Nik06; MKN17; GM08; Riv16].

The two important material properties *X-ray stopping power* (X-ray absorption) and *Photon yield* (light emission) are crucial for the conversion of X-ray photons into optical photons. A high conversion paves the way for a high X-ray sensitivity of the detection system. The X-ray stopping power depends on the mass density and the effective atomic number of the scintillator. The absorption curves for the three materials, shown in Fig. 4.5, are obtained from [CXR] by applying the density and chemical formula given by [GM08]. The stopping power can also be increased by increasing the scintillator thickness at the expense of the image resolution, which is discussed in detail below. The *Photon yield* is the ratio of emitted photons ( $\lambda \approx 550$  nm) per absorbed X-ray photon.

The important scintillation properties of the three available scintillation materials are listed in Tab. 4.1 and the absorption curves of the three scintillation materials are presented in fig 4.5. The X-ray sensitivity of the Yttrium Aluminium garnet scintillator (*YAG:Ce*) and the Lutetium Aluminium Garnet (*LuAG:Ce* or *LAG:Ce*) are comparable. The lower absorption power of the *YAG:Ce* is compensated by the two times higher photon yield. However, *YAG:Ce* has an absorption edge at 17 keV, which results in a very low absorption for X-ray energies slightly below the edge. For example, the absorption at 13.8 keV is 23.4%. The advantages of both the scintillators are the short decay times and the single crystal structure. The latter is important for lens-coupled scintillation detectors, due to the low signal broadening within the scintillator as explained in detail below. The Gadolinium oxysulfide also known as *P43*, *GOS* or *Gadox* is a powder scintillator with a median particle size of 2.5  $\mu\text{m}$ . The powder

is mixed with a binding agent and processed to a film. Its X-ray stopping power is comparable to the stopping power of the *LuAG:Ce* scintillator. However, due to its high photon yield of  $60 \text{ ph keV}^{-1}$  the X-ray sensitivity of the *Gadox* scintillator is the highest of the three. The major disadvantage of *Gadox* is its long light decay time of a few hundred microseconds, which severely limits its application in fast imaging applications [GM08], and its powder structure.

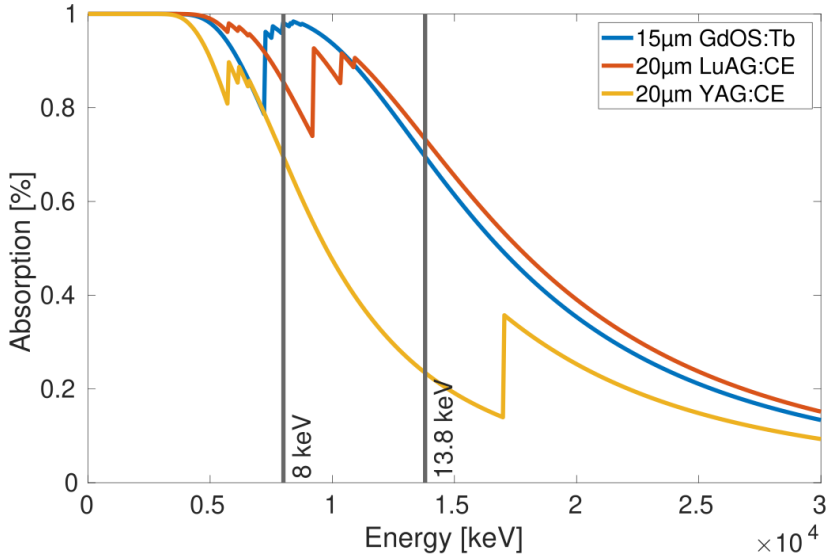


**Fig. 4.5:** Absorption curves for three different Zyla HF scintillators. For the default X-ray energies at the P10 beamline, 8 keV and 13.8 keV (highlighted lines), the Gadox scintillator absorbs 98% of the X-ray photons at 8 keV, while the LuAG scintillator absorbs 73.2% at 13.8 keV). Curves are obtained by [CXR].

**Scintillator resolution** The layer thickness of the scintillator as well as the structure of the scintillation material influences the resolution power of the scintillator. The photons emitted by the scintillator without preferred direction require a transfer onto the sensor. This transfer can either be realized by an imaging optic (fiber or lens) or by a guiding of the emitted photons by the scintillator structure itself, e.g. by the pillar structure of *CsI:Tl* scintillators [Riv16]. The Zyla scintillation units are based on a fiber-coupled optical transfer. To this end, the scintillation layer is coupled to a 3 mm thick fiber optic plate (FOP), which also acts as a substrate for the thin layer. The FOP consists of adjacent optical fibers with a diameter of  $3 \mu\text{m}$ , which are waveguides

Parameter	LuAG:Ce	YAG:Ce	Gadox
Density [ $\frac{g}{cm^3}$ ]	6.73	4.55	7.3
Chemical formula	$Lu_3Al_5O_{12} : Ce$	$Y_3Al_5O_{12} : Ce$	$Gd_2O_2S : Tb$
Type	single crystal	single crystal	grained powder
Thickness [ $\mu m$ ]	20	20	15
Absorption <sub>8keV</sub> [%]	85.6	69.7	98
Absorption <sub>13.8keV</sub> [%]	73.2	23.4	69.5
Photon yield [ph/keV]	12.5	24	60
Decay time [ns]	55	90-120	$6 \times 10^5$
Emission wavelength [nm]	530	550	540

**Table 4.1:** Properties of the three exchangeable Zyla scintillators.

for the incoming photons emitted by the scintillation layer. The FOP provides a 1:1 imaging of the scintillation signal onto the exit surface of the FOP. Nevertheless, the emission signal is broadened, which is described by the point spread function (PSF). The broadening depends on the distance between the emitted photon and the FOP due to the fixed acceptance angle of the FOP fibers. To this end, a thin scintillation layer is preferred to obtain a small scintillator PSF. On the other hand, a thin scintillation layer has a reduced possibility to absorb the X-ray photons resulting in a low X-ray sensitivity. The choice of layer thickness is always a compromise between resolution and sensitivity. Furthermore, the PSF of the scintillator also depends on the structure of the scintillation material itself. The ideal structure of the scintillation layer is in the form of a single crystal material, which does not cause an additional broadening. Some scintillation materials can only be manufactured in a powder format. The powder is mixed with a binding agent and processed to a layer such as the *Gadox* scintillator. In this scintillator layer an emitted light photon has the potential to scatter at the surfaces of the powder grains, which results in an additional broadening [GTE02; Cec+14]. As a consequence, at the same layer thickness the PSF of single crystal material is smaller than the PSF of a powder scintillator. So far, only the scintillator PSF was considered. In fact, the PSF or resolution power of the detector is determined by the PSF of the FOP, which is limited by the waveguide diameter of  $3 \mu m$ , and the PSF of the sensor, which is limited by the pixel size of  $6.5 \mu m$ .

To characterize the effect of the *Gadox* powder structure on the resolution power of the detector system, the 2D resolution of the *YAG:Ce* and the *Gadox* scintillator are determined at the in-house setup *TONI* [Rei+17] (20 keV acceleration voltage and characteristic line  $E_{K_\alpha} = 8 \text{ keV}$  of a rotating copper anode) via the slanted edge method. The test sample is a  $50 \mu m$  thick gold edge. The object to scintillator distance

is 20 mm, due to the beryllium window at the front of the detector, and the source to detector distance is 500 mm. Figure 4.6 compares the resolution of the two scintillators. The *YAG:Ce* scintillator shows a maximum intensity of 12 000 ADU at 15 s exposure time. Compared to this, the *Gadox* scintillator yields 27 400 ADU within 3 s exposure time, which is an intensity increase of a factor of  $\approx 10$ . The 2D resolution is identical for both scintillators, as shown in the MTFs of both images in Fig. 4.6 c). The cross section of the MTF at the 10 %-threshold is at  $40 \text{ cy mm}^{-1}$ , which corresponds to a full period resolution of  $25 \text{ }\mu\text{m} \approx 4 \text{ px}$ . As a consequence, the powder structure of the *Gadox* scintillator does not limit the resolution of the detector, while providing a high sensitivity.

**Assembly** To allow the exchange of the scintillator material, the scintillator is not directly coupled to the sensor. Instead, a separated and compact scintillation unit is manufactured by mounting the scintillator material on an FOP. To protect the detection sensor from mechanical damage during the exchange, it is also equipped with an FOP. The two FOPs are coupled with an optical grease e.g. glycerol in between. To block optical photons a  $200 \text{ }\mu\text{m}$  thick beryllium window is placed in front of the scintillation unit. A detailed procedure to equip the Zyla with a new scintillator can be found in A.1.

#### 4.4.2 Detector pixel response map

[Cro+19] presented an approach to suppress ring artifacts in X-ray computed tomography by calculating and applying a pixel-wise detector response. The idea is to address a gain factor and an offset to every pixel. This approach was applied for the Zyla equipped with the  $15 \text{ }\mu\text{m}$  *Gadox* scintillator and illuminated with X-rays of 8 keV energy at the *GINIX*. The results are shown in figure 4.7. To obtain the sensitivity maps, the following steps are executed:

- (1) For each detector pixel, the dynamic range must be properly scanned by acquiring an ensemble of different intensity values. To this end, the detector was moved through the empty X-ray beam, which is Gaussian shaped by the waveguide, using a mesh scan across the detector's FOV.
- (2) These intensity images are then dark corrected  $I = I_{raw} - I_{dark}$ .
- (3) The 'true' illumination is assumed to be the measured intensity  $I$  smoothed with a 50 px Gaussian kernel  $I_{true} = I * \mathcal{K}_{50px}$ . This assumption is reasonable for the waveguide illumination.

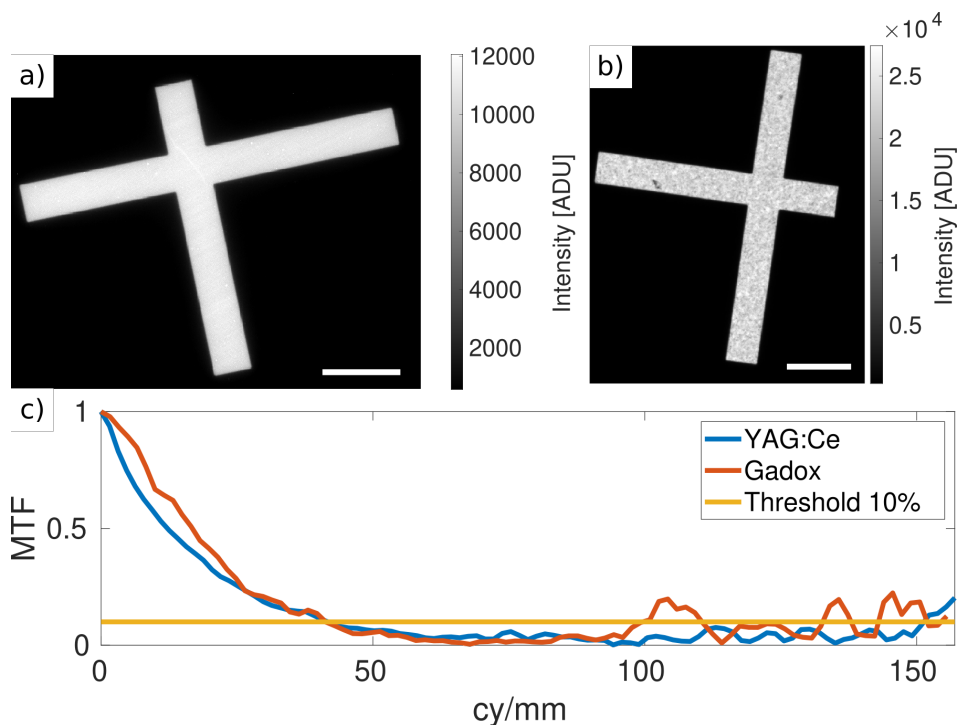


**Fig. 4.6:** Resolution comparison of *YAG:Ce* and *Gadox* scintillator of the Zyla by means of the slanted edge method. The test object is the edge of a  $50\ \mu\text{m}$  thick gold foil. The images are acquired at an in-house X-ray setup (20 keV Bremspectrum of a rotating copper anode  $E_{K\alpha} = 8\ \text{keV}$ ). The object to scintillator distance is 20 mm, and the source to detector distance is 500 mm. a) The raw image of the test structure obtained with the *YAG:Ce* scintillator at 15 s exposure time. b) The raw image of the test structure obtained with the *Gadox* scintillator at 3 s exposure time. c) The MTFs of both images were obtained by slanted edge method. Both scintillators have the same 2D resolution at 10% image contrast. The cross sections are at  $40\ \text{cy}\ \text{mm}^{-1}$ , which corresponds to a full period resolution of  $25\ \mu\text{m} \approx 4\ \text{px}$ . Note different intensities and exposure times of both images. Scale bars denote 1 mm.

(4) A linear fit of the  $k$  true intensities as a function of the  $k$  measured intensities was performed for each pixel  $(i,j)$ :

$$I_{true}(i, j, k) = \alpha_{ij} \cdot I(i, j, k) + \beta_{ij}.$$

(5) The resulting correction maps (sensitivity maps) of the pixel gain  $\alpha_{ij}$  and the pixel offset  $\beta_{ij}$  are shown in figure 4.7(a) and (b), respectively.

(6) These correction maps were applied to the measured intensities, e.g. the empty image  $I_0$ , as follows:

$$I_{0,\text{corr}} = \alpha_{ij} \cdot (I_0) + \beta_{ij}. \quad (4.1)$$

The empty image  $I_0$  without the sensitivity correction shows the grained structure of the *Gadox* scintillator as depicted in figure 4.7(c). In contrast, the application of the sensitivity correction (4.1) on  $I_0$  removes the grained structure of the scintillator as shown in figure 4.7(d).

Additionally, the correction reveals features in the presence of particle holograms within the X-ray illumination. To estimate the location of the particles, the PSD of the particle holograms  $I_{particle} = \frac{I_{0,\text{corr}}}{I_{0,\sigma_{50\text{px}}}}$  was calculated. By changing the Fresnel number, the expected CTF curve is tuned to fit the calculated PSD of  $I_{particle}$ . For a Fresnel number of  $F = 0.0076$  the expected and the measured PSD are in good agreement, illustrated in figure 4.7(e).  $F = 0.0076$  corresponds to a distance of  $x_{01} \approx 0.65$  m behind the waveguide. At that distance the entrance window of the flight tube in form of a kapton foil is located, which apparently is unclean. A CTF phase reconstruction of  $I_{particle}$  reveals the shape of the particles.

Next, the influence of the sensitivity correction on ring artifacts within the tomographic reconstruction was investigated. To this end, a tomographic reconstruction without the sensitivity correction was performed first. All holograms of a tomographic scan  $I_\theta$  were empty beam corrected by  $I_{\theta,\text{corr}} = \frac{I_\theta}{I_0}$  with the empty image  $I_0$  shown in figure 4.8(a), same  $I_0$  as in Fig. 4.7(c). Several ring artifacts are visible in an exemplary 2D slice of tomographic reconstruction as depicted in figure 4.8(b). Note that no phase retrieval was applied. The red arrow is marking a ring artifact that can be assigned to the scintillator defect marked with the red arrow in figure 4.8(a). In comparison, the same 2D slice obtained by the tomographic reconstruction of the corrected intensity images  $I_{\theta,\text{corr}}$  is shown in figure 4.8(c). To this end, the sensitivity correction is applied to the holograms  $I_\theta$  as well as to the empty image  $I_0$ :

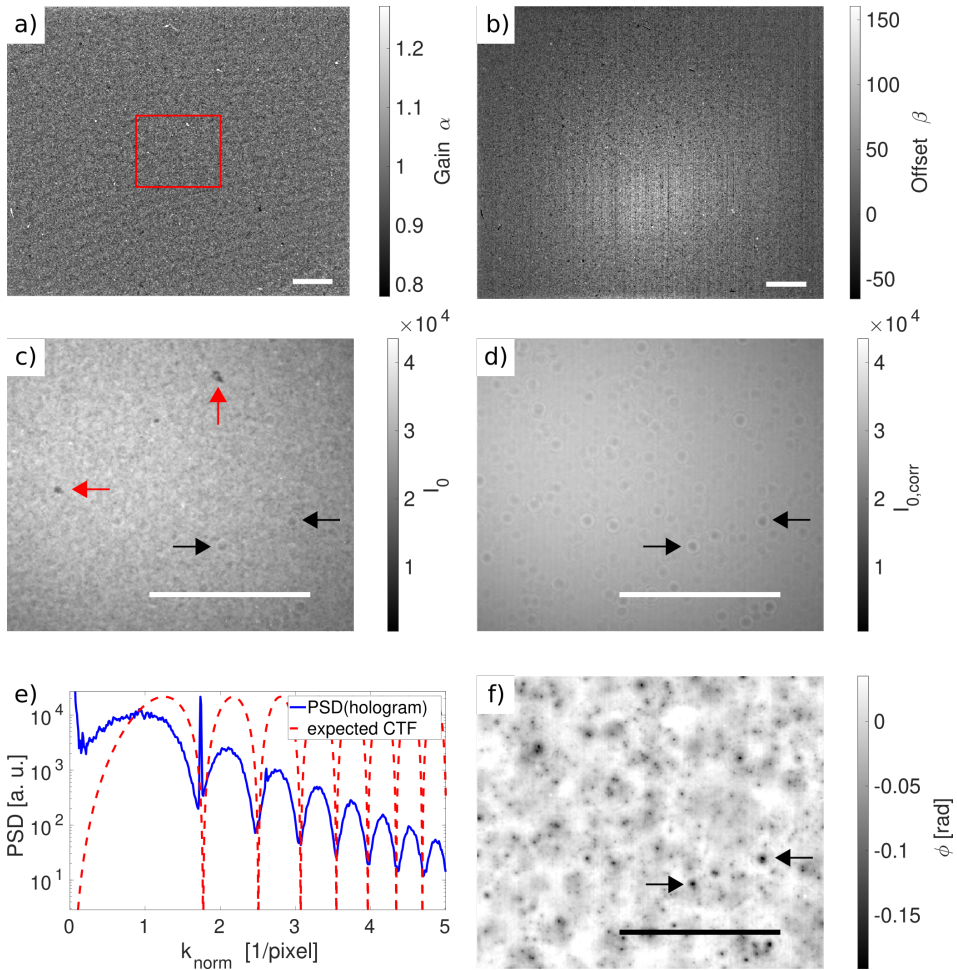


**Fig. 4.7:** Sensitivity map of the Zyla equipped with the  $15\ \mu\text{m}$  Gadox scintillator acquired at 8 keV X-ray energy at the GINIX. a) Gain map  $\alpha$  and b) offset map  $\beta$  for each detector pixel. Red rectangle marks the area of the images (c/d/f). c) Standard empty beam image  $I_0 = I_{\text{raw}} - I_{\text{dark}}$  without sensitivity correction. Illumination is superimposed by the grained structure of the scintillator material. Red arrows mark scintillator features that stand out from the general grained structure. Black arrows mark features of the X-ray illumination (circular shape with holographic fringes). d) Sensitivity corrected empty beam image  $I_{0,\text{corr}} = \alpha \cdot (I_{\text{raw}} - I_{\text{dark}}) + \beta$  reveals the waveguide illumination. It is corrupted by holograms of small particles. e) PSD of the particles obtained from  $I_{\text{particle}} = \frac{I_{0,\text{corr}}}{I_{0,\sigma_{50\text{px}}}}$ .  $I_{0,\sigma_{50\text{px}}}$  represents  $I_0$  filtered with a 50 px Gaussian kernel. f) CTF reconstructed phase shift  $\varphi$  of  $I_{\text{particle}}$ . Particles are located at the distance  $x_{01} \approx 0.65\ \text{m}$  behind the waveguide (entrance window of the flight tube). Scale bars are  $50\ \mu\text{m}$  with a pixel size of 168.6 nm.

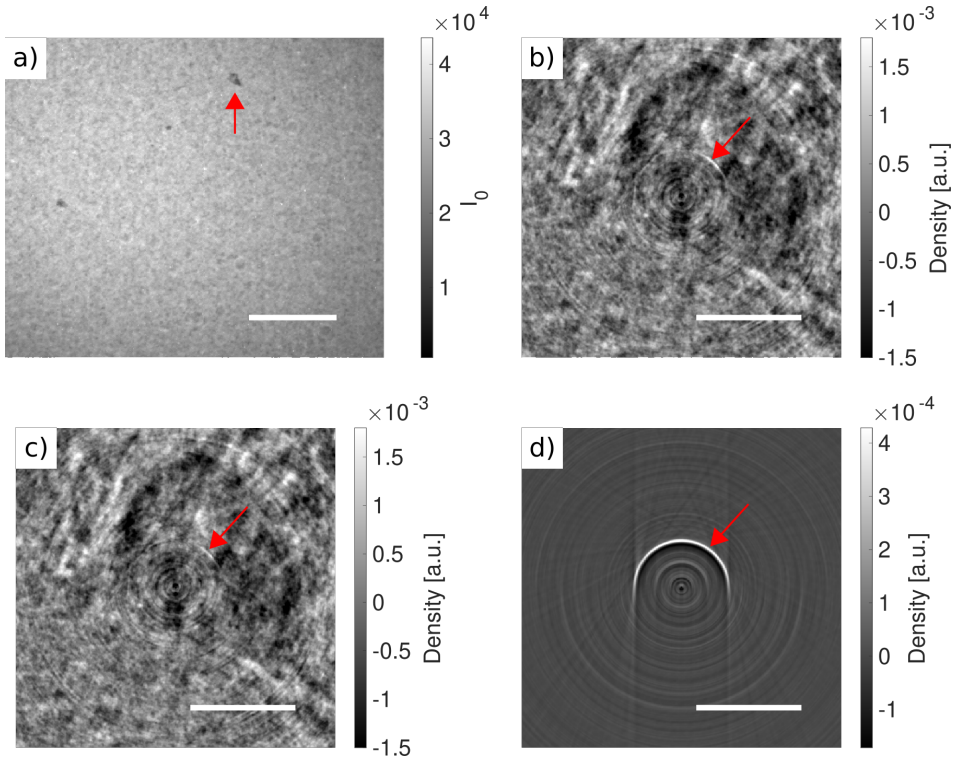


**Fig. 4.8:** Influence of the detector sensitivity correction on the tomographic reconstruction. a) Image of the X-ray illumination  $I_0$  without sensitivity correction. The red arrow marks an example of a strong scintillator feature of the  $15\ \mu\text{m}$  Gadox scintillator at 8 keV. b) Example slice of the tomographic reconstruction obtained from the standard empty beam corrected holograms  $I_{\theta,corr} = \frac{I_{\theta}}{I_0}$ . Phase retrieval was not applied. The reconstruction shows several ring artifacts. The red arrow marks one ring artifact caused by the scintillator feature in a). c) The same example slice as in b) obtained from the sensitivity corrected holograms divided by the sensitivity corrected empty beam image  $I_{\theta,corr} = \frac{\alpha_{ij} \cdot (I_{\theta}) + \beta_{ij}}{\alpha_{ij} \cdot (I_0) + \beta_{ij}}$ . Ring artifacts are still present, but the marked ring is reduced. d) The difference image between b) and c) shows the correction of the marked ring. Scale bars  $25\ \mu\text{m}$  with  $168.6\ \text{nm}\ \text{px}^{-1}$ .



$$I_{\theta, \text{corr}} = \frac{\alpha_{ij} \cdot (I_{\theta}) + \beta_{ij}}{\alpha_{ij} \cdot (I_0) + \beta_{ij}}.$$

The ring artifact caused by the marked scintillator feature is reduced, which is more prominent in the difference image of the slices in figure 4.8(d). The sensitivity correction compensates for ring artifacts caused by incorrect pixel values. Since the reconstructed slice is still flawed by ring artifacts, the origin of these artifacts must be elsewhere. In general, the standard empty beam correction by a simple division is a good approximation, especially for a smooth illumination. In the case of a structured illumination the assumption breaks down, as illustrated in [Hag+14; Hub+18]. Since the particles on the kapton foil structure the illumination beam and are stationary during the tomographic scan, they potentially cause the ring artifacts. To this end, the next step to reduce ring artifacts is to clean or exchange the kapton foil. Another approach to circumvent the immobility of features within the illumination is to shift the sample randomly in both lateral directions for each acquisition angle, as applied in [Hub+18].

## 4.5 3D virtual pathohistology of Covid-19 lung tissue

*This section is based on the publication "3D virtual histology of human pancreatic tissue by multiscale phase-contrast X-ray tomography" with a shared first authorship of M.Eckermann, J.Frohn and M.Reichardt [Eck+20] and covers the results from the waveguide-based holotomography.*

The *WG setup* was used in a proof-of-concept study to investigate Covid-19 affected human lung tissue at sub-cellular resolution. The previous work of [Ack+20] on Covid-19 lungs hypothesizes that a specific variant of new vessel growth - intussusceptive angiogenesis - is significantly more prevalent in Covid-19 lungs as in lungs of patients with H1N1 influenza A. In order to investigate blood vessels and possible vessel growth, tomograms are acquired with the waveguide-based configuration. The acquisition as well as phase retrieval parameters are listed in Tab. 4.2. The image quality and resolution of the unstained paraffin embedded lung tissue is illustrated in Fig. 4.9. The holograms of four different propagation distances are empty-beam corrected and aligned to each other in order to perform the multi distance non-linear CTF-phase retrieval. The tomographic reconstruction via FDK-algorithm reveals the morphology

of the lung tissue sample Fig. 4.9(c) & (d). It shows a large artery filled with erythrocytes. Otherwise, the tissue consists of connective tissue including elastic fibers and collagen as well as smooth muscle tissue. A 3D visualisation is shown in Fig. 4.9(e). In the front plane, a section through the artery is illustrated, showing the 3D distribution of erythrocytes within the blood vessel. The PSD of the holograms is in good agreement with the expected PSD for the given Fresnel number  $F$  (red curve) as shown in Fig. 4.9 (f). The spatial frequencies are normalized by the Fresnel number  $k_{\text{norm}} = \frac{k}{\sqrt{4\pi F}}$ .

To investigate the potential splitting of blood vessels within the reconstructed volume, the segmentation of an exemplary blood vessel is depicted in Fig. 4.9. A series of 2D slices at different heights highlights the difficulties of the segmentation as shown in Fig. 4.9 a). The separation starts with the creation of a branch from the blood vessel (arrow in slice 336). In slice 326, which differs in height by  $1.7 \mu\text{m}$  from slice 336, this branch evolves into an empty and separate capillary. Another  $2 \mu\text{m}$  above, the capillary is entirely filled with cells. Further  $2.3 \mu\text{m}$ , the capillary is empty again and has a diameter of about  $2.8 \mu\text{m}$ . The segmentation of the blood vessel with all its separated branches is indicated for slice 336 in Fig. 4.9 b) by the red lines. In this slice, three capillaries have already separated from the main vessel, while the fourth starts to emerge, indicated by the red arrow. The 3D shape of the blood vessel is illustrated by the 3D rendering of the segmentation, shown in Fig. 4.9 c). Blood vessels or capillaries, that are spatially separated in the 2D slice, can now be connected due to the access to the 3D volume. A manual sliding through a series of 2D slices at different heights is an accurate approach to quickly detect such connections by eye. This sliding also provides the opportunity to detect cell-filled capillaries, which is impossible on a single 2D slice, such as slice 314. An automated segmentation of such filled capillaries requires more elaborate segmentation routines, apart from standard methods such as thresholding, watershed or region growing. In addition, the segmentation routine must be able to distinguish between different structures with the same gray values. For example, empty capillaries and empty alveoli are filled with paraffin, resulting in the same gray values. Deep learning methods, which are trained on manual segmented data sets, are a promising approach for an automatic segmentation routine [MNA16]. The segmentation of the presented capillary is performed manually.

Variable	Value
GINIX run	94 (April 2020)
X-ray energy [keV]	8
Detector	Zyla 5.5
$x_{01,min}$ [mm]	125
$x_{02}$ [mm]	5100
$p_{eff}$ [ $\mu\text{m}$ ]	168.2
Field of view [ $\mu\text{m}$ ]	430 x 360
Fresnel number $F^r$	0.0015
Waveguide	Si - 100 nm diameter
Number of distances	4
Angular range	180°
Number of projections	1501
Exposure time	1 s
Phase retrieval	non-linear CTF
lim1	0.0008
lim2	0.4
$\beta/\delta$	1/90

**Table 4.2:** Acquisition and reconstruction parameters for the tomographic scan of the unstained paraffin embedded Covid-19 affected human lung that is presented in Fig. 4.9.

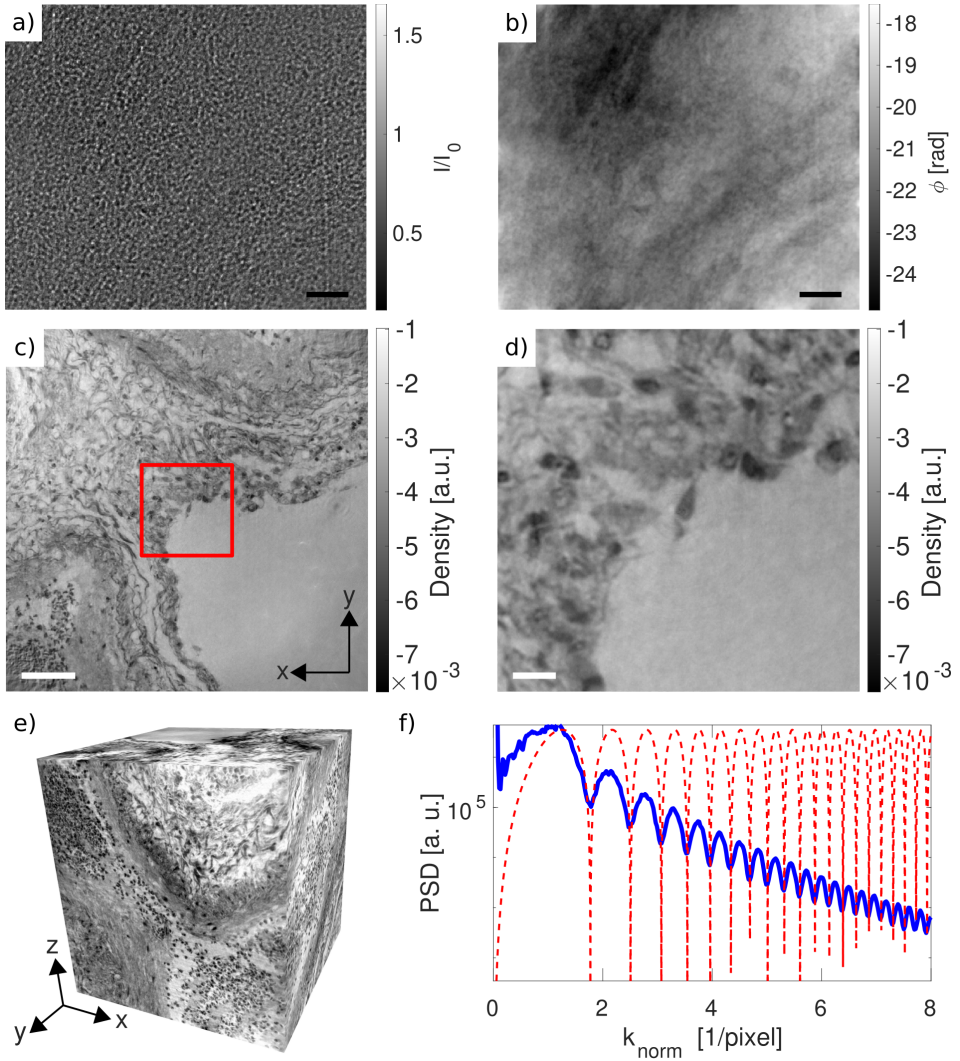


**Fig. 4.9:** Phase retrieval and tomographic reconstruction of unstained paraffin embedded lung tissue from Covid-19 patients. a) Exemplary empty-beam corrected hologram of the object at distance  $x_{01} = 125$  mm. b) Reconstructed phase distribution  $\phi$  from 4 distances of the hologram in (a) via non-linear CTF-algorithm. c) Exemplary reconstructed tomographic slice in  $xy$ -plane. d) Magnified area marked as the red rectangle in (c). e) Visualisation of the reconstructed 3D volume. f) Power spectral density of the hologram in (a). The spatial frequency is normalized by the Fresnel number  $F$  such that the first CTF minimum correlates to  $1 \text{ px}^{-1}$ . Scale bars:  $50 \mu\text{m}$  in (a), (b), (c) and  $10 \mu\text{m}$  in (d).

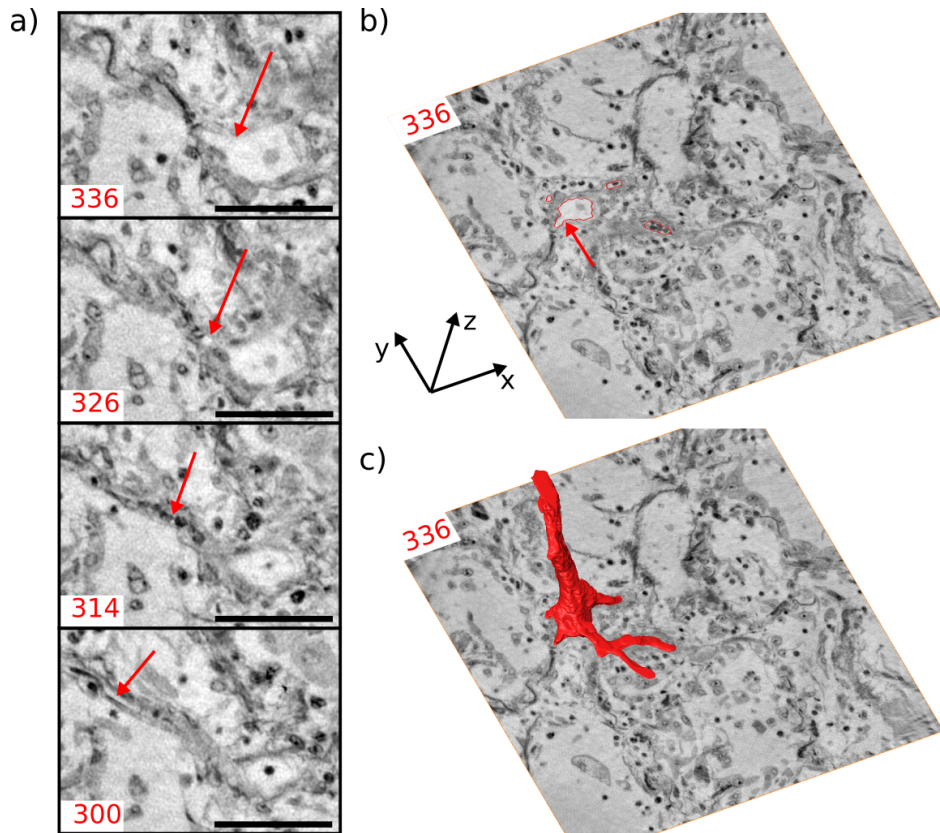


**Fig. 4.10:** Segmentation of the blood vessel network within the reconstruction of unstained paraffin embedded lung tissue from Covid-19 patients. a) Series of slices in z-direction illustrates the separation of a capillary ( $\approx 5 \mu\text{m}$  diameter) from a blood vessel. The red arrow marks the separating capillary. In slice 314, the capillary is entirely filled with erythrocytes. b) Red lines in the entire virtual slice (336) represent the contours of a manual segmentation of the blood vessel network. Three capillaries are already separated from the main vessel, while the fourth starts to emerge, indicated by the red arrow. c) Segmentation illustrating the 3D structure of the blood vessel network. Scale bars:  $50 \mu\text{m}$ . Figure and caption taken from [Eck+20].

## 4.6 Discussion

A new generation of X-ray waveguides shows promising improvements for the X-ray beam properties utilized in the *WG setup*. At an X-ray energy of 8 keV, 1 mm long silicon waveguides with a diameter of 100 nm provide a high photon flux, which saturates the Zyla detector within one second, paired with beam stability over the course of one day. This stability reduces the artifacts introduced by a flawed empty-beam correction due to a changing illumination. The drawback of silicon as the cladding material of the waveguide is its low X-ray absorption power. For experiments at higher X-ray energies e.g. at 13.8 keV either the waveguide length needs to be increased or a different cladding material is required. Germanium is a good candidate for the cladding material, due to its absorption edge at 11.1 keV. Such germanium waveguides show a  $\sim 3$  times higher photon flux (Zyla saturation at 0.35 s) compared to the silicon waveguide. But its intensity decreases radically over time due to physical changes of the channel shape. Understanding these shape changes in detail and taking the corresponding countermeasures would be the next major hardware upgrade for the *WG setup*. At sub-second exposure times, a switch from the *step and shoot* acquisition scheme of the tomographic scans towards a *continuous* acquisition scheme further reduces the total scanning time, due to the saved overhead time per image. Shorter acquisition times also reduce the time for waveguide position drifts and therefore makes the waveguide alignment step obsolete. Furthermore, the position of the waveguide requires a sub-micrometer accuracy and is the most sensitive part of the setup. An improved drift-resistant mounting of the waveguide would be a major upgrade for this setup, since the empty beam correction is more accurate and the time for the waveguide alignment step can be saved.

A customized 15  $\mu\text{m}$  thick *Gadox* scintillator combined with the fiber-coupled Zyla 5.5 HF detector shows a higher sensitivity compared to the *LuAG:Ce* and the *YAG:Ce* scintillators for X-ray energies of 5-20 keV. Its grained structure has no influence on the resolution power of the detector due to the large pixel size of 6.5  $\mu\text{m}$ . Although the grained *Gadox* structure is reproduced in the empty beam image itself, an empty beam division corrects for the scintillator structure. However, the grained structure of the empty image hides fine structures within the X-ray illumination. By calculating a sensitivity map of the detector the true illumination profile can be revealed. The sensitivity map corrects systematic detection errors of differing pixel responses and ring artifacts in tomographic reconstructions are reduced.

3D virtual histology in this configuration was used to investigate Covid-19 affected

---

human lung tissue. The image contrast of the phase reconstruction is sufficient to enable 3D tissue quantification at sub-cellular resolution. Here, the splitting of a blood vessel with capillaries of a few micrometer in diameter was highlighted in 3D to search for intussusceptive angiogenesis within Covid-19 affect lung tissue [Ack+20]. The access to the 3D shape of the blood vessel reveals the connection of capillaries, which are separated in different 2D slices. Furthermore, 3D virtual histology offers the opportunity to investigate several hundreds of 2D slices. Since 3D virtual histology is nondestructive, it can therefore support histopathology prior to histology examination, which can be performed on well-chosen sections after the scan. In particular, immunohistochemical staining can help to inform about on the biomolecular origin of the certain structures.





# Multi-scale approach (Scale III): Super-resolution in-line holography

---

# 5

## 5.1 Motivation

The third scale of the multi-scale approach aims to push the highest resolution available at the GINIX setup to the next level. Up to now, high resolution three-dimensional data sets are recorded by holotomographic acquisitions in the waveguide configuration at high geometrical magnifications, see Ch. 4. To this end, the established acquisition scheme utilises a scintillation-based detector with a small pixel size to acquire the magnified holograms within the primary X-ray beam. The subsequent phase reconstruction is performed via the CTF-approach (Ch. 2.2.3), which assumes a plane wave illumination. The actual cone beam geometry of the setup can be treated in an equivalent parallel beam geometry with effective coordinates in combination with the empty-beam division of the holograms.

Soltau et al. [Sol+21] presented a novel acquisition and reconstruction scheme for X-ray in-line holography (2D images) at the GINIX setup, which resulted in an improved 2D resolution compared to the aforementioned approach. There, the scintillation-based detector was replaced by a single photon counting detector *Eiger 4M* (Dectris, Switzerland). It provides a larger area of detection and more importantly it enables the detection of weak signals, due to its noise-free readout and higher dynamic range compared to scintillation-based detectors. This allows for the detection of the waveguide illumination tails, which results in an extended hologram, and the detection of coherent diffracted photons beyond the cone beam illumination, which will be referred to as the "CDI signal" (based on Coherent Diffractive Imaging) in the following. The simultaneous detection of the holographic and the CDI signal increases the numerical aperture (NA) of the setup and improves therefore its resolution [Lat21].

The combined acquisition of both signals by placing the sample downstream of a X-ray focus has already been reported in different terms. In [Wil+06; Wil+10] it is called *Fresnel coherent diffractive imaging (FCDI)* and in [Abb+08] *keyhole coherent diffractive*

*imaging (KCDI)*. [LLF12] shows the relation between holography and CDI for optical light and names it *holographic coherent diffraction imaging (HCDI)*. In [Luu+14] FCDI is combined with ptychography and tomography. In FCDI and KCDI the X-ray beam is focused by a Fresnel zone plate (FZP), while the central beam part is blocked by an upstream beam stop and higher order contributions of the FZP are removed by an order sorting aperture (OSA) in the focal plane. The unique use of an X-ray waveguide at the GINIX, which generates a highly confined point source, neither requires a beam stop nor an OSA.

The phase reconstruction scheme presented in Soltau et al. [Sol+21] is an iterative scheme based on alternating projections. Compared to the CTF-approach, it separately reconstructs the complex-valued illumination wavefield  $P$  in the object allowing for a division of  $P$  from the object exit wavefield  $\psi = P \cdot O$  in the object plane rather than the empty-beam division is in the detection plane. Furthermore, the far-field propagation of the curved phase of  $P$  from the object plane to the detection plane via Fourier transform maintains the actual cone beam geometry of the experiment. In addition, the far-field treatment results in a smaller effective pixel size compared to the equivalent parallel beam geometry of the CTF-approach in the object plane. [Sol+21] reported a 2D resolution of 11.2 nm half width at half maximum for a thin pure phase object, which is smaller than the effective pixel size obtained by the geometrical magnification in the CTF-approach  $p_{eff} = 17.3$  nm. To this end, this novel approach is named **Super-resolution in-line Holography (SrH)**.

In this work, the SrH scheme is adapted to 3D imaging using tomographic acquisitions in a proof-of-principle experiment. Furthermore, the iterative reconstruction scheme is revised, since the assumption of a pure phase object is usually not applicable for a 3D object. A unique extraction of the object transmission function  $O$  from the object exit wavefield  $\psi = P \cdot O$  enables the application of various constraints onto the object transmission function  $O$  in the reconstruction plane. In the remainder of this chapter, a detailed description of the experiment and the reconstruction scheme is presented along with the resolution determination in 3D.

## 5.2 Experimental realization

**Test object** Lines and spaces or Siemens star patterns are common test patterns to determine the 2D resolution of an imaging setup. However, the transition of such a pattern from 2D to 3D creates strong phase gradients at the edges of the spoke if

the spoke is parallel to the X-ray beam direction. These edges complicate the phase retrieval of the object. Thus, we have designed a novel test pattern in form of a 2D spiral that is extended in the third dimension. The spiral circumvents strong phase gradients, which is more suitable for the phase reconstruction step. The test pattern was manufactured by XRnanotech (Villigen-PSI, Switzerland) with a total diameter of  $50\ \mu\text{m}$ , consisting of five  $2\ \mu\text{m}$  thick spokes and a height of  $150\ \mu\text{m}$ , as illustrated in Fig. 5.4a). It is supported by 3 surrounding helical spokes. The sample material is the photon resin *IP-S* (Nanoscribe, Karlsruhe, Germany), which has the index of refraction coefficients of  $\beta = 1.1 \times 10^{-9}$  and  $\delta = 1.39 \times 10^{-6}$ , which results in a ratio of  $\sim 1/1250$  at 13.8 keV. The mass density is  $1.2\ \text{g cm}^{-3}$ . With these object properties a maximum phase shift of  $\phi_{max} < 1.5\ \text{rad}$  is expected.

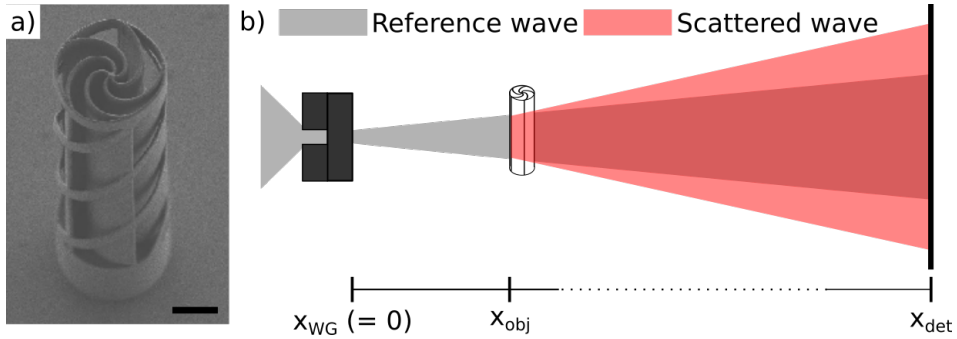


**Fig. 5.1:** Scheme of the Super-resolution in-line Holography setup at the *GINIX*. a) The 3D spiral test pattern to determine the 3D resolution of the setup imaged by a SEM. b) A sketch of the SrH setup. The reference beam (gray) is focused by a KB-mirror system. Two crossed 1d multilayer waveguides (Ge/Mo/C/Mo/Ge) act as a 2D waveguide for the KB-focused X-ray beam. The divergent X-ray beam generated by the waveguide interacts with the object, which is placed at  $x_{obj} = 12.7\ \text{mm}$ . The scattered wave is marked as red. The photon-counting detector Eiger 4M is placed at  $x_{det} = 5.1\ \text{m}$  behind the waveguide exit. Scale bars: a)  $20\ \mu\text{m}$ .

**Setup** The experiment is performed at the synchrotron endstation *GINIX* [Sal+15] at the P10 coherence beamline at PETRA III (DESY). A sketch of the setup is shown in Fig. 5.1b). The X-ray beam is monochromatized by an Si(111) channel cut to an energy of 13.8 keV and focused by the KB-mirror system onto the entrance channel of an X-ray waveguide. The waveguide consists of two crossed 1d multilayer waveguides (Ge/Mo/C/Mo/Ge) as described in [Krü+12; Krü+10]. The guiding layer thickness is 58 nm. The distance between waveguide exit and sample is  $x_{01} = x_{obj} = 12.7\ \text{mm}$ .

The interaction of the reference beam (gray) with the object results in a scattered wave (red). The detector is a photon-counting Eiger 4M (Dectris, Switzerland) with a FOV of  $2070 \text{ px} \times 2167 \text{ px}$  and a pixel size of  $75 \mu\text{m}$ . It is placed at a distance of  $x_{02} = x_{det} = 5100 \text{ mm}$  behind the waveguide exit. The acquisition parameter for the tomographic scan are listed in Tab. 5.1. 10 empty images are acquired prior and post to the tomographic scan.

Variable	Value
GINIX run	102 (April 2022)
X-ray energy [keV]	13.8
Detector	Eiger 4M
$x_{01}$ [mm]	12.7
$x_{02}$ [mm]	5100
$p_{eff,CTF}$ [nm]	186.8
Geometric magnification	401.6
Fresnel number $F$	0.0306
Waveguide	<i>ID4743: 58nm (2021-08-26)</i>
Number of distances	1
Angular range	$180^\circ$
Number of projections	758
Exposure time	0.4 s

**Table 5.1:** Acquisition parameter for the SrH tomographic scan.

### 5.3 Reconstruction scheme

The idea of the reconstruction scheme is to first reconstruct the complex-valued X-ray illumination wavefield  $P$  in the waveguide plane using an iterative *error reduction* approach [Fie82]. As shown in [Sol+21] this reconstruction results in similar results as the reconstruction by ptychography. The determination of the illumination wavefield in the object plane via near-field propagation provides the opportunity to perform a division of the wavefields in the object plane rather than intensity division in the detection plane. The object transmission function  $O$  is reconstructed in a second iterative reconstruction approach based on alternating projections and far-field propagation. A detailed description of the scheme is given below.

**Probe reconstruction** The iterative phase reconstruction scheme *Error Reduction (ER)*, which is based on alternating projections, is used to reconstruct the complex-

valued wavefield of the illumination  $P_{WG}$  in the exit plane of the waveguide [Krü+10]. The reconstruction scheme is illustrated in Fig. 5.2. One iteration consists of the following four steps: Forward propagation into the detector plane  $\mathcal{F}(\cdot)$ , application of the magnitude constraint in the detector plane  $\mathcal{P}_M(\cdot)$ , back propagation into the waveguide plane  $\mathcal{F}^{-1}(\cdot)$  and application of the support constraint  $\mathcal{P}_S(\cdot)$ :

$$P_{WG}^{n+1} = \mathcal{P}_S [\mathcal{F}^{-1} [\mathcal{P}_M [\mathcal{F} (P_{WG}^n)]]]$$

After  $n = 100$  iterations, the probe wavefield  $P_{WG}^{100}$  is Fresnel propagated into the object plane  $P_{obj} = \mathcal{F}_r(P^{100})$ . The result of a consistency check of the reconstructed probe wavefield  $P_{obj}$  is that the modulus of its far-field propagation  $|\mathcal{F}[P_{obj}]| \approx \sqrt{I}$  is in good agreement with the measured amplitude of the empty image  $\sqrt{I}$ .

**Object reconstruction** The interaction between object transmission function  $O$  and the illumination wavefield  $P_{obj}$  is given by the wavefield  $\psi$ .

$$\psi = P_{obj} \cdot O$$

The object transmission function  $O$  describes the interaction of an object with the incident radiation. The object absorption  $A$  is given by  $A = |O|$  and the object phase shift by  $\Phi = \arg [O]$ .

$$O = A \cdot e^{i \cdot \Phi}$$

A refractive object approach [Dav+11; Kos+13; Wit20] is introduced to avoid the phase wrapping of phase shifts  $\Phi > 2\pi$ . Accordingly, the object transmission function  $O$  is expressed as an exponential function of the wavefield  $\tilde{O}$ , which is referred to as the *refractive object*.

$$O = e^{i \cdot \tilde{O}}$$

Now, the object absorption is given by  $A = |O| = e^{-\text{Im}[\tilde{O}]}$  and the object phase by  $\Phi = \arg [O] = \text{Re}[\tilde{O}]$ .

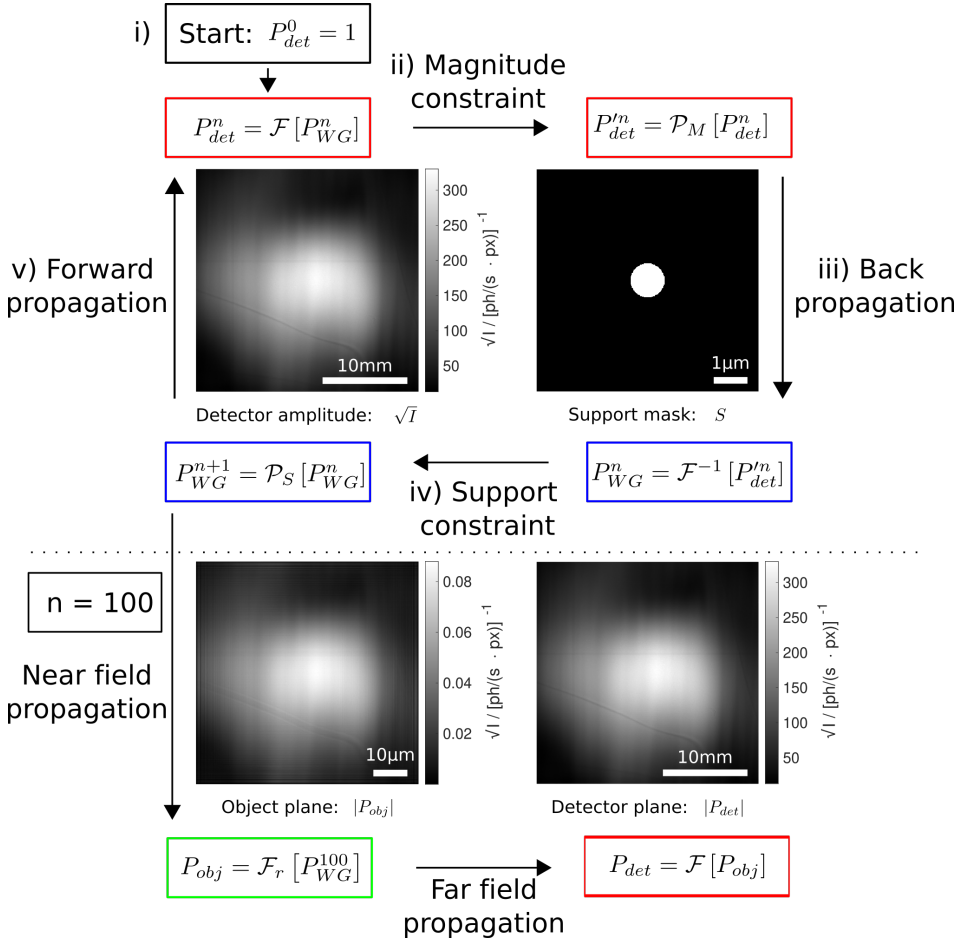


**Fig. 5.2:** Iterative scheme for reconstruction of the complex-valued illumination function  $P^n_{obj}$ . One iterations is as follows: i) The reconstruction starts in the plane of the X-ray detector (marked red) with  $P^n_{det}$  or the initial guess  $P^0_{det} = 1$ . ii) The magnitude constraint  $\mathcal{P}_M$  is applied on the wavefield via  $\mathcal{P}_M[P^n_{det}] = \frac{P^n_{det}}{|P^n_{det}|} \cdot \sqrt{I}$ .  $\sqrt{I}$  is the square root of the measured detector intensity. iii) The updated wavefield is back propagated into the waveguide plane (marked blue) via an inverse Fourier transform  $\mathcal{F}^{-1}$ . iv) The support constraint  $\mathcal{P}_S$  is applied on the wavefield via the pixelwise multiplication of the support mask  $S$  and the wavefield  $\mathcal{P}_S[P^n_{WG}] = P^n_{WG} \cdot S = P^{n+1}_{WG}$ . v) The last iteration step is to propagate the updated wavefield forward into the detector plane via a Fourier transform  $\mathcal{F}$ . After  $n = 100$  iteration steps the wavefield  $P^{100}_{WG}$  is propagated via a Fresnel propagation into the object plane (marked green). The far field propagation via Fourier transform of the wavefield  $P_{obj}$  provides the complex-valued illumination function in the detector plane  $P_{det}$ . Note that the scale bars differs depending on the reconstruction plane.

The object reconstruction scheme consists of the following eight steps as illustrated in Fig. 5.3. The upper index  $n$  indicates the iteration number, while the lower index indicates the step number within one iteration:

- i) The start is the initial guess for the refractive object  $\tilde{O}_i^0$ . A pure phase object ( $A^0 = 1$ ) with a guessed phase distribution  $\Phi^0$  is assumed.  $\Phi^0$  is obtained by a prior CTF reconstruction  $\Phi^0 = \Phi_{CTF}^0$ . This results in an initial guess of:

$$\tilde{O}_i^0 = \Phi_{CTF}^0 + i \cdot 0$$

- ii) Multiplication of the probe wavefield  $P_{obj}$  (object plane) and the object transmission function  $O_i^n = e^{i\tilde{O}_i^n}$ :

$$\psi_{ii}^n = P_{obj} \cdot O_i^n = P_{obj} \cdot e^{i\tilde{O}_i^n}$$

- iii) Forward propagation of the wavefield  $\psi_{ii}^n$  to the detector plane via a Fourier transform  $\mathcal{F}$ :

$$\psi_{iii}^n = \mathcal{F}[\psi_{ii}^n]$$

- iv) Application of the magnitude constraint  $\mathcal{P}_M$  on the wavefield  $\Psi_{iii}^n$  by replacing the modulus of the wavefield with the square root of the measured intensity  $\sqrt{I}$ :

$$\psi_{iv}^n = \mathcal{P}_M[\Psi_{iii}^n] = \sqrt{I} \cdot e^{i \arg(\psi_{iii}^n)}$$

- v) Back propagation via inverse Fourier transform  $\mathcal{F}^{-1}$  of the updated wavefield  $\psi_{iv}^n$ :

$$\psi_v^n = \mathcal{F}^{-1}[\psi_{iv}^n]$$

- vi) Extraction of the refractive object transmission function  $\tilde{O}_{vi}^n$  from the wavefield  $\psi_v^n$ : In order to account for low intensity regions of the illumination wavefield  $P_{obj}$  an object update step based on the ePIE algorithm [MJL17] and adapted for a refractive object [Wit20] is applied to the wavefield  $\psi_v^n$ . The parameter  $\alpha$  sets the strength of the update step. In this thesis an  $\alpha$  value of 0.9 is chosen. A

detailed derivation of the formula is provided in A.2.

$$\tilde{O}_{vi}^n = \tilde{O}_i^n + \alpha \cdot \frac{i \cdot \psi_{ii}^{*,n}}{|\psi_{ii}^{*,n}|_{max}^2} \cdot (\psi_v^n - \psi_{ii}^n)$$

vii) Application of a negativity constrain  $\mathcal{P}_{range}$  on the phase  $\Phi_{vi}^n = \text{Re} [\tilde{O}_{vi}^n]$  of the refractive object transmission function  $\tilde{O}_{vi}^n$ :

$$\Phi_{vii}^n = \mathcal{P}_{range} [\Phi_{vi}^n] = \begin{cases} 0, & \text{if } \Phi_{vi}^n \geq 0 \\ \Phi_{vi}^n, & \text{otherwise} \end{cases}$$

viii) The final step to obtain the updated refractive object  $\tilde{O}_i^{n+1}$  is the application of a homogeneous object constraint  $\mathcal{P}_{ho}$  on the objects phase  $\Phi_{vii}^n$ .

$$\tilde{O}_i^{n+1} = \tilde{O}_{viii}^n = \mathcal{P}_{ho} [\Phi_{vii}^n] = -i \cdot \frac{\beta}{\delta} \cdot \Phi_{vii}^n + \Phi_{vii}^n$$

In conclusion, the operator notation for one iteration step is:

$$\tilde{O}^{n+1} = \left(1 - i \frac{\beta}{\delta}\right) \mathcal{P}_{range} \text{Re} \left\{ \tilde{O}^n + \alpha \cdot \left( \frac{i \psi^{*,n}}{|\psi^{*,n}|_{max}^2} \cdot (\mathcal{F}^{-1} \mathcal{P}_M \mathcal{F} \psi^n - \psi^n) \right) \right\}$$



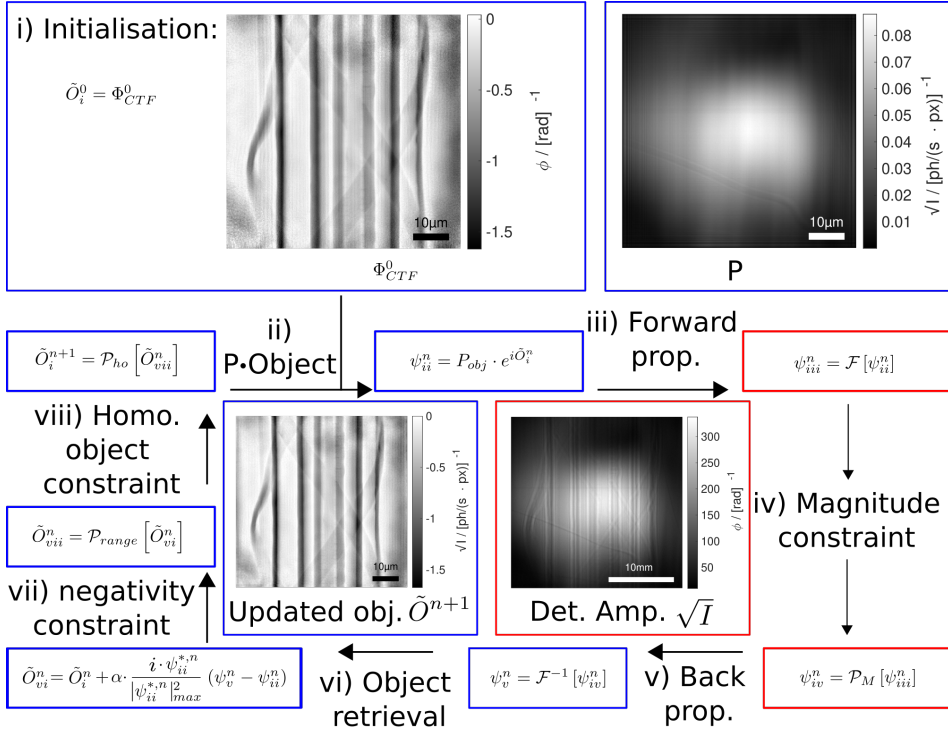


**Fig. 5.3:** Iterative scheme for reconstruction of the complex-valued refractive object transmission function  $\tilde{O}$ . One iterations is as follows: i) The iteration starts with the reconstructed probe wavefield  $P$  and the reconstructed refractive object transmission function  $\tilde{O}$  or the intial guess  $\tilde{O}_i^0$  obtained by the CTF reconstruction  $\Phi_{CTF}^0$ . ii) Multiplication of the probe wavefield  $P$  and the object transmission function. iii) Forward propagation of the wavefield via Fourier transform. iv) Application of the modulus constraint  $\mathcal{P}_M$ . v) Back propagation of the updated wavefield  $\Psi'_n$  into the object plane via inverse Fourier transform  $\mathcal{F}^{-1}$ . vi) Retrieval of the object transmission function from back propagated wavefield via a modified ePIE approach. vii) Application of a negativity constraint on the phase of the refractive object. viii) Application of a homogeneous object constraint to obtain the absorption of the refractive object.

**Fig. 5.4 (next page):** An exemplary detector image obtained in the SrH setup at the *GINIX*. a) Left: The raw image of the detector is represented on a logarithmic scale. Right: The magnified area shows the weak contrast of the 3D spiral object. b) Left: The empty beam corrected image shows the holographic contribution to the detected signal. Right: The magnified area reveals the shape of the 3D spiral. For a comparison, the blue square indicates the FOV of the scintillation detector Zyla (2560 px  $\times$  2160 px at 6.5  $\mu\text{m}$  pixel size), which is used in X-ray waveguide-based holography setup at the *GINIX*. c) Right: The difference between raw image and empty image shows the scattered signal. Note that some of the horizontal and vertical scattered signal is part of the waveguide illumination, due to the design of two crossed 1d waveguides. Right: The inset shows the signal next to the reference beam. The histogram of this scattered signal is shown in Fig. 5.5. Scale bars: 10 mm in the detector plane.

## 5.4 Results

**Detector images** The large field of view of the EIGER 4M detector allows for the acquisition of the holographic signal as well as the CDI signal of the object. Figure 5.4 depicts an exemplary raw detector image as well as the signal contributions acquired at an exposure time of 0.4 s. The raw detector image is represented on a logarithmic scale in Fig. 5.4 a). The detector FOV captures the entire waveguide illumination with the potential to use the scattered signal next to the waveguide illumination for phase retrieval. The magnified area shows that the illumination is Gaussian shaped in the center with horizontal and vertical extensions as expected by the waveguide design of two crossed 1d waveguides [Krü+10]. The object in the center of the beam is barely visible. To highlight the holographic signal, the raw image is divided by an empty beam image, as shown in Fig. 5.4 b). This empty beam corrected image reveals the contrast obtained by the interaction between reference wave and scattered wave. However, it does not show the diffracted wavefield beyond the cone beam illumination. The general shape of the 3D spiral is recognised. For a comparison, the blue square indicates the FOV of the scintillation detector Zyla (2560 px  $\times$  2160 px at 6.5  $\mu\text{m}$  pixel size), which is commonly used in X-ray waveguide-based holography setup at the *GINIX*.

The difference image between the raw image and the empty image isolates the CDI signal, as illustrated in Fig. 5.4 c). The absorption of the object is negligible, since the mean value of the difference image is  $\bar{I} = 0$ . To check the CDI signal an exemplary area next to the waveguide illumination is depicted. It shows the weak signal next to the direct X-ray illumination. The histogram of that area is shown in Fig. 5.5. The detected

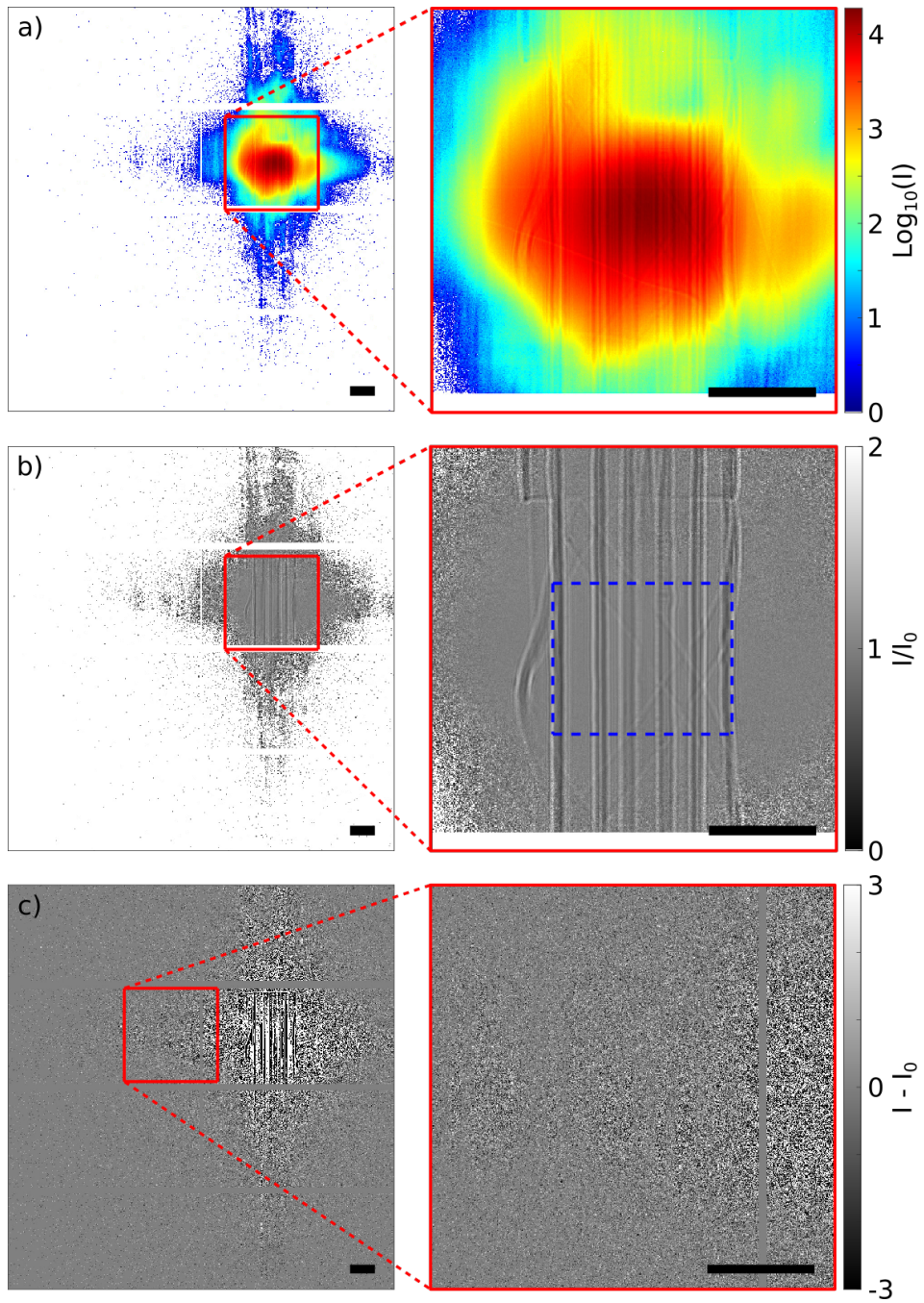
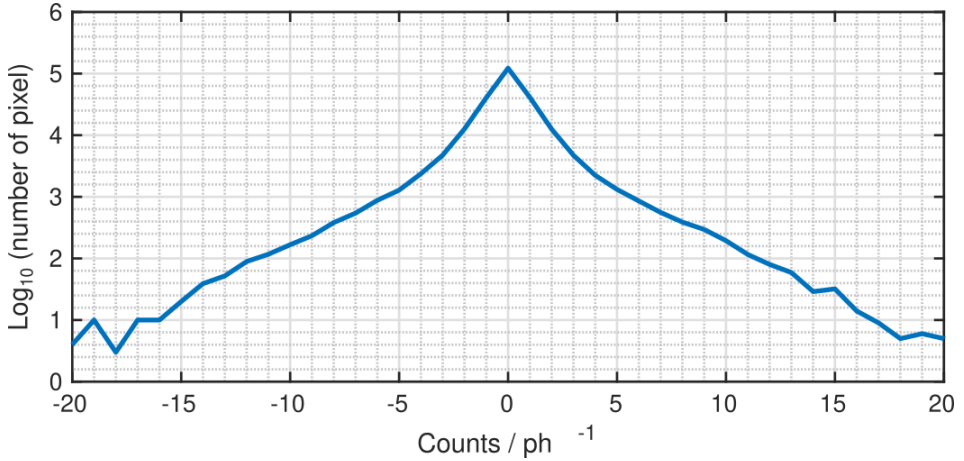


Fig. 5.4: (caption previous page)

signal ranges from  $-20$  ph to  $20$  ph with a symmetrical behavior around the zero. This indicates that the measured coherent scattering signal can not be distinguished from noise of the X-ray illumination in that area.



**Fig. 5.5:** The histogram of the difference of object image and empty beam image (red marked area in 5.4 c)) ranges from  $-20$  to  $20$  photons. The fact that the histogram is symmetrical centered at zero indicates that the coherent scattering signal (CDI signal) can not be distinguished from noise of the X-ray illumination in the selected image area.

**CTF phase reconstruction** The conventional *GINIX* workflow for holotomography data sets is applied to the tomographic scan of the 3D spiral acquired with the EIGER 4M detector. The results are summarized in Fig. 5.6. Since the area of the X-ray illumination is approximately  $500 \text{ px} \times 500 \text{ px}$  of the raw image, each hologram is cropped to this area (same area as marked in Fig. 5.4 a)). Such a cropped hologram is shown in Fig. 5.6 a). While the sample structure is recognisable in the centre of the image, the signal decreases towards the corners of the hologram, recognisable by the increased photon noise. The phase reconstruction via the CTF-approach (Ch. 2.2.3) is performed on each hologram with the reconstruction parameters  $lim1 = 0.0004$ ,  $lim2 = 0.05$ ,  $\frac{\beta}{\delta} = 1/1250$  and a negativity constraint on the phase  $\Phi_{max} = 0$ . The reconstructed phase is presented in Fig. 5.6 b). Since the phase reconstruction results in artifacts at the noisy corners, the image is faded out towards the corners. After the phase reconstruction of each hologram, an inverse radon transform is performed via filtered backprojection. An exemplary reconstructed xy-slice is shown in Fig. 5.6 c). The spiral shape of the object is recognisable. However, the reconstruction is flawed

by phase retrieval artifacts in form of remaining fringes between the spokes and background variations of low spatial frequencies. A histogram of the red rectangle yields the reconstructed phase shifts per voxel. The histogram peak at  $\Phi/vx = -9 \text{ mrad vx}^{-1}$  represents the object, while the peak at  $\Phi/vx = 4 \text{ mrad vx}^{-1}$  represents the background. The difference of  $\Phi/vx = 13 \text{ mrad vx}^{-1}$  between the peaks is in the order of the expected phase shifts of:

$$\Delta\Phi_{theo} = -\delta \cdot k \cdot z = -1.38 \times 10^{-6} \frac{2\pi}{8.98 \times 10^{-11} \text{ m}} \cdot 1.78 \times 10^{-7} \text{ m} = -18.03 \text{ mrad.}$$

The 3D resolution is estimated by an edge profile along the marked red line. Figure 5.6 e) shows the obtained profile. The error function fit with

$$f(x) = a \cdot \left( 1 + \operatorname{erf} \left( \frac{x - x_0}{\sigma \cdot \sqrt{2}} \right) \right) + b$$

yields a half width at half maximum resolution, which is the same as the half-period resolution [Bar13], of  $HWHM = 241.9 \text{ nm}$ . This corresponds to a half-period resolution of 1.3 px.

**Upsampling** The sampling or effective pixel size of the CTF reconstruction is given by the geometrical magnification and physical detector pixel size. The SrH allows for better sampling of the object, based on the NA of the detected signal. In order to use the CTF reconstruction as the initial guess for the SrH-approach the CTF reconstruction has to be interpolated with the corresponding pixel size and FOV.

As described in the reconstruction scheme in section 5.3, the illumination function is reconstructed in the waveguide plane first. The effective pixel size in the waveguide plane  $px_{WG}$  of the far-field propagation is given by the smallest resolution element and is therefore determined by the size of the detectors FOV  $D$ , the wavelength  $\lambda$  and the propagation distance  $z_{02}$ :

$$px_{WG} = \frac{\lambda \cdot z_{02}}{D} = \frac{\lambda \cdot z_{02}}{N_p \cdot px}.$$

The subsequent Fresnel propagation from the waveguide plane to the sample plane

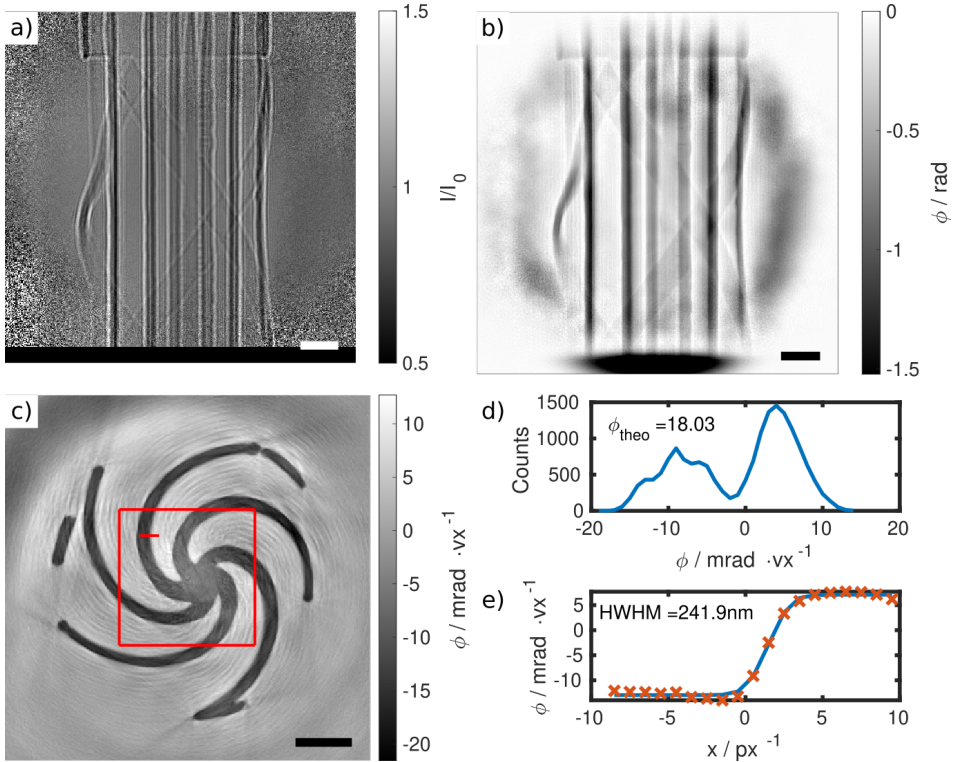


**Fig. 5.6:** Reconstruction of the object phase shifts  $\phi$  via the CTF approach. a) Shows an area of  $500 \text{ px} \times 500 \text{ px}$  of the empty beam corrected hologram. The pixel size due to the geometrical magnification of  $M = 401.6$  is  $186.8 \text{ nm}$ . b) The phase distribution  $\phi$  of the hologram from a) was reconstructed via the CTF approach with the application of a negativity constraint. c) Shows an exemplary  $xy$ -slice of the reconstructed 3D volume obtained by filtered back projection of the reconstructed phase distributions. d) The histogram of the red marked area in c) divides into two values corresponding to air ( $\Phi = 4 \text{ mrad vx}^{-1}$ ) and the object ( $\Phi = -9 \text{ mrad vx}^{-1}$ ). The theoretical phase shift is  $18.03 \text{ mrad vx}^{-1}$ . e) The fit of an error function at the edge of the object (red line in c) with the thickness) results in a resolution of  $240 \text{ nm}$ . This corresponds to a half-period period resolution of  $1.3 \text{ px}$ . Scale bars are  $10 \mu\text{m}$  in the object plane.

leaves the pixel size unchanged  $px_{WG} = px_{SF}$  (Sample F). Thus, for the selected detector FOV of  $D = 500$  px the resulting pixel size in the object plane is  $px_{SF} = 12$  nm. In comparison, the pixel size of the CTF reconstruction is  $px_{eff} = 187$  nm. To extend the FOV in the object plane of the SrH reconstruction, the signal in the detector plane can be upsampled by a pixel interpolation. The upsampling factor is given by  $\alpha = \frac{dx_{eff}}{px_{SF}}$ , which causes the FOV of both reconstructions to match in the object plane. Furthermore, to also match sampling rate of both reconstructions, the CTF reconstruction is upsampled by the factor  $\alpha$  as well.

In the case of  $D = 500$  px the resulting upsampling factor is  $\alpha_{500px} = 15.3$ . To this end, the detector image as well as the initial CTF reconstruction image are upsampled from  $500$  px  $\times$   $500$  px to  $7643$  px  $\times$   $7643$  px. Figure 5.7 compares the tomographic reconstructions of the initial 500 px-CTF phase reconstructions with the tomographic reconstructions of the upsampled CTF phase reconstructions. Integrated line profiles of both reconstructions are determined at the same spoke-to-air transition position as marked by the red line in Fig. 5.6 c). The corresponding areas are shown in Fig.5.7 a) and b), respectively. The line profiles of the two tomographic reconstructions are almost identical, but differ in sampling. As expected, the upsampling of the CTF reconstructions has no influence on the 3D resolution.

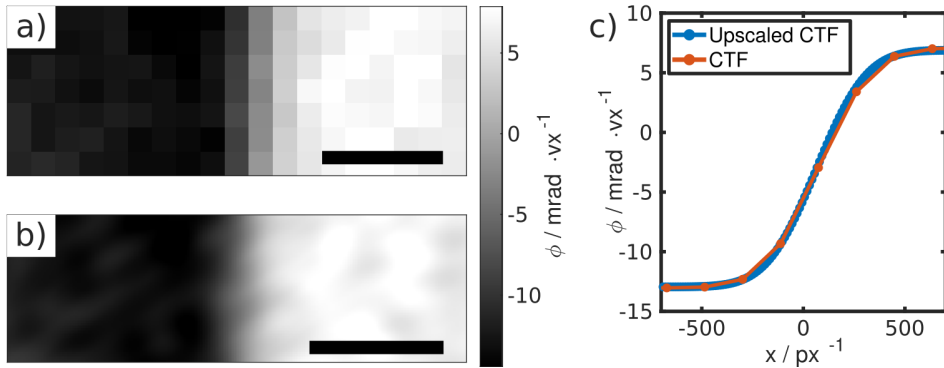


**Fig. 5.7:** Comparison of the original and the upsampled the CTF reconstruction on the spoke-to-air transition of the tomographic reconstruction. The integrated line profile is the same as shown in Fig. 5.6. a) The area of the line profile obtained by the original CTF reconstruction. b) The area of the line profile obtained by the upsampled CTF reconstruction. c) The line profiles of both reconstructions show the same behavior. Scale bars: 1  $\mu$ m.

**SrH reconstruction** The SrH-approach to reconstruct the phase of the object  $\Phi_{SrH}$  requires the prior reconstruction of the complex probe wavefield  $P$ . The wavefield  $P$  is obtained by the iterative reconstruction scheme presented in Ch. 5.3. 100 iterations and a waveguide exit support constraint of a  $1\ \mu\text{m}$  circular aperture are applied. The modulus of the reconstructed wavefield in the exit plane of the waveguide  $P_{wg}$  is shown in Fig. 5.8 a) on a logarithmic scale. The inner circular  $100\ \text{nm}$  contain 72 % of the total intensity. This wavefield is propagated into the object plane at  $x_{obj} = 12.7\ \text{mm}$  via Fresnel propagation. The modulus of  $P_{obj}$  is shown in Fig. 5.8 b). It has the same shape as the measured empty image with scaled intensities.

The inputs for the SrH phase reconstruction of the object transmission function  $O$  are the wavefield  $P_{obj}$ , the upsampled detector holograms  $\sqrt{I_{up}}$  and the upsampled CTF phase reconstructions of the object  $\Phi_{CTF,up}$ , which acts as the initial phase guess. An exemplary image is shown in Fig. 5.8 c). With the aforementioned iterative reconstruction scheme, the reconstructed object phase  $\Phi_{SrH}$  is obtained after 1000 iteration steps and is depicted in Fig. 5.8 d). Horizontal line profiles of both reconstructions at central image height are compared in Fig. 5.8 e). The largest changes of the reconstructed phase shifts occur at the highest absolute phase shifts. Here, the SrH algorithm reconstructs slightly larger phase shifts compared to the CTF reconstruction. In addition, residual vertical interference fringes of the CTF reconstruction are corrected by the SrH algorithm.

Next, the tomographic reconstructions of the CTF and the SrH phase reconstructions are compared, as illustrated in Fig. 5.9 a). The CTF reconstruction shows fringe artifacts between the spokes as well as larger spoke widths compared to the SrH reconstruction. The edge profiles at the red marked area is plotted in Fig. 5.9 b). The spoke-to-air transition is  $\text{HWHM} = 229\ \text{nm}$  for the CTF and  $\text{HWHM} = 120.6\ \text{nm}$  for the SrH reconstruction obtained by an error fit of the profiles. To this end, the 3D resolution is increased by a factor of  $\sim 2$ , due to the novel phase reconstruction scheme.

In addition, a  $\text{HWHM} = 120.6\ \text{nm}$  is smaller than the effective pixel size of  $186.8\ \text{nm}$  of the equivalent parallel beam geometry. Since this is a sub-pixel resolution compared the standard in-line holography approach (equivalent parallel beam geometry), the new reconstruction approach is named **Super-resolution in-line Holography (SrH)**. The key difference of the SrH approach to obtain the sub-pixel resolution is the propagation of a larger field of view via Fourier transform, which results in smaller effective pixel sizes  $p_{SrH} = 12\ \text{nm}$  compared to the equivalent parallel beam geometry and a higher resolution. A 3D rendering of the spiral test pattern is illustrated in Fig. 5.9 c).



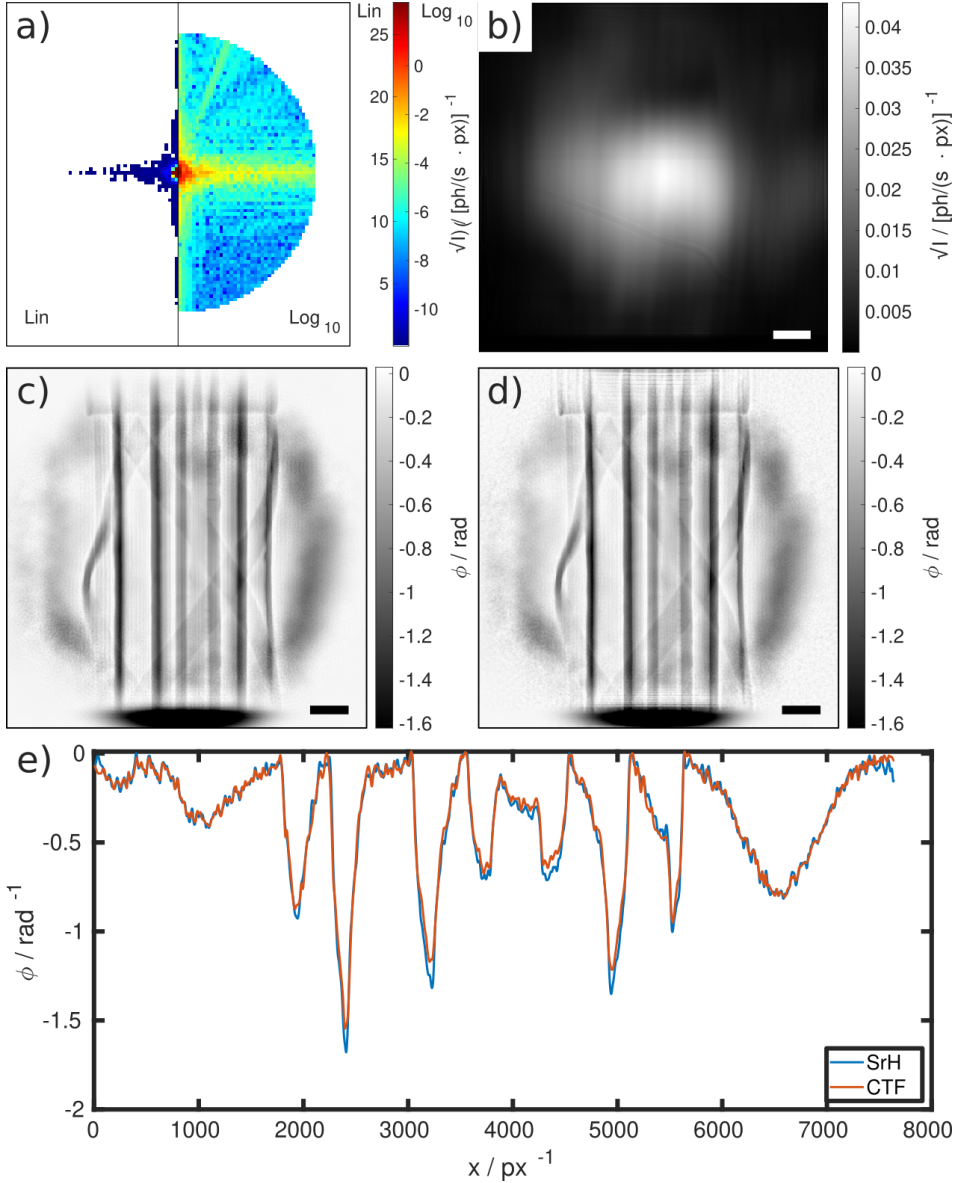


**Fig. 5.8:** Results of the SrH phase reconstruction scheme. a) The modulus of the reconstructed probe wavefield  $|\psi_{probe}(x_{wg})|$  shows the intensity distribution in the waveguide exit plane after 100 iterations. b) The modulus of the near-field propagated wavefield  $|\psi_{probe}(x_{obj})|$  is shown in the object plane. c) The initial guess for the SrH scheme, which is given by the CTF reconstruction  $\Phi_{CTF}$ , is presented. d) Shows the phase reconstruction via SrH-approach  $\Phi_{SrH}$  after 1000 iterations. e) The comparison of the intensity profile of the central horizontal line depicts the differences of the two phase reconstructions. Scale bars: a) 20 nm, b), c), and d)  $10 \mu\text{m}$ .

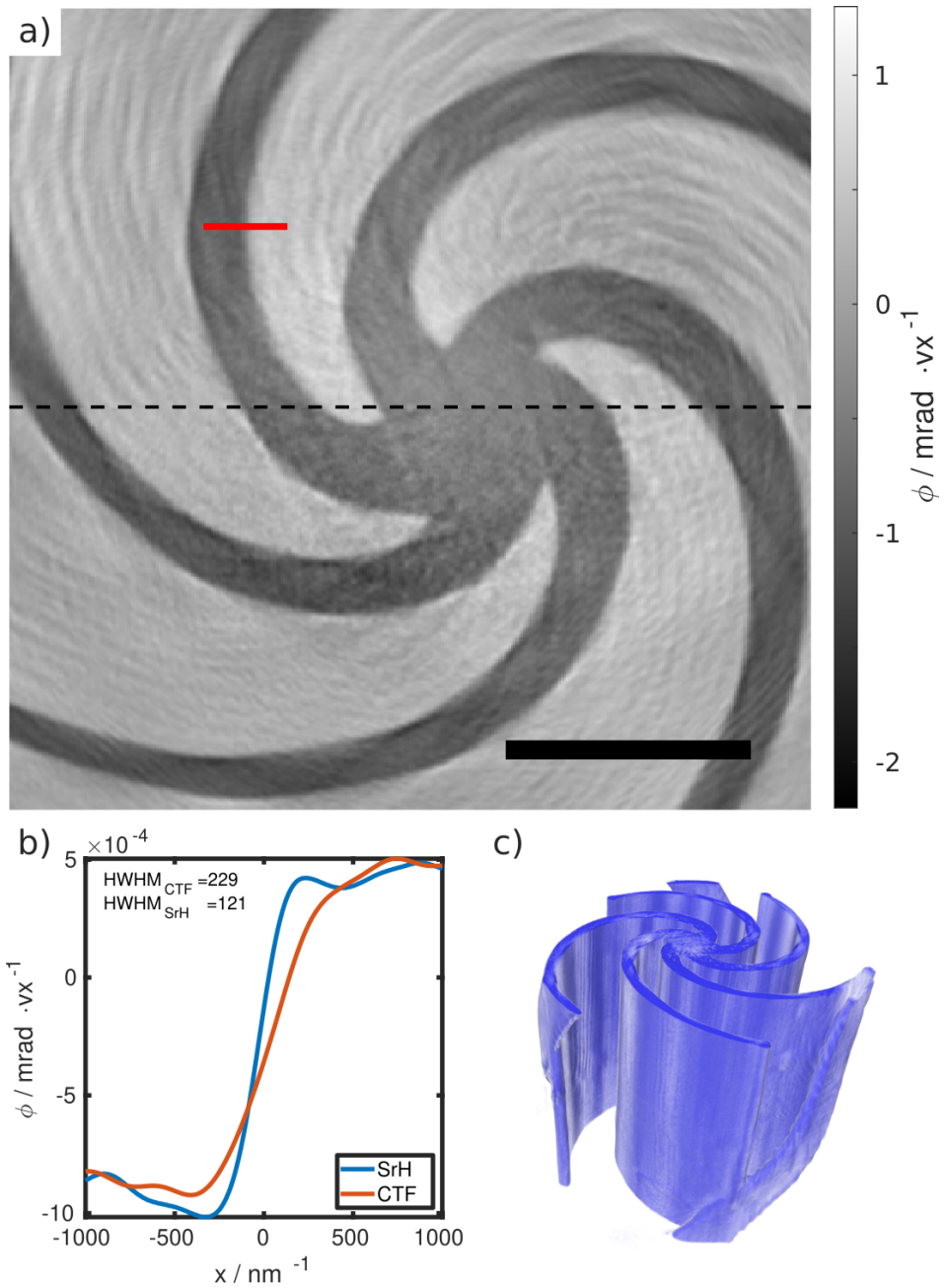


**Fig. 5.9:** (caption next page)

**Fig. 5.9 (previous page):** 3D resolution comparison of the CTF and the SrH phase reconstructions. a) Top: Zoom into the xy-slice of the tomographic reconstruction obtained from the CTF phase reconstructions. Bottom: Zoom into the same xy-slice obtained from the SrH phase reconstructions. The SrH reconstruction shows less fringe artifacts between the spokes. b) The 3D resolution of both reconstructions is determined by an error fit of the intensity profiles, which are marked by the red area in a). The half width at half maximum of the SrH approach is by a factor  $\sim 2$  smaller than the CTF approach. c) 3D rendering of the reconstructed 3D spiral. The scale bar is  $10 \mu\text{m}$ .

**Comparison of reconstruction quality** The difference image of the forward propagated phase solution  $A_{prop}$  and the square root of the measured intensity  $A_{meas}$  is calculated to check the consistency of the reconstructed phases, as illustrated in Fig. 5.10. Major interference residuals of the object are visible in the case of the CTF phase reconstruction. The propagated SrH reconstruction is in a better agreement with the measurement in the central part, where the beam intensity is the highest. Towards the edges the reconstruction fails. Figure 5.10 c) shows the following error metric of the reconstruction scheme:

$$E(i) = \frac{|(|\mathcal{F}(P \cdot O(i))|^2 - I)|^2}{N_y \cdot N_z}$$

The error metric shows a converging behavior for 1000 iterations.

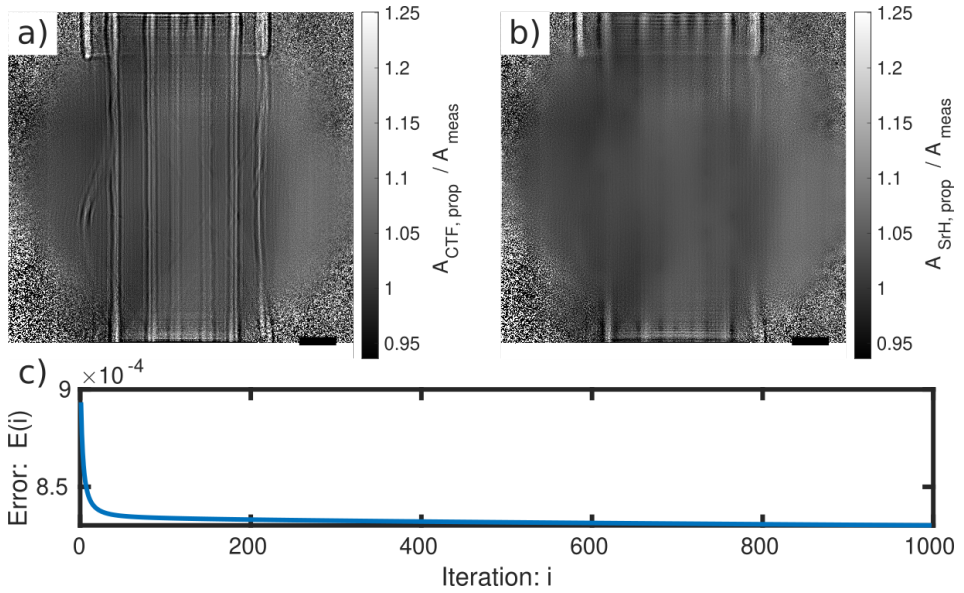


**Fig. 5.10:** Comparison of the quality of the reconstructed phases by the CTF and the SrH approach. a) The amplitude of the forward propagated CTF phase reconstruction  $A_{CTF,prop}$  is divided by the square root of the measured hologram  $A_{meas}$ . The object does not cancel out well. b) The amplitude of the forward propagated SrH phase reconstruction ( $i = 1000$ )  $A_{SrH,prop}$  is divided by the square root of the measured hologram  $A_{meas}$ . The object cancel out well in the center. The reconstruction become worse towards the illumination borders. c) The error metric of the SrH iterations  $E(i) = \frac{[|\mathcal{F}(P \cdot O(i))|^2 - I]^2}{N_y \cdot N_z}$  shows a converging behavior for  $i = 1000$ . Scale bars are  $10 \mu\text{m}$  in the detection plane.

## 5.5 Discussion and Outlook

A new test pattern in the form of a 3D spiral is designed and manufactured to determine the 3D resolution of the novel **Super-resolution in-line Holography (SrH)** phase retrieval approach and the routinely used CTF approach. Instead of a scintillation-based detector, the large area photon counting detector Eiger 4M is used to increase the numerical aperture of the imaging system. The complex probe wavefield is reconstructed by a single empty beam acquisition via an iterative reconstruction scheme based on alternating projections. This allows for an empty beam division in the object plane, rather than in the detection plane. The high X-ray sensitivity of the Eiger 4M enables the possibility to detect weak signals such as the CDI signal of the object. After phase retrieval of the images and subsequent tomographic reconstruction, the 3D resolution is determined by error function fits at the object-to-air transition. The 3D resolution of the SrH approach is approximately twice as high (HWHM = 120.6 nm) as that of the CTF reconstruction (HWHM = 229 nm). This is attributed to the far-field treatment of the object transmission function, which provides smaller effective pixel sizes than the equivalent parallel beam geometry assumed in the CTF approach, the larger field of view and the usage of the waveguide illumination tails. In fact, the resolution of the SrH approach is higher than the effective pixel size of 186.8 nm > 120.6 nm of the CTF approach, resulting in a super-resolution compared to the standard in-line holography CTF-based approach. Furthermore, a refractive object approach is applied, which allows for the reconstruction of phase shifts larger than  $2\pi$  without phase wrapping.

In the presented proof-of-principle experiment, the coherent scattered signal beyond the waveguide illumination is weak. A FOV larger than the selected 500 px  $\times$  500 px does not contain any further information and therefore does not increase the 3D resolution. Besides, the determination of the 3D resolution is limited by the actual steepness of the edge of the test object. A more elaborate method of determining resolution would be to use a 3D spiral with narrowing spokes as the equivalent of a 2D siemens star. Currently, the manufacture of such small spokes is a challenge for the used method of laser lithography of polymer material. In addition, 3D resolution is affected by tomographic reconstruction. For example, positional inaccuracies of the tomographic rotation axis at different acquisition angles reduce resolution, especially at these small scales. Furthermore, the quality of tomographic reconstruction can be improved by increasing the number of tomographic angles.

This proof-of-concept experiment demonstrates the potential of the SrH approach for 3D imaging. Further steps would be to verify the actual 3D resolution limit of this

approach at the GINIX setup. A smaller distance between source and sample, the switch to lower X-ray energies and longer acquisition times could result in a more intense coherent diffracted signal. With the planned upgrade of the PETRA III storage ring to a diffraction-limited PETRA IV storage ring, the higher intensity provided could be helpful for the coherent diffraction signal as well. Furthermore, a 3D support constraints can be considered for compact objects. Currently, the reconstruction scheme works with the upsampled pixel sizes in the detector plane. A more accurate reconstruction method would consider the actual pixel size in the detector plane instead of the upsampled pixel sizes. The reconstruction scheme should also benefit from acquisitions at several propagation distances. Another important step is the application to biological samples. In general, they are not compact objects and the effect of region-of-interest tomography becomes relevant.

## Conclusion and Outlook

---

# 6

In this work the holotomography setup of the synchrotron endstation GINIX was extended to a **multi-scale** X-ray phase-contrast tomography setup suitable for **3D virtual histology** by adding two acquisition schemes. The first additional scheme is **Scale I** of the multi-scale approach, which enlarges the reconstructed 3D volumes by a factor of  $\sim 64$  at  $\frac{1}{30}$ th of the acquisition time compared to the existing holotomography setup. To this end, the larger sized and more intense parallel X-ray beam is used. The already established X-ray waveguide-based configuration is referred to as **Scale II**. The second additional scheme is **Scale III** of the multi-scale approach, which aims for the highest resolution. It is based on a novel acquisition and reconstruction scheme, which is enabled by using a single photon counting detector with a large FOV instead of a high-resolution scintillation-based detector.

The propagation-based X-ray phase-contrast tomography of **Scale I** or else the parallel beam (PB) setup is a powerful imaging scheme, which is known to provide excellent reconstructions of unstained biological tissue and is an established imaging technique at several synchrotron beamlines, e.g. TOMCAT [Bor+21], ID19 [Cho+22b] or ANATOMIX [Rod+21]. Such a microtomography configuration complements and improves the 3D virtual histology capability of the GINIX endstation by its larger reconstruction volume of  $1.6 \text{ mm} \times 1.6 \text{ mm} \times 1.4 \text{ mm}$  or more by stitching several tomograms. This additional scale complements 3D virtual histology at the GINIX by enabling the investigation of tissue morphologies such as the tissue parenchyma on larger scales with the possibility of investigations at sub-cellular resolution by the waveguide-based setup. Chapter 3 describes the implementation and commissioning of the PB setup. The characterisation of biological tissue imaged by this setup is demonstrated on the examples of pancreatic tumorous human tissue and Covid-19 affected human lung tissue. An Islet of Langerhans, which is a distinctive feature within the pancreas, and its inner cells are visualized. The calculation of an 3D anisotropy parameter of the reconstructed volume showcases the potential to support the classification of tumorous pancreatic tissue into different stages. The example for another tissue-specific 3D metric is presented for the Covid-19 tissue. In this case, the air-to-tissue

distance was calculated for each voxel. A larger mean distance of the reconstructed volume leads to the assumption of a reduced oxygen-to-blood transport. Furthermore, a direct comparison of a conventional *H&E* histology image and a virtual histology image is presented and discussed. The reconstruction volume can be increased by acquiring multiple side-by-side tomograms with overlapping FOVs followed by the subsequent stitching of the individual tomograms.

Chapter 4 describes the improvements on **Scale II**, the X-ray waveguide-based holotomography setup. New designed silicon and germanium X-ray waveguides are presented. The silicon waveguide offers long beam stabilities at an X-ray energy of 8 keV. The germanium waveguide shows great potential in terms of X-ray beam intensity at 13.8 keV. However, the intensity decreases drastically over the course of a few hours of illumination due to structural changes. At the current stage of development, the germanium waveguide is not suitable for routine operation. A new scintillation-based X-ray detector is commissioned and implemented as the new standard detector in this configuration. In this context a pixel response map of the detector was calculated, which separates the actual shape of the X-ray illumination function from the grained structure of the Gadox scintillator. More importantly it reduces ring artifacts in the tomographic reconstruction caused by stationary false pixel responses. This setup was used to investigate the blood vessel splitting of micrometer thick capillaries of Covid-19 affected human lung tissue.

In addition to this two scales, a novel acquisition and reconstruction scheme for high resolution tomographic acquisitions (**Scale III**) is presented. In a proof-of-concept experiment, which is based on the work of Soltau et al. [Sol+21], the potential for high resolutions of the novel super-resolution in-line holography (SRH) approach is demonstrated in 3D on a custom designed test pattern in form of a 3D spiral. The reconstruction scheme of Soltau [Sol+21] is extended by its application to 3D imaging using tomographic acquisitions. Furthermore, an object extraction step is introduced to apply constraints to the object transmission function e.g. homogeneous object. The 3D resolution power of the SRH-approach was determined by the error function fit of an object edge. It resulted in a sub-pixel resolution of 120 nm and therefore super-resolution compared to the standard approach of an equivalent parallel beam geometry, which provides an effective pixel size of 180 nm. However, the determined 3D half-period resolution of 120 nm at an effective pixel size of 12 nm leaves room for further resolution improvements.

This work presents an imaging instrument with the capability of multi-scale 3D virtual



---

histology. However, to realise the full potential of this multi-scale approach an improved workflow is required. This includes an uncomplicated reconstruction pipeline for all three scales, e.g. in the form of a dedicated user interface with a few parameter settings and reconstruction previews. On the fly reconstructions of Scale 1 enable the possibility to select an area of interest for the Scale 2 scan. With an improved and automated switch routine between Scale 1 and Scale 2, a follow up scan of the selected area can be performed at a higher resolution. The object size and possible region-of-interest tomography issues, such as a weak X-ray signal, need to be considered. An equivalent selection and switch from Scale 2 to Scale 3 is conceivable. In addition to an optimized acquisition and reconstruction workflow, each scale offers room for improvements. A major upgrade for Scale 1 would be a sophisticated acquisition pattern of individual adjacent tomograms with a subsequent reconstruction that stitches accordingly. The next improvement step for Scale 2 is the reduction of waveguide motion drifts to ensure a more static X-ray illumination. The switch from a *step and shoot* to a *continuous* tomographic acquisition scheme would lead to a reduced total scanning time. For Scale 3, the application to biomedical samples and further improvements in 3D resolution by refined acquisition parameters are important next steps. For all three scales local tomography artifacts can become an issue and should be considered. One concern for high resolution scans is the lateral motion of the rotation axis during a tomographic scan. A separate control of the rotation axis e.g. by an interferometer can help. Up to now, a simple but meaningful presentation of the 3D data is challenging. The segmentation of characteristic object features is an effective approach. However, image segmentation can be arbitrarily complex and is the subject of current research [Ram+21]. The presented work with the resulting schemes shows interesting candidates for potential beamline applications and endstations for the planned upgrade of the *PETRA III* into a diffraction-limited storage ring (*PETRA IV*).

So far, the combination of Scale 1 and Scale 2 for 3D virtual histology has been demonstrated on tumorous pancreatic tissue [Fro+20a] and Covid-19 affected lung tissue [Eck+20]. This allows the 3D quantification of the tissue morphology, e.g. the parenchym, as well as the 3D quantification at a cellular level, e.g. 3D cell shapes. It is expected that the application of Scale 3 to 3D virtual histology provides further insights into the 3D substructure of cells within the tissue. The obtained 3D information can support conventional histology, which is more specific to the biomolecular origin of the structures due to special staining. Note that each chapter contains its own detailed discussion.



# Appendix

# A

## A.1 Zyla scintillator exchange

It is recommended to (dis-) assemble the Zyla in a cleanroom:

1. Clean the scintillator-FOP and the sensor-FOP with optical tissues and isopropyl alcohol
2. Put the O-ring around the sensor-FOP and a drop of glycerol onto the sensor-FOP in order to ensure a good optical transmission
3. Put the scintillator-FOP against the sensor-FOP (scintillation layer faces towards the X-rays)
4. Put the beryllium-scintillator-adapter onto the scintillator
5. Fix the adapter by 4 screws and tighten it lightly crossed-wise
6. Put the beryllium filter onto the beryllium-scintillator-adapter
7. Put the cover plate-beryllium-adapter onto the beryllium filter
8. Fix the adapter by 4 screws and tighten it lightly crossed-wise

Figure A.1 shows the sCMOS sensor of the disassembled camera on the left and the front side of the scintillation unit on the right.

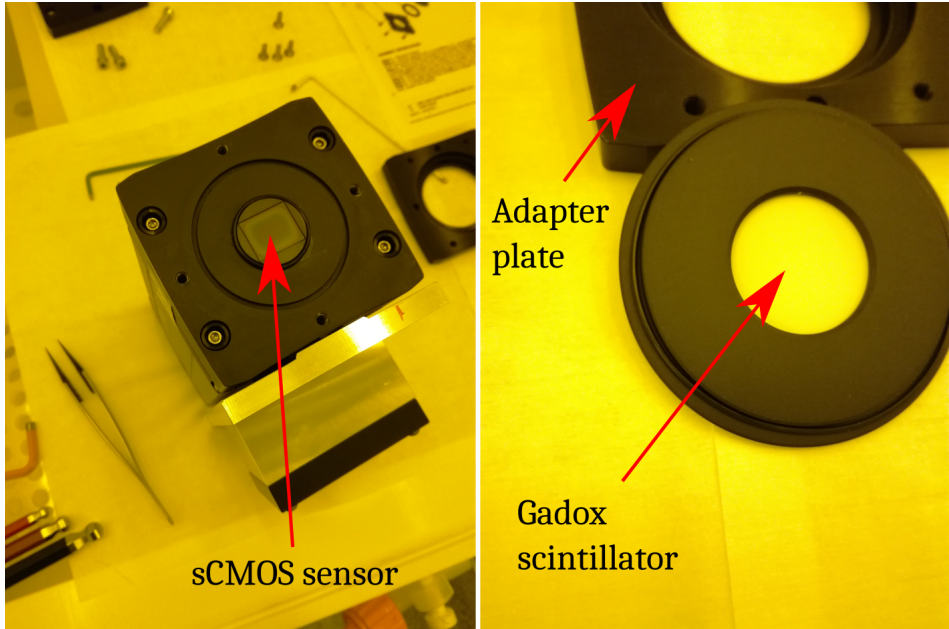


**Fig. A.1:** Left: Disassembled Zyla camera reveals the sCMOS sensor. Right: Gadox scintillation unit and adapter plate.

## A.2 Derivation of the modified ePIE

The derivation is based on [MJL17] and [Wit20]. The updated wavefield  $\psi'$  can be divided by the probe wavefield  $P$  to retrieve the updated object transmission function  $O'$ .

$$O' = \frac{\psi'}{P} = \frac{\psi' \cdot P^*}{|P|^2}$$

However, this fails for areas of low intensity (photon counts). The idea is to update bright areas of the probe wavefield  $P$ , while keeping the object  $O$  at dim areas of the probe wavefield. This is realised by the introduction of a weighting factor  $\omega$ :

$$\begin{aligned} O' &= (1 - \omega) \cdot O + \omega \cdot \frac{\psi' \cdot P^*}{|P|^2} \\ &= O + \omega \cdot \frac{P^* \cdot (\psi' - \psi)}{|P|^2} \end{aligned}$$

With  $\omega = \alpha \cdot |P|^2 / |P|_{max}^2$ , this leads to the ePIE update step:

$$O' = O + \alpha \cdot \frac{P^*}{|P|_{max}^2} \cdot (\psi' - \psi)$$

By replacing the object wavefield with an exponential wavefield of the refractive object  $O = e^{i\tilde{O}}$ , this update step changes. The change is derived from the perspective of a minimization problem. Consider the error metric :

$$E^{obj} = |P \cdot e^{i\tilde{O}} - \psi'|^2$$

The gradient of the error metric with respect to  $\tilde{O}$  is:

$$\nabla_{\tilde{O}} E^{obj} = 2 \cdot (iPe^{i\tilde{O}})^* (Pe^{i\tilde{O}} - \psi')$$

The error metric is reduced by moving in the negative gradient direction:

$$\begin{aligned} \tilde{O}' &= \tilde{O} - \frac{\gamma}{2} \nabla_{\tilde{O}} E^{obj} = \tilde{O} + \gamma (iPe^{i\tilde{O}})^* (\psi' - Pe^{i\tilde{O}}) \\ &= \tilde{O} + \alpha \cdot \frac{(iPe^{i\tilde{O}})^*}{|Pe^{i\tilde{O}}|_{max}^2} \cdot (\psi' - Pe^{i\tilde{O}}) \\ &= \tilde{O} - \alpha \cdot \frac{i \cdot \psi^*}{|\psi|_{max}^2} \cdot (\psi' - \psi) \end{aligned}$$

with  $\gamma = \alpha / |\psi|_{max}^2$ .

### A.3 Silicon waveguide

The internal name of the presented silicon waveguide is **P200L-01**, which was introduced at the end of run89. The presented beam stability results from measurements in run90. Furthermore, the waveguide was used in run94. Figure A.2 shows the unmounted waveguide (top) and the mounted waveguide (bottom).

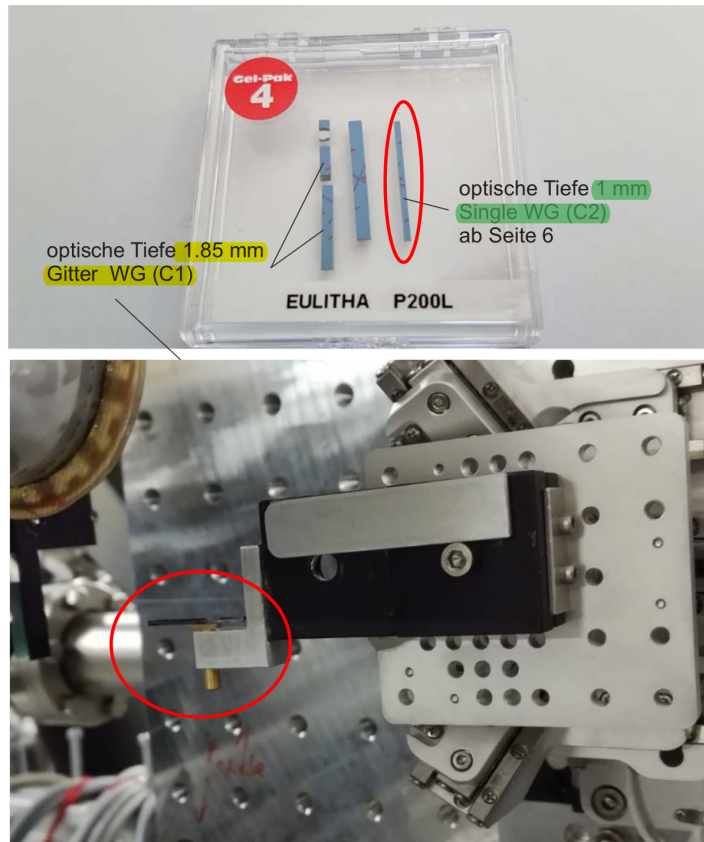


**Fig. A.2:** Top: Unmounted silicon waveguide **P200L-01** with 1 mm optical depth and channels with 100 nm diameter. Bottom: The waveguide is mounted onto the hexapod.

# Bibliography

---

- [Abb+08] B. Abbey, K. A. Nugent, G. J. Williams, J. N. Clark, A. G. Peele, M. A. Pfeifer, M. De Jonge, and I. McNulty. “Keyhole coherent diffractive imaging.” In: *Nature Physics* 4.5 (2008), pp. 394–398.
- [Ack+20] M. Ackermann, S. E. Verleden, M. Kuehnel, A. Haverich, T. Welte, F. Laenger, A. Vanstapel, C. Werlein, H. Stark, A. Tzankov, et al. “Pulmonary vascular endothelialitis, thrombosis, and angiogenesis in Covid-19.” In: *New England Journal of Medicine* 383.2 (2020), pp. 120–128.
- [Alb+18] J. Albers, S. Pacilé, M. A. Markus, M. Wiart, G. Vande Velde, G. Tromba, and C. Dullin. “X-ray-based 3D virtual histology—Adding the next dimension to histological analysis.” In: *Molecular Imaging and Biology* 20.5 (2018), pp. 732–741.
- [Alb+21] J. Albers, A. Svetlove, J. Alves, A. Kraupner, F. di Lillo, M. A. Markus, G. Tromba, F. Alves, and C. Dullin. “Elastic transformation of histological slices allows precise co-registration with microCT data sets for a refined virtual histology approach.” In: *Scientific reports* 11.1 (2021), pp. 1–13.
- [AM11] J. Als-Nielsen and D. McMorrow. *Elements of modern X-ray physics*. John Wiley & Sons, 2011.
- [Amu+13] K. Amunts, C. Lepage, L. Borgeat, H. Mohlberg, T. Dickscheid, M.-É. Rousseau, S. Bludau, P.-L. Bazin, L. B. Lewis, A.-M. Oros-Peusquens, et al. “BigBrain: an ultrahigh-resolution 3D human brain model.” In: *Science* 340.6139 (2013), pp. 1472–1475.
- [And17] Andor. *Hardware Guide - Zyla sCMOS*. Version 1.12. 2017.
- [BG08] J. D. Bancroft and M. Gamble. *Theory and practice of histological techniques*. Elsevier health sciences, 2008.

- [Bar+22] G. E. Barbone, A. Bravin, A. Mittone, A. Pacureanu, G. Mascio, P. Di Pietro, M. J. Kraiger, M. Eckermann, M. Romano, M. Hrabě de Angelis, et al. “X-ray multiscale 3D neuroimaging to quantify cellular aging and neurodegeneration postmortem in a model of Alzheimer’s disease.” In: *European Journal of Nuclear Medicine and Molecular Imaging* (2022), pp. 1–20.
- [Bar13] M. Bartels. *Cone-beam X-ray phase contrast tomography of biological samples: optimization of contrast, resolution and field of view*. Vol. 13. Universitätsverlag Göttingen, 2013.
- [Bar+13] M. Bartels, V. H. Hernandez, M. Krenkel, T. Moser, and T. Salditt. “Phase contrast tomography of the mouse cochlea at microfocus x-ray sources.” In: *Applied Physics Letters* 103.8 (2013), p. 083703.
- [Ber+19a] S. Berg, D. Kutra, T. Kroeger, C. N. Straehle, B. X. Kausler, C. Haubold, M. Schiegg, J. Ales, T. Beier, M. Rudy, et al. “Ilastik: interactive machine learning for (bio) image analysis.” In: *Nature methods* 16.12 (2019), pp. 1226–1232.
- [Ber+19b] S. Berg, D. Kutra, T. Kroeger, C. N. Straehle, B. X. Kausler, C. Haubold, M. Schiegg, J. Ales, T. Beier, M. Rudy, K. Eren, J. I. Cervantes, B. Xu, F. Beuttenmueller, A. Wolny, C. Zhang, U. Koethe, F. A. Hamprecht, and A. Kreshuk. “ilastik: interactive machine learning for (bio)image analysis.” In: *Nature Methods* (2019). DOI: 10.1038/s41592-019-0582-9.
- [BWS12] S. Berujon, H. Wang, and K. Sawhney. “X-ray multimodal imaging using a random-phase object.” In: *Physical Review A* 86.6 (2012), p. 063813.
- [Bor+21] E. Borisova, G. Lovric, A. Miettinen, L. Fardin, S. Bayat, A. Larsson, M. Stampanoni, J. C. Schittny, and C. M. Schlepütz. “Micrometer-resolution X-ray tomographic full-volume reconstruction of an intact post-mortem juvenile rat lung.” In: *Histochemistry and cell biology* 155.2 (2021), pp. 215–226.
- [Brä+19] G. Brändén, G. Hammarin, R. Harimoorthy, A. Johansson, D. Arnlund, E. Malmerberg, A. Barty, S. Tångefjord, P. Berntsen, D. P. DePonte, et al. “Coherent diffractive imaging of microtubules using an X-ray laser.” In: *Nature communications* 10.1 (2019), pp. 1–9.



- [Bus+18] M. Busse, M. Müller, M. A. Kimm, S. Ferstl, S. Allner, K. Achterhold, J. Herzen, and F. Pfeiffer. “Three-dimensional virtual histology enabled through cytoplasm-specific X-ray stain for microscopic and nanoscopic computed tomography.” In: *Proceedings of the National Academy of Sciences* 115.10 (2018), pp. 2293–2298.
- [Buz11] T. M. Buzug. “Computed tomography.” In: *Springer handbook of medical technology*. Springer, 2011, pp. 311–342.
- [Cas+11] E. Castelli, M. Tonutti, F. Arfelli, R. Longo, E. Quaia, L. Rigon, D. Sanabor, F. Zanconati, D. Dreossi, A. Abrami, et al. “Mammography with synchrotron radiation: first clinical experience with phase-detection technique.” In: *Radiology* 259.3 (2011), pp. 684–694.
- [Cec+14] A. Cecilia, V. Jary, M. Nikl, E. Mihokova, D. Hänschke, E. Hamann, P.-A. Douissard, A. Rack, T. Martin, B. Krause, et al. “Investigation of the luminescence, crystallographic and spatial resolution properties of LSO: Tb scintillating layers used for X-ray imaging applications.” In: *Radiation measurements* 62 (2014), pp. 28–34.
- [Cha14] J. K. Chan. “The wonderful colors of the hematoxylin–eosin stain in diagnostic surgical pathology.” In: *International journal of surgical pathology* 22.1 (2014), pp. 12–32.
- [CV01] T. F. Chan and L. A. Vese. “Active contours without edges.” In: *IEEE Transactions on image processing* 10.2 (2001), pp. 266–277.
- [Che+17] C. Chen, C. M. Cohrs, J. Stertmann, R. Bozsak, and S. Speier. “Human beta cell mass and function in diabetes: Recent advances in knowledge and technologies to understand disease pathogenesis.” In: *Molecular metabolism* 6.9 (2017), pp. 943–957.
- [Cho+22a] M. Chourrout, H. Rositi, E. Ong, V. Hubert, A. Paccalet, L. Foucault, A. Autret, B. Fayard, C. Olivier, R. Bolbos, et al. “Brain virtual histology with X-ray phase-contrast tomography Part I: whole-brain myelin mapping in white-matter injury models.” In: *Biomedical optics express* 13.3 (2022), pp. 1620–1639.
- [Cho+22b] M. Chourrout, M. Roux, C. Boisvert, C. Gislard, D. Legland, I. Arganda-Carreras, C. Olivier, F. Peyrin, H. Boutin, N. Rama, et al. “Brain virtual histology with X-ray phase-contrast tomography Part II: 3D morphologies

- of amyloid- $\beta$  plaques in Alzheimer's disease models." In: *Biomedical optics express* 13.3 (2022), pp. 1640–1653.
- [Chu+20] M. Chung, A. Bernheim, X. Mei, N. Zhang, M. Huang, X. Zeng, J. Cui, W. Xu, Y. Yang, Z. A. Fayad, et al. "CT imaging features of 2019 novel coronavirus (2019-nCoV)." In: *Radiology* (2020).
- [Cle+11] J. O. Cleary, M. Modat, F. C. Norris, A. N. Price, S. A. Jayakody, J. P. Martinez-Barbera, N. D. Greene, D. J. Hawkes, R. J. Ordidge, P. J. Scambler, et al. "Magnetic resonance virtual histology for embryos: 3D atlases for automated high-throughput phenotyping." In: *Neuroimage* 54.2 (2011), pp. 769–778.
- [Clo+96] P. Cloetens, R. Barrett, J. Baruchel, J.-P. Guigay, and M. Schlenker. "Phase objects in synchrotron radiation hard x-ray imaging." In: *Journal of physics D: applied physics* 29.1 (1996), p. 133.
- [Clo+99] P. Cloetens, W. Ludwig, J. Baruchel, D. Van Dyck, J. Van Landuyt, J. Guigay, and M. Schlenker. "Holotomography: Quantitative phase tomography with micrometer resolution using hard synchrotron radiation x rays." In: *Applied physics letters* 75.19 (1999), pp. 2912–2914.
- [CCJ41] A. H. Coons, H. J. Creech, and R. N. Jones. "Immunological properties of an antibody containing a fluorescent group." In: *Proceedings of the society for experimental biology and medicine* 47.2 (1941), pp. 200–202.
- [Cro+19] L. C. Croton, G. Ruben, K. S. Morgan, D. M. Paganin, and M. J. Kitchen. "Ring artifact suppression in X-ray computed tomography using a simple, pixel-wise response correction." In: *Optics express* 27.10 (2019), pp. 14231–14245.
- [Cul13] C. F. A. Culling. *Handbook of histopathological and histochemical techniques: including museum techniques*. Butterworth-Heinemann, 2013.
- [CXR] CXRO. *The Center for X-ray Optics*. [http://cxro.lbl.gov/optical\\_constants](http://cxro.lbl.gov/optical_constants). [Online; accessed 31-March-2022].
- [Dav+02] C. David, B. Nöhammer, H. Solak, and E. Ziegler. "Differential x-ray phase contrast imaging using a shearing interferometer." In: *Applied physics letters* 81.17 (2002), pp. 3287–3289.
- [Dav+11] V. Davidoiu, B. Sixou, M. Langer, and F. Peyrin. "Non-linear iterative phase retrieval based on Frechet derivative." In: *Opt. Express* 19.23 (2011), pp. 22809–22819. DOI: 10.1364/OE.19.022809.

- [Die+10] M. Dierolf, A. Menzel, P. Thibault, P. Schneider, C. M. Kewish, R. Wepf, O. Bunk, and F. Pfeiffer. “Ptychographic X-ray computed tomography at the nanoscale.” In: *Nature* 467.7314 (2010), pp. 436–439.
- [Doe+14] T. R. Doeppner, B. Kaltwasser, M. Bähr, and D. M. Hermann. “Effects of neural progenitor cells on post-stroke neurological impairment—a detailed and comprehensive analysis of behavioral tests.” In: *Frontiers in cellular neuroscience* 8 (2014), p. 338.
- [Dul+21] C. Dullin, F. di Lillo, A. Svetlove, J. Albers, W. Wagner, A. Markus, N. Sodini, D. Dreossi, F. Alves, and G. Tromba. “Multiscale biomedical imaging at the SYRMEP beamline of Elettra-Closing the gap between preclinical research and patient applications.” In: *Physics Open* 6 (2021), p. 100050.
- [Eck+20] M. Eckermann, J. Frohn, M. Reichardt, M. Osterhoff, M. Sprung, F. Westermeyer, A. Tzankov, C. Werlein, M. Kühnel, D. Jonigk, et al. “3D virtual pathohistology of lung tissue from Covid-19 patients based on phase contrast X-ray tomography.” In: *Elife* 9 (2020), e60408.
- [Eck+21a] M. Eckermann, N. Peruzzi, J. Frohn, M. Bech, E. Englund, B. Veress, T. Salditt, L. B. Dahlin, and B. Ohlsson. “3d phase-contrast nanotomography of unstained human skin biopsies may identify morphological differences in the dermis and epidermis between subjects.” In: *Skin Research and Technology* 27.3 (2021), pp. 316–323.
- [Eck+21b] M. Eckermann, B. Schmitzer, F. van der Meer, J. Franz, O. Hansen, C. Stadelmann, and T. Salditt. “Three-dimensional virtual histology of the human hippocampus based on phase-contrast computed tomography.” In: *Proceedings of the National Academy of Sciences* 118.48 (2021), e2113835118.
- [Eck+21c] M. Eckermann, F. Van der Meer, P. Cloetens, T. Ruhwedel, W. Möbius, C. Stadelmann, and T. Salditt. “Three-dimensional virtual histology of the cerebral cortex based on phase-contrast X-ray tomography.” In: *Biomedical optics express* 12.12 (2021), pp. 7582–7598.
- [Fie82] J. R. Fienup. “Phase retrieval algorithms: a comparison.” In: *Applied optics* 21.15 (1982), pp. 2758–2769.

- [Fro+20a] J. Frohn, D. Pinkert-Leetsch, J. Missbach-Güntner, M. Reichardt, M. Osterhoff, F. Alves, and T. Salditt. “3D virtual histology of human pancreatic tissue by multiscale phase-contrast X-ray tomography.” In: *Journal of Synchrotron Radiation* 27.6 (2020), pp. 1707–1719.
- [Fro+20b] J. Frohn, M. Reichardt, M. Eckermann, and T. Salditt. *Propagation-based phase-contrast X-ray tomography of soft tissue with Zyla-HF sCMOS camera at the synchrotron endstation „GINIX“*. <https://qd-europe.com/de/en/product/cameras-for-fiber-coupled-scintillators/>. [Online; accessed 16-September-2022]. 2020.
- [Gab48] D. Gabor. “A new microscopic principle.” In: *nature* 161 (1948), pp. 777–778.
- [Ger72] R. W. Gerchberg. “A practical algorithm for the determination of plane from image and diffraction pictures.” In: *Optik* 35.2 (1972), pp. 237–246.
- [Ger+08] M. Germann, A. Morel, F. Beckmann, A. Andronache, D. Jeanmonod, and B. Müller. “Strain fields in histological slices of brain tissue determined by synchrotron radiation-based micro computed tomography.” In: *Journal of neuroscience methods* 170.1 (2008), pp. 149–155.
- [Gol38] J. Goldner. “A modification of the Masson trichrome technique for routine laboratory purposes.” In: *The American journal of pathology* 14.2 (1938), p. 237.
- [Goo05] J. W. Goodman. “Introduction to Fourier optics.” In: *Introduction to Fourier optics, 3rd ed., by JW Goodman*. Englewood, CO: Roberts & Co. Publishers, 2005 1 (2005).
- [GM08] H. Graafsma and T. Martin. “Detectors for synchrotron tomography.” In: *Advanced tomographic methods in materials research and engineering* (2008), pp. 277–302.
- [Gre82] R. Grella. “Fresnel propagation and diffraction and paraxial wave equation.” In: *Journal of Optics* 13.6 (1982), p. 367. DOI: 10.1088/0150-536X/13/6/006.
- [GTE02] S. M. Gruner, M. W. Tate, and E. F. Eikenberry. “Charge-coupled device area X-ray detectors.” In: *Review of Scientific Instruments* 73.8 (2002), pp. 2815–2842.
- [HE19] L. Haeberle and I. Esposito. “Pathology of pancreatic cancer.” In: *Translational gastroenterology and hepatology* 4 (2019).

- [Hag+14] J. Hagemann, A.-L. Robisch, D. Luke, C. Homann, T. Hohage, P. Cloetens, H. Suhonen, and T. Salditt. “Reconstruction of wave front and object for inline holography from a set of detection planes.” In: *Optics Express* 22.10 (2014), pp. 11552–11569.
- [Häg+17] R. Hägerling, D. Drees, A. Scherzinger, C. Dierkes, S. Martin-Almedina, S. Butz, K. Gordon, M. Schäfers, K. Hinrichs, P. Ostergaard, et al. “VIPAR, a quantitative approach to 3D histopathology applied to lymphatic malformations.” In: *JCI insight* 2.16 (2017).
- [HM22] R. Hägerling and F. Mohr. “Light-Sheet Microscopy as a Novel Tool for Virtual Histology.” In: *Artificial Intelligence Applications In Human Pathology* (2022), p. 21.
- [Hof17] S. Hoffmann-Urlaub. “X-ray waveguide optics. Beyond straight channels.” In: (2017).
- [Hof+16] S. Hoffmann-Urlaub, P. Höhne, M. Kanbach, and T. Salditt. “Advances in fabrication of X-ray waveguides.” In: *Microelectronic Engineering* 164 (2016), pp. 135–138.
- [Hol+14] M. Holler, A. Diaz, M. Guizar-Sicairos, P. Karvinen, E. Färm, E. Härkönen, M. Ritala, A. Menzel, J. Raabe, and O. Bunk. “X-ray ptychographic computed tomography at 16 nm isotropic 3D resolution.” In: *Scientific reports* 4.1 (2014), pp. 1–5.
- [Hol+19] M. Holler, M. Odstrcil, M. Guizar-Sicairos, M. Lebugle, E. Müller, S. Finizio, G. Tinti, C. David, J. Zusman, W. Unglaub, et al. “Three-dimensional imaging of integrated circuits with macro-to nanoscale zoom.” In: *Nature Electronics* 2.10 (2019), pp. 464–470.
- [Hom+15] C. Homann, T. Hohage, J. Hagemann, A.-L. Robisch, and T. Salditt. “Validity of the empty-beam correction in near-field imaging.” In: *Physical Review A* 91.1 (2015), p. 013821.
- [How+09] M. R. Howells, T. Beetz, H. N. Chapman, C. Cui, J. Holton, C. Jacobsen, J. Kirz, E. Lima, S. Marchesini, H. Miao, et al. “An assessment of the resolution limitation due to radiation-damage in x-ray diffraction microscopy.” In: *Journal of electron spectroscopy and related phenomena* 170.1-3 (2009), pp. 4–12.
- [Hru10] R. Hruban. “Ductal adenocarcinoma of the pancreas.” In: *WHO classification of digestive tumors* (2010), pp. 281–290.

- [Hub+18] M. Hubert, A. Pacureanu, C. Guilloud, Y. Yang, J. C. da Silva, J. Laurencin, F. Lefebvre-Joud, and P. Cloetens. “Efficient correction of wavefront inhomogeneities in X-ray holographic nanotomography by random sample displacement.” In: *Applied Physics Letters* 112.20 (2018), p. 203704.
- [Huh+22] S. Huhn, L. M. Lohse, J. Lucht, and T. Salditt. “Fast algorithms for nonlinear and constrained phase retrieval in near-field X-ray holography based on Tikhonov regularization.” In: *Opt. Express* 30.18 (2022), pp. 32871–32886. DOI: 10.1364/OE.462368.
- [KS01] A. C. Kak and M. Slaney. *Principles of computerized tomographic imaging*. SIAM, 2001.
- [Kal12] S. Kalbfleisch. *A dedicated endstation for waveguide-based x-ray imaging*. Vol. 10. Universitätsverlag Göttingen, 2012.
- [Kep+21] D. Keppeler, C. A. Kampshoff, A. Thirumalai, C. J. Duque-Afonso, J. J. Schaeper, T. Quilitz, M. Töpperwien, C. Vogl, R. Hessler, et al. “Multiscale photonic imaging of the native and implanted cochlea.” In: *Proceedings of the National Academy of Sciences* 118.18 (2021), e2014472118.
- [Khi+18] A. Khimchenko, C. Bikis, A. Pacureanu, S. E. Hieber, P. Thalmann, H. Deyhle, G. Schweighauser, J. Hench, S. Frank, M. Müller-Gerbl, et al. “Hard X-ray nanoholography: large-scale, label-free, 3D neuroimaging beyond optical limit.” In: *Advanced Science* 5.6 (2018), p. 1700694.
- [Kim+20] M. A. Kimm, M. Willner, E. Drecoll, J. Herzen, P. B. Noël, E. J. Rummeny, F. Pfeiffer, and A. A. Fingerle. “Grating-based phase-contrast CT (PCCT): histopathological correlation of human liver cirrhosis and hepatocellular carcinoma specimen.” In: *Journal of Clinical Pathology* 73.8 (2020), pp. 483–487.
- [Kos+13] A. Kostenko, K. J. Batenburg, H. Suhonen, S. E. Offerman, and L. J. van Vliet. “Phase retrieval in in-line x-ray phase contrast imaging based on total variation minimization.” In: *Opt. Express* 21.1 (2013), pp. 710–723. DOI: 10.1364/OE.21.000710.
- [Kre15] M. Krenkel. “Cone-beam x-ray phase-contrast tomography for the observation of single cells in whole organs.” PhD thesis. Georg-August-Universität Göttingen, 2015.

- [Krü+12] S. Krüger, H. Neubauer, M. Bartels, S. Kalbfleisch, K. Giewekemeyer, P. Wilbrandt, M. Sprung, and T. Salditt. “Sub-10 nm beam confinement by X-ray waveguides: design, fabrication and characterization of optical properties.” In: *Journal of synchrotron radiation* 19.2 (2012), pp. 227–236.
- [Krü+10] S. P. Krüger, K. Giewekemeyer, S. Kalbfleisch, M. Bartels, H. Neubauer, and T. Salditt. “Sub-15 nm beam confinement by two crossed x-ray waveguides.” In: *Optics Express* 18.13 (2010), pp. 13492–13501.
- [Kua+20] A. T. Kuan, J. S. Phelps, L. A. Thomas, T. M. Nguyen, J. Han, C.-L. Chen, A. W. Azevedo, J. C. Tuthill, J. Funke, P. Cloetens, et al. “Dense neuronal reconstruction through X-ray holographic nano-tomography.” In: *Nature neuroscience* 23.12 (2020), pp. 1637–1643.
- [Kul+19] S. Kulpe, M. Dierolf, B. Günther, M. Busse, K. Achterhold, B. Gleich, J. Herzen, E. Rummeny, F. Pfeiffer, and D. Pfeiffer. “K-edge subtraction computed tomography with a compact synchrotron X-ray source.” In: *Scientific reports* 9.1 (2019), pp. 1–8.
- [Kyr+11] A. Kyrieleis, V. Titarenko, M. Ibison, T. Connolley, and P. Withers. “Region-of-interest tomography using filtered backprojection: assessing the practical limits.” In: *Journal of microscopy* 241.1 (2011), pp. 69–82.
- [Lat19] T. Latychevskaia. “Lateral and axial resolution criteria in incoherent and coherent optics and holography, near-and far-field regimes.” In: *Applied Optics* 58.13 (2019), pp. 3597–3603.
- [Lat21] T. Latychevskaia. “Chapter One - Phase retrieval methods applied to coherent imaging.” In: *Advances in Imaging and Electron Physics*. Ed. by M. Hýtch and P. W. Hawkes. Vol. 218. *Advances in Imaging and Electron Physics*. Elsevier, 2021, pp. 1–62. DOI: <https://doi.org/10.1016/bs.aiep.2021.04.001>.
- [LLF12] T. Latychevskaia, J.-N. Longchamp, and H.-W. Fink. “When holography meets coherent diffraction imaging.” In: *Optics express* 20.27 (2012), pp. 28871–28892.
- [L NK20] E. Y. Lee, M.-Y. Ng, and P.-L. Khong. “COVID-19 pneumonia: what has CT taught us?” In: *The Lancet Infectious Diseases* 20.4 (2020), pp. 384–385.

- [Loh+20a] L. M. Lohse, A.-L. Robisch, M. Töpperwien, S. Maretzke, M. Krenkel, J. Hagemann, and T. Salditt. “A phase-retrieval toolbox for X-ray holography and tomography.” In: *Journal of Synchrotron Radiation* 27.3 (2020), pp. 852–859.
- [Loh+20b] L. Lohse, M. Vassholz, M. Töpperwien, T. Jentschke, A. Bergamaschi, S. Chiriotti, and T. Salditt. “Spectral  $\mu$ CT with an energy resolving and interpolating pixel detector.” In: *Optics Express* 28.7 (2020), pp. 9842–9859.
- [Luk04] D. R. Luke. “Relaxed averaged alternating reflections for diffraction imaging.” In: *Inverse problems* 21.1 (2004), p. 37.
- [Luu+14] M. B. Luu, G. A. Van Riessen, B. Abbey, M. W. Jones, N. W. Phillips, K. Elgass, M. D. Junker, D. J. Vine, I. McNulty, G. Cadenazzi, et al. “Fresnel coherent diffractive imaging tomography of whole cells in capillaries.” In: *New Journal of Physics* 16.9 (2014), p. 093012.
- [MJL17] A. Maiden, D. Johnson, and P. Li. “Further improvements to the Ptychographical iterative engine.” In: *Optica* 4.7 (2017), pp. 736–745.
- [Mar19] S. Maretzke. “Inverse Problems in Propagation-based X-ray Phase Contrast Imaging and Tomography: Stability Analysis and Reconstruction Methods.” PhD thesis. Niedersächsische Staats- und Universitätsbibliothek Göttingen, 2019.
- [MKN17] T. Martin, A. Koch, and M. Nikl. “Scintillator materials for x-ray detectors and beam monitors.” In: *MRS Bulletin* 42.6 (2017), pp. 451–457.
- [Men+20] T. Menter, J. D. Haslbauer, R. Nienhold, S. Savic, H. Hopfer, N. Deigendesch, S. Frank, D. Turek, N. Willi, H. Pargger, et al. “Postmortem examination of COVID-19 patients reveals diffuse alveolar damage with severe capillary congestion and variegated findings in lungs and other organs suggesting vascular dysfunction.” In: *Histopathology* 77.2 (2020), pp. 198–209.
- [Mia+99] J. Miao, P. Charalambous, J. Kirz, and D. Sayre. “Extending the methodology of X-ray crystallography to allow imaging of micrometre-sized non-crystalline specimens.” In: *Nature* 400.6742 (1999), pp. 342–344.
- [Mie+19] A. Miettinen, I. V. Oikonomidis, A. Bonnin, and M. Stampanoni. “NR-Stitcher: non-rigid stitching of terapixel-scale volumetric images.” In: *Bioinformatics* 35.24 (2019), pp. 5290–5297.



- [MNA16] F. Milletari, N. Navab, and S.-A. Ahmadi. “V-net: Fully convolutional neural networks for volumetric medical image segmentation.” In: *2016 fourth international conference on 3D vision (3DV)*. IEEE, 2016, pp. 565–571.
- [Mom+03] A. Momose, S. Kawamoto, I. Koyama, Y. Hamaishi, K. Takai, and Y. Suzuki. “Demonstration of X-ray Talbot interferometry.” In: *Japanese journal of applied physics* 42.7B (2003), p. L866.
- [MPS12] K. S. Morgan, D. M. Paganin, and K. K. Siu. “X-ray phase imaging with a paper analyzer.” In: *Applied Physics Letters* 100.12 (2012), p. 124102.
- [Mül+18] M. Müller, M. A. Kimm, S. Ferstl, S. Allner, K. Achterhold, J. Herzen, F. Pfeiffer, and M. Busse. “Nucleus-specific X-ray stain for 3D virtual histology.” In: *Scientific reports* 8.1 (2018), pp. 1–10.
- [MA96] M. Müller and G. R. Arce. “Truncation artifacts in tomographic reconstructions from projections.” In: *Applied optics* 35.20 (1996), pp. 3902–3914.
- [Nat01] F. Natterer. *The mathematics of computerized tomography*. SIAM, 2001.
- [Nik06] M. Nikl. “Scintillation detectors for x-rays.” In: *Measurement Science and Technology* 17.4 (2006), R37.
- [Ohn+00] B. Ohnesorge, T. Flohr, K. Schwarz, J. Heiken, and K. Bae. “Efficient correction for CT image artifacts caused by objects extending outside the scan field of view.” In: *Medical physics* 27.1 (2000), pp. 39–46.
- [OS11] M. Osterhoff and T. Salditt. “Coherence filtering of x-ray waveguides: analytical and numerical approach.” In: *New Journal of Physics* 13.10 (2011), p. 103026.
- [Pac19] G. Pacchioni. “An upgrade to a bright future.” In: *Nature Reviews Physics* 1.2 (2019), pp. 100–101.
- [Pag06] D. M. Paganin. *Coherent X-Ray Optics*. New York: Oxford University Press, 2006.
- [Pag+02] D. Paganin, S. C. Mayo, T. E. Gureyev, P. R. Miller, and S. W. Wilkins. “Simultaneous phase and amplitude extraction from a single defocused image of a homogeneous object.” In: *Journal of microscopy* 206.1 (2002), pp. 33–40.

- [Pfe+06] F. Pfeiffer, T. Weitkamp, O. Bunk, and C. David. “Phase retrieval and differential phase-contrast imaging with low-brilliance X-ray sources.” In: *Nature physics* 2.4 (2006), pp. 258–261.
- [Rad17] J. Radon. “Über die Bestimmung von Funktionen durch ihre Integralwerte längs gewisser Mannigfaltigkeiten.” In: *Akad. Wiss.* 69 (1917), pp. 262–277.
- [Ram+21] K. Ramesh, G. K. Kumar, K. Swapna, D. Datta, and S. S. Rajest. “A review of medical image segmentation algorithms.” In: *EAI Endorsed Transactions on Pervasive Health and Technology* 7.27 (2021), e6–e6.
- [Rei+17] M. Reichardt, J. Frohn, M. Toepperwien, J.-D. Nicolas, A. Markus, F. Alves, and T. Salditt. “Nanoscale holographic tomography of heart tissue with x-ray waveguide optics.” In: *Developments in X-Ray Tomography XI*. Vol. 10391. SPIE. 2017, pp. 27–38.
- [Rei+20] M. Reichardt, J. Frohn, A. Khan, F. Alves, and T. Salditt. “Multi-scale X-ray phase-contrast tomography of murine heart tissue.” In: *Biomedical optics express* 11.5 (2020), pp. 2633–2651.
- [Rei+21] M. Reichardt, P. Moller Jensen, V. Andersen Dahl, A. BJORHOLM DAHL, M. ACKERMANN, H. SHAH, F. LÄNGER, C. WERLEIN, M. P. KUEHNEL, D. JONIGK, and T. SALDITT. “3D virtual histopathology of cardiac tissue from Covid-19 patients based on phase-contrast X-ray tomography.” In: *eLife* 10 (2021). Ed. by H. Chaudhry and M. Barton, e71359. DOI: 10.7554/eLife.71359.
- [Rei+19] M. Reichardt, M. Töpperwien, A. Khan, F. Alves, and T. Salditt. “Fiber orientation in a whole mouse heart reconstructed by laboratory phase-contrast micro-CT.” In: *Developments in X-Ray Tomography XII*. Vol. 11113. International Society for Optics and Photonics. 2019, 111130S.
- [Riv16] F. Riva. “Development of new thin film scintillators for high-resolution X-ray imaging.” PhD thesis. Université de Lyon, 2016.
- [RFS20] A. Robisch, J. Frohn, and T. Salditt. “Iterative micro-tomography of biopsy samples from truncated projections with quantitative gray values.” In: *Physics in Medicine & Biology* 65.23 (2020), p. 235034.
- [Rob+20] A.-L. Robisch, M. Eckermann, M. Töpperwien, F. van der Meer, C. Stadelmann-Nessler, and T. Salditt. “Nanoscale x-ray holotomography of human brain tissue with phase retrieval based on multienergy recordings.” In: *Journal of Medical Imaging* 7.1 (2020), p. 013501.

- [Rod+21] G. Rodgers, W. Kuo, G. Schulz, M. Scheel, A. Migga, C. Bikis, C. Tanner, V. Kurtcuoglu, T. Weitkamp, and B. Müller. “Virtual histology of an entire mouse brain from formalin fixation to paraffin embedding. Part 1: Data acquisition, anatomical feature segmentation, tracking global volume and density changes.” In: *Journal of Neuroscience Methods* 364 (2021), p. 109354.
- [Rod+22] G. Rodgers, C. Tanner, G. Schulz, A. Migga, W. Kuo, C. Bikis, M. Scheel, V. Kurtcuoglu, T. Weitkamp, and B. Müller. “Virtual histology of an entire mouse brain from formalin fixation to paraffin embedding. Part 2: Volumetric strain fields and local contrast changes.” In: *Journal of Neuroscience Methods* 365 (2022), p. 109385.
- [RFB15] O. Ronneberger, P. Fischer, and T. Brox. “U-net: Convolutional networks for biomedical image segmentation.” In: *International Conference on Medical image computing and computer-assisted intervention*. Springer, 2015, pp. 234–241.
- [SAA17] T. Salditt, T. Aspelmeier, and S. Aeffner. *Biomedical Imaging*. De Gruyter, 2017.
- [Sal+15] T. Salditt, M. Osterhoff, M. Krenkel, R. N. Wilke, M. Priebe, M. Bartels, S. Kalbfleisch, and M. Sprung. “Compound focusing mirror and X-ray waveguide optics for coherent imaging and nano-diffraction.” In: *Journal of synchrotron radiation* 22.4 (2015), pp. 867–878.
- [San+22] G. S. Sangha, B. Hu, G. Li, S. E. Fox, A. B. Sholl, J. Brown, and C. J. Goergen. “Assessment of photoacoustic tomography contrast for breast tissue imaging using 3D correlative virtual histology.” In: *Scientific reports* 12.1 (2022), pp. 1–13.
- [Sch+11] T. Schoonjans, A. Brunetti, B. Golosio, M. S. del Rio, V. A. Solé, C. Ferrero, and L. Vincze. “The xraylib library for X-ray–matter interactions. Recent developments.” In: *Spectrochimica Acta Part B: Atomic Spectroscopy* 66.11-12 (2011), pp. 776–784.
- [Shi+20] H. Shi, X. Han, N. Jiang, Y. Cao, O. Alwalid, J. Gu, Y. Fan, and C. Zheng. “Radiological findings from 81 patients with COVID-19 pneumonia in Wuhan, China: a descriptive study.” In: *The Lancet infectious diseases* 20.4 (2020), pp. 425–434.

- [SMJ19] R. L. Siegel, K. D. Miller, and A. Jemal. “Cancer statistics, 2019.” In: *CA: a cancer journal for clinicians* 69.1 (2019), pp. 7–34.
- [Sni+95] A. Snigirev, I. Snigireva, V. Kohn, S. Kuznetsov, and I. Schelokov. “On the possibilities of x-ray phase contrast microimaging by coherent high-energy synchrotron radiation.” In: *Review of scientific instruments* 66.12 (1995), pp. 5486–5492.
- [Sol+21] J. Soltau, M. Vassholz, M. Osterhoff, and T. Salditt. “In-line holography with hard x-rays at sub-15 nm resolution.” In: *Optica* 8.6 (2021), pp. 818–823.
- [Sta+10] M. Stampanoni, F. Marone, P. Modregger, B. Pinzer, T. Thüring, J. Vila-Comamala, C. David, and R. Mokso. “Tomographic hard X-ray phase contrast micro- and nano-imaging at TOMCAT.” In: *AIP Conference Proceedings*. Vol. 1266. 1. American Institute of Physics. 2010, pp. 13–17.
- [Töp18] M. Töpperwien. “3d virtual histology of neuronal tissue by propagation-based x-ray phase-contrast tomography.” In: (2018).
- [Töp+19] M. Töpperwien, T. R. Doeppner, B. Zechmeister, M. Bähr, and T. Salditt. “Multiscale x-ray phase-contrast tomography in a mouse model of transient focal cerebral ischemia.” In: *Biomedical Optics Express* 10.1 (2019), pp. 92–103.
- [Töp+18] M. Töpperwien, F. van der Meer, C. Stadelmann, and T. Salditt. “Three-dimensional virtual histology of human cerebellum by X-ray phase-contrast tomography.” In: *Proceedings of the National Academy of Sciences* 115.27 (2018), pp. 6940–6945.
- [Töp+20] M. Töpperwien, F. van der Meer, C. Stadelmann, and T. Salditt. “Correlative x-ray phase-contrast tomography and histology of human brain tissue affected by Alzheimer’s disease.” In: *Neuroimage* 210 (2020), p. 116523.
- [TOH07] T. Tuohimaa, M. Otendal, and H. M. Hertz. “Phase-contrast x-ray imaging with a liquid-metal-jet-anode microfocus source.” In: *Applied Physics Letters* 91.7 (2007), p. 074104.
- [Tur+04] L. D. Turner, B. Dhal, J. Hayes, A. Mancuso, K. A. Nugent, D. Paterson, R. E. Scholten, C. Tran, and A. G. Peele. “X-ray phase imaging: Demonstration of extended conditions with homogeneous objects.” In: *Optics express* 12.13 (2004), pp. 2960–2965.

- [Våg+18] W. Vågberg, J. Persson, L. Szekely, and H. M. Hertz. “Cellular-resolution 3D virtual histology of human coronary arteries using x-ray phase tomography.” In: *Scientific reports* 8.1 (2018), pp. 1–7.
- [Van02] C. W. Van Eijk. “Inorganic scintillators in medical imaging.” In: *Physics in medicine & biology* 47.8 (2002), R85.
- [Ves+21] M. Vesely, R. Valadian, L. M. Lohse, M. Toepperwien, K. Spiers, J. Garrevoet, E. T. Vogt, T. Salditt, B. M. Weckhuysen, and F. Meirer. “3-DX-ray Nanotomography Reveals Different Carbon Deposition Mechanisms in a Single Catalyst Particle.” In: *ChemCatChem* 13.10 (2021), pp. 2494–2507.
- [Wad32] H. Wadell. “Volume, shape, and roundness of rock particles.” In: *The Journal of Geology* 40.5 (1932), pp. 443–451.
- [Wal+21] C. Walsh, P. Tafforeau, W. Wagner, D. Jafree, A. Bellier, C. Werlein, M. Kühnel, E. Boller, S. Walker-Samuel, J. Robertus, et al. “Imaging intact human organs with local resolution of cellular structures using hierarchical phase-contrast tomography.” In: *Nature methods* 18.12 (2021), pp. 1532–1541.
- [Wei+17] T. Weitkamp, M. Scheel, J. Giorgetta, V. Joyet, V. L. Roux, G. Cauchon, T. Moreno, F. Polack, A. Thompson, and J. Samama. “The tomography beamline ANATOMIX at Synchrotron SOLEIL.” In: *Journal of Physics: Conference Series* 849.1 (2017), p. 012037. DOI: 10.1088/1742-6596/849/1/012037.
- [Wei+05] T. Weitkamp, A. Diaz, C. David, F. Pfeiffer, M. Stampanoni, P. Cloetens, and E. Ziegler. “X-ray phase imaging with a grating interferometer.” In: *Optics express* 13.16 (2005), pp. 6296–6304.
- [Wei+10] T. Weitkamp, P. Tafforeau, E. Boller, P. Cloetens, J.-P. Valade, P. Bernard, F. Peyrin, W. Ludwig, L. Helfen, and J. Baruchel. “Status and evolution of the ESRF beamline ID19.” In: *AIP Conference Proceedings*. Vol. 1221. 1. American Institute of Physics. 2010, pp. 33–38.
- [WK18] U. Welsch and W. Kummer. *Histologie. Das Lehrbuch*. Elsevier (Urban & Fischer), 2018.
- [Wil+12] R. Wilke, M. Priebe, M. Bartels, K. Giewekemeyer, A. Diaz, P. Karvinen, and T. Salditt. “Hard X-ray imaging of bacterial cells: nano-diffraction and ptychographic reconstruction.” In: *Optics express* 20.17 (2012), pp. 19232–19254.

- [Wil+96] S. Wilkins, T. E. Gureyev, D. Gao, A. Pogany, and A. Stevenson. “Phase-contrast imaging using polychromatic hard X-rays.” In: *Nature* 384.6607 (1996), pp. 335–338.
- [Wil+06] G. Williams, H. Quiney, B. Dhal, C. Tran, K. A. Nugent, A. Peele, D. Paterson, and M. De Jonge. “Fresnel coherent diffractive imaging.” In: *Physical review letters* 97.2 (2006), p. 025506.
- [Wil+10] G. Williams, H. Quiney, A. Peele, and K. Nugent. “Fresnel coherent diffractive imaging: treatment and analysis of data.” In: *New Journal of Physics* 12.3 (2010), p. 035020.
- [Wit20] F. Wittwer. “Development and Study of Refractive Phase Retrieval and X-ray Multibeam Ptychography.” PhD thesis. Staats-und Universitätsbibliothek Hamburg Carl von Ossietzky, 2020.
- [Zab+05] S. Zabler, P. Cloetens, J.-P. Guigay, J. Baruchel, and M. Schlenker. “Optimization of phase contrast imaging using hard x rays.” In: *Review of Scientific Instruments* 76.7 (2005), p. 073705.
- [Zan+14] I. Zanette, T. Zhou, A. Burvall, U. Lundström, D. H. Larsson, M. Zdora, P. Thibault, F. Pfeiffer, and H. M. Hertz. “Speckle-based x-ray phase-contrast and dark-field imaging with a laboratory source.” In: *Physical review letters* 112.25 (2014), p. 253903.
- [Zdo+20] M.-C. Zdora, P. Thibault, W. Kuo, V. Fernandez, H. Deyhle, J. Vila-Comamala, M. P. Olbinado, A. Rack, P. M. Lackie, O. L. Katsamenis, et al. “X-ray phase tomography with near-field speckles for three-dimensional virtual histology.” In: *Optica* 7.9 (2020), pp. 1221–1227.
- [Zdo+17] M.-C. Zdora, P. Thibault, T. Zhou, F. J. Koch, J. Romell, S. Sala, A. Last, C. Rau, and I. Zanette. “X-ray phase-contrast imaging and metrology through unified modulated pattern analysis.” In: *Physical review letters* 118.20 (2017), p. 203903.
- [ZYW16] Y. Zhou, J. Yao, and L. V. Wang. “Tutorial on photoacoustic tomography.” In: *Journal of biomedical optics* 21.6 (2016), p. 061007.

# List of publications

---

1. 3D VIRTUAL HISTOLOGY OF HUMAN PANCREATIC TISSUE BY MULTISCALE PHASE-CONTRAST X-RAY TOMOGRAPHY. J. Frohn, D. Pinkert-Leetsch, J. Missbach-Güntner, M. Reichardt, M. Osterhoff, F. Alves and T. Salditt. In: *J. Synchrotron Rad.*, 27(6), (2020). DOI: 10.1107/S1600577520011327.
2. NANOSCALE HOLOGRAPHIC TOMOGRAPHY OF HEART TISSUE WITH X-RAY WAVEGUIDE OPTICS. M. Reichardt, J. Frohn, M. Töpperwien, J.-D. Nicolas, A. Markus, F. Alves and T. Salditt. In: *Proc. SPIE 10391*, 1039105, (2017). DOI: 10.1117/12.2276648.
3. FORMATION AND DEVELOPMENT OF THE MALE COPULATORY ORGAN IN THE SPIDER PARASTEATODA TEPIDARIORUM INVOLVES A METAMORPHOSIS-LIKE PROCESS. F. S. C. Quade, J. Holtzheimer, J. Frohn, M. Töpperwien, T. Salditt and N.M. Prpic. In: *Scientific reports*, 9(1), (2019). DOI: 10.1038/s41598-019-43192-9.
4. ITERATIVE MICRO-TOMOGRAPHY OF BIOPSY SAMPLES FROM TRUNCATED PROJECTIONS WITH QUANTITATIVE GRAY VALUES. A.-L. Robisch, J. Frohn and T. Salditt. In: *Physics in Medicine & Biology*, 65(23), (2020). DOI: 10.1088/1361-6560/abc22f.
5. MULTI-SCALE X-RAY PHASE-CONTRAST TOMOGRAPHY OF MURINE HEART TISSUE. M. Reichardt, J. Frohn, A. Khan, F. Alves and T. Salditt. In: *Biomedical optics express*, 11(5), (2020). DOI: 10.1364/BOE.386576.
6. 3D VIRTUAL PATHOHISTOLOGY OF LUNG TISSUE FROM COVID-19 PATIENTS BASED ON PHASE CONTRAST X-RAY TOMOGRAPHY. M. Eckermann\*, J. Frohn\*, M. Reichardt\*, M. Osterhoff, M. Sprung, F. Westermeier, A. Tzankov, C. Werlein, M. Kühnel, D. Jonigk and T. Salditt. In: *Elife*, 9, (2020). DOI: 10.7554/eLife.60408.  
\* shared first authorship
7. 3D ANALYSIS OF THE MYENTERIC PLEXUS OF THE HUMAN BOWEL BY X-RAY PHASE-CONTRAST TOMOGRAPHY – A FUTURE METHOD?. N. Peruzzi, B. Veress, L. B. Dahlin, T. Salditt, M. Andersson, M. Eckermann, J. Frohn, A.-L. Robisch,

- M. Bech and B. Ohlsson. In: *Scandinavian journal of gastroenterology*, 55(10), (2020). DOI: 10.1080/00365521.2020.1815079.
8. 3D PHASE-CONTRAST NANOTOMOGRAPHY OF UNSTAINED HUMAN SKIN BIOPSIES MAY IDENTIFY MORPHOLOGICAL DIFFERENCES IN THE DERMIS AND EPIDERMIS BETWEEN SUBJECTS. M. Eckermann, N. Peruzzi, J. Frohn, M. Bech, E. Englund, B. Veress, T. Salditt, L. B. Dahlin and B. Ohlsson. In: *Skin Research and Technology*, 27(3), (2021). DOI: 10.1111/srt.12974.
9. BINOCULAR MIRROR-SYMMETRIC MICROSACCADIC SAMPLING ENABLES DROSOPHILA HYPERACUTE 3D VISION. J. Kemppainen, B. Scales, K. R. Haghghi, J. Takalo, N. Mansour, J. McManus, G. Leko, P. Saari, J. Hurcomb, A. Antohi, J.-P. Suuronen, F. Blanchard, R.C. Hardie, Z. Song, M. Hampton, M. Eckermann, F. Westermeier, J. Frohn, H. Hoekstra, C.-H. Lee, M. Huttula, R. Mokso and M. Juusola. In: *Proceedings of the National Academy of Sciences*, 119(12), (2022). DOI: 10.1073/pnas.2109717119.
10. STRUCTURE OF THE MYENTERIC PLEXUS IN NORMAL AND DISEASED HUMAN ILEUM ANALYZED BY X-RAY VIRTUAL HISTOLOGY SLICES. B. Veress, N. Peruzzi, M. Eckermann, J. Frohn, T. Salditt, M. Bech, B. Ohlsson. In: *World Journal of Gastroenterology*, 3994-4006, (2022). DOI: 10.3748/wjg.v28.i29.3994.



# Acknowledgements

---

An dieser Stelle möchte ich vielen Menschen danken, die mich während meiner Promotionszeit begleitet und unterstützt haben.

Mein ganz besonderer Dank gilt Prof. Tim Salditt, welcher mir nicht nur die Möglichkeit zur Promotion an diesem spannenden Projekt gegeben hat, sondern auch immer mit Rat und Tat zur Seite stand. Seine wissenschaftliche Neugier und kreative Denkweise war stets inspirierend und hat mir oft bei wissenschaftlichen Problemen geholfen. Neben seiner außerordentlichen wissenschaftlichen Expertise habe ich immer seine Bodenständigkeit und den respektvollen Umgang mit anderen Menschen sehr geschätzt. Ich möchte mich bei Prof. Alexander Egner für die Betreuung meiner Arbeit im Rahmen des Thesis Committees und die Bereitschaft zum Erstellen des Zweitgutachtens bedanken. Ich danke Prof. Frauke Alves sowohl für die Betreuung meiner Arbeit im Rahmen des Thesis Committees als auch für die tolle gemeinsame Zusammenarbeit in diversen Projekten. Weiterhin möchte ich mich bei Prof. Sarah Köster, Prof. Timo Betz und Prof. Florentin Wörgötter für Beteiligung an meiner Prüfungskommission bedanken.

Ein großer Dank gilt Dr. Michael Sprung und Fabian Westermeier für das Bereitstellen einer tollen Beamline und die Hilfe bei zahlreichen P10 Messzeiten. Falls mal ein Problem auftrat oder spontan neue Sachen ausprobiert wurden, sind Lösungen innerhalb kürzester Zeit gefunden worden. An dieser Stelle ist auch Dr. Markus Osterhoff zu nennen, ohne dessen permanenten *"online Support"* wahrscheinlich kaum ein Experiment an der GINIX erfolgreich gewesen wäre.

Weiterhin möchte ich mich beim gesamten IRP für tolle Jahre bedanken. Dr. Markus Osterhoff und Jan Goeman danke ich für die Bereitstellung einer tollen und unkomplizierten IT-Infrastruktur. Falls doch mal Probleme auftraten, konnten diese jederzeit schnell behoben werden. Ich danke Kerstin Pluschke und Michaela Ständer für die schnelle und reibungslose Hilfe bei administrativen Angelegenheiten. Weiterhin danke ich Bastian Hartmann, Peter Luley und Mike Kanbach für stets schnelle Lösungen bei technischen Problemen in den Laboren, sowie für gute Ideen bei der praktischen Umsetzung von Konstruktionen, die für das Experiment notwendig waren.

Zahlreiche Diskussionen, tägliche Mensagänge und schöne Freizeitaktivitäten mit den Studierenden des IRPs haben mir sehr geholfen. Insbesondere möchte ich mich hiermit bei Jakob Soltau, Karlo Komorowski, Hannes Hoeppe, Leon Lohse, Jens Lucht, Paul Meyer, Charlotte Neuhaus, Jette Alfken, Malte Vassholz, Marina Eckermann, Marius Reichardt, Jakob Reichmann, Simon Huhn und Mareike Töpferwien bedanken. Ein weiterer Dank gilt allen Korrekturlesern dieser Arbeit.

Der abschließende Dank gilt meiner langjährigen Partnerin Lina Gause, meinem guten Freund Philipp Wendt und meiner Familie für den notwendigen Rückhalt abseits der Promotion.

# Curriculum Vitae

---

## Personal Information

Name: Jasper Frohn  
Born: 18 October 1991 in Dannenberg (Elbe)  
Nationality: German

## Studies

since 07/2018      Doctoral student in Physics,  
Institut für Röntgenphysik,  
Group of Prof. Dr. Tim Salditt  
Georg-August-Universität, Göttingen

10/2014 - 07/2018      Master of Science in Physics  
Georg-August-Universität, Göttingen  
Title of thesis: “Construction of a setup for x-ray  
phase contrast tomography on micrometer scale  
at a rotating anode x-ray source”

10/2010 - 07/2014      Bachelor of Science in Physics  
Universität Hamburg  
Title of thesis: “Optical setup for generation of a  
sub-micron double focus”

01/2010 - 10/2010      Military service, Munster

06/2009      Abitur, Fritz-Reuter-Gymnasium in Dannenberg

To this day, the standard method for investigating biological tissue with cellular resolution is the examination under a light microscope, first denoted as histology by Karl Meyer in 1819. Despite the enormous success and importance of histology, it has two major disadvantages. Firstly, the specimen must be physically cut into thin sections due to the limited penetrating power of optical light, and secondly, additional staining of the specimen is required to achieve sufficient image contrast. Both disadvantages can be overcome by the non-destructive method of propagation-based X-ray phase-contrast tomography. While the mechanism of phase-contrast provides sufficient image contrast to image single cells, a tomographic imaging scheme with penetrating X-rays allows for an undamaged sample by virtually slicing the reconstructed 3D sample volume.

In this work, the holotomography setup of the synchrotron endstation „GINIX“ (The Göttingen Instrument for Nanoscale-Imaging with X-Rays) was extended to a multi-scale X-ray phase-contrast tomography setup suitable for 3D virtual histology by adding two acquisition schemes. Compared to the existing setup, the first additional scheme is a propagation-based microtomography setup, which enlarges the reconstructed 3D volumes by a factor of approx. 64 at a fraction of the acquisition time (ca. 2 min). The second additional scheme aims for higher resolutions. To this end, the X-ray waveguide illumination was combined with photon counting detector with a large field of view and a novel phase reconstruction scheme, which is based on iterative farfield phase retrieval without an „empty-beam correction“ in the detector plane.